Master Thesis

Material Characterization using Complementary Split Ring Resonators

performed at the

Institute of Electrodynamics, Microwave and Circuit Engineering
TU Wien

supervised by

Assoc. Prof. Dipl.-Ing. Dr. techn. Holger Arthaber
and
Univ. Ass. Dipl.-Ing. Jure Soklič

by

Edgar Philip Jirousek, BSc
Matr. Nr. 00827237

Vienna, August 24, 2022

Abstract

The relative complex permittivity is arguably the most decisive property of a dielectric. The desire to measure a dielectric's permittivity sparked an abundance of methods. This thesis introduces an improvement to a low-cost measurement method that emerged in the literature less than a decade ago.

Complementary split ring resonators (CSRRs) are defective ground structures, removed from the ground plane of a printed circuit board (PCB) beneath a microstrip line. A CSRR's resonant frequency is inversely proportional to its diameter. A CSRR is loaded by placing a dielectric on the ground plane. Loading a CSRR with a dielectric reduces its resonant frequency and insertion loss. These changes allow to determine a sample's complex permittivity and enable a low-cost method to characterize dielectrics.

Current CSRR based dielectric characterization methods relate the frequency shift and the magnitude of minimum transmission of a microstrip-coupled CSRR to the complex permittivity of material samples loading the CSRR. Instead of relying on those two quantities, I present a method to characterize materials that takes the complex scattering matrices (S-matrices) of CSRRs over a large frequency range into account. The S-matrices are used to represent the CSRR by its equivalent circuit. The values for the elements in the equivalent circuit change when loading a CSRR. These changes are used to determine the sample's relative complex permittivity in this thesis.

I formulate an improved equivalent circuit representation for CSRRs by minimizing the mean Frobenius distance between simulated CSRRs and their equivalent circuit. Having found an improved equivalent circuit, I study the effect of a material sample backing a CSRR on the elements of the equivalent circuit based on simulations. I formulate a method to calculate the sample's permittivity based on the equivalent circuit elements.

The established relation between the equivalent circuit elements and a dielectric's permittivity is experimentally verified using a custom-made test fixture and material samples whose permittivity is already known. The test fixture is a PCB on an FR-4 substrate that contains CSRRs with resonant frequencies ranging from 1 GHz to 4 GHz. I measure the scattering parameters (S-parameters) of the CSRRs when they are not loaded and when they are loaded with each of the samples. The S-parameters are used to determine the values of the elements in the equivalent circuit. The relation between the equivalent circuit parameters and a sample's permittivity is successfully demonstrated.

Kurzfassung

Die relative Permittivität ist die wohl wichtigste Eigenschaft eines Dielektrikums im bereich der Hochfrequenztechnik. Das bestreben, sie zu messen, brachte eine Vielzahl von Messmethoden hervor. Diese Diplomarbeit stellt eine Verbesserung einer kostengünstigen Messmethode vor, welche erst im letzten Jahrzent in der Literatur erschien.

Ein CSRR (englisch: complementary split ring resonator) bildet das Komplement eines Resonators, der aus geteilten Ringen besteht. CSRRs werden aus der Grundplatte einer Leiterplatte unterhalb einer Mikrostreifenleitung entfernt. Die Resonanzfrequenz eines CSRRs ist indirekt proportional zu seinem Durchmesser. CSRRs werden belastet, indem man ein Dielektrikum auf die Seite der Grundplatte legt, die nicht das Substrat berührt. Belastet man ein CSRR mit einem Dielektrikum, so reduziert man dabei die Resonanzfrequenz und die Einfügedämpfung. Diese Änderungen lassen auf die komplexe Permittivität des Dielektrikums schliessen.

Aktuelle Methoden in der Literatur bilden die Änderungen der Resonanzfrequenz und der Einfügedämpfung auf die Permittivität und den Verlustfaktor eines Dielektrikums ab. Anstatt Dieletkrika anhand der Einfügedämpfung und des Verlustfaktors zu bestimmen, präsentiere ich eine Methode, die die komplexen Streumatrizen belasteter CSRRs über einen großen Frequenzbereich berücksichtigt. Die Streumatrizen werden verwendet, um ein CSRR anhand einer Ersatzschaltung darzustellen. Die Werte der Elemente der Ersatzschaltung eines unbelasteten CSRRs unterscheiden sich von denen eines belasteten CSRRs. Diese Änderungen werden herangezogen, um die komplexe Permittivität von Dielektrika zu ermitteln.

Ich formuliere ein verbessertes Ersatzschaltbild für CSRRs, das die Frobenius Distanz zwischen simulierten CSRRs und ihrem Ersatzschaltbild minimiert. Basierend auf Simulationen, untersuche ich den Einfluss von Dielektrika, die ein CSRR belasten, auf dessen Ersatzschaltbild. Ich formuliere Ausdrücke, mit denen die Permittivität und Verlustfaktor anhand der Werte der Elemente in der Ersatzschaltung berechnet werden kann.

Das formulierte Verhältnis zwischen der Permittivität eines Dielektrikums und den Werten der Elemente im Ersatzschaltbild wird mit einer eigens gefertigten Testvorrichtung, und Materialproben, deren Permittivität bekannt ist, experimentell nachgewiesen. Die Testvorrichtung ist eine Leiterplatte auf einem FR-4 Substrat, die CSRRs mit unterschiedlichen Resonanzfrequenzen zwischen 1 GHz und 4 GHz enthält. Ich messe die Streuparameter der CSRRs wenn sie unbelastet sind, und wenn sie mit unterschiedlichen Dielektrika belastet sind. Die Werte der Elemente der Ersatzschaltung der CSRRs werden anhand der Streuparameter berechnet. Der Zusammenhang zwischen der Permittivität eines Dielektrikums und den Werten der Elemente im Ersatzschaltbild wird erfolgreich nachgewiesen.

Acknowledgements

I want to give a special thanks to Holger Arthaber and Jure Soklič for their excellent supervision of this master thesis.

I further want to thank Christoph Mecklenbräuker for introducing me to the subject of wave propagation, antennas, and radio frequency engineering back in the bachelor-programme.

This work was supported by the Christian Doppler Laboratory for Location-aware Electronic Systems.

Table of Contents

1 Introduction **1**

1.1 Commercial State-of-the-Art 4

1.1.1 Split-Cylinder Resonators 4

1.1.2 Split-Dielectric Resonators 5

1.1.3 Parallel Plate Method 6

1.1.4 Coaxial Probe 7

1.2 Emerging Methods 8

1.2.1 Transmission/Reflection Method 8

1.2.2 Complementary Split Ring Resonators 8

1.3 Proposed Method Outline 10

2 Modelling Complementary Split Ring Resonators **11**

2.1 Design and Simulation 12

2.1.1 Equivalent Circuit Models 13

2.1.2 Optimization 14

2.2 Results 15

2.2.1 Equivalent Circuit Comparison 15

2.2.2 Optimal Equivalent Circuit 15

3 Simulation-Based Permittivity Determination **22**
3.1 Field Simulations . . . 23
3.1.1 Results . . . 24
3.2 Equivalent Circuit Variations . . . 24
3.2.1 Variation 1 - Variation in All Parameters . . . 25
3.2.2 Variation 2 - Variation in the Resonator and Coupling Capacitor . . . 25
3.2.3 Variations 3 and 4 - Variation In Only the Resonator . . . 29
3.3 Determining an SUT's Complex Permittivity . . . 32
3.3.1 Real Permittivity . . . 32
3.3.2 Loss Tangent . . . 34

4 Experimental Test Fixture **36**
4.1 Footprint Optimization . . . 37
4.2 TRL Calibration Kit . . . 41
4.3 Size and Number of CSRRs . . . 42
4.4 Board Layout . . . 44

5 Measurement-Based Permittivity Determination **46**
5.1 Material Samples . . . 46
5.2 Measurement Setup . . . 48
5.3 Calibration . . . 48
5.4 Measurement Procedure . . . 50
5.5 Results and Discussion . . . 51
5.5.1 Real Permittivity . . . 52
5.5.2 Loss Tangent . . . 55
5.6 Conclusion . . . 60

6 Summary and Outlook **61**

A Complex Permittivity Measurement Example **63**
A.1 Required Components . . . 63
A.2 TRL Calibration . . . 64
A.2.1 Calibration Measurements with MultilineTRL . . . 66
A.3 Unloaded Resonator Equivalent Circuit . . . 66
A.4 Determining the CSRR's Parameters A and B . . . 67
A.5 Measuring a Samples Permittivity . . . 68

References **69**

List of Figures

1.1 Measurement methods for determining a material's ε_r, and their applicable range regarding frequency, and loss tangent. . . . 3

1.2 A split-cylinder resonator loaded with a sample. . . . 4

1.3 Sample Thickness influence on the resonant frequency of a split-cylinder resonator. . . . 5

1.4 Schematic cross section of a split-dielectric resonator. . . . 6

1.5 E_φ in an unloaded split-dielectric resonator (SDR) (a), and in a split-dielectric resonator (SDR) loaded with a sample under test (SUT) (b). . . . 6

1.6 Electric field in a parallel plate capacitor without (a) and with guard electrodes (b). . . . 7

1.7 Schematic cross section of a coaxial probe pressed against a sample under test (SUT) (a). Equivalent circuit (b). . . . 8

1.8 Coaxial (a) and rectangular (b) waveguides with an inserted sample under test (SUT). . . . 9

1.9 Complementary split ring resonator (CSRR) on a printed circuit board (PCB) with coaxial launch connectors. Top layer (a) and bottom layer (b). 9

1.10 Measuring a complementary split ring resonator (CSRR)'s scattering parameters (S-parameters) using a vector network analyzer (VNA). Measurement setup (a). Effect of the sample under test (SUT) on the resonant frequency (b). . . . 10

2.1 Top view of the printed circuit board (PCB) with a microstrip-coupled complementary split ring resonator (CSRR). . . . 13

2.2 S_{11} (left) and S_{21} (right) for different values of d. . . . 14

2.3 Equivalent circuit for a microstrip-coupled complementary split ring resonator (CSRR). Dashed elements are implemented in different ways. . . . 15

2.4 Error with respect to d for all circuit models. Models from Tab. 2.2 are in the legend. . . . 16

2.5 Examples for values of C_{Res} with respect to d for some models that involve C_{Neg}. 17

2.6 Optimal circuit for a microstrip-coupled complementary split ring resonator (CSRR) (Model 10). 17

2.7 Comparison of S_{11} (left) and S_{21} (right) between the Ansys High Frequency Structure Simulator (HFSS) simulations and the solution for Model 10 for $d = 7\,\mathrm{mm}$. 18

2.8 Length of the microstrip line with respect to d. 19

2.9 Values for C_{Cpl}, C_{Res}, L_{Line}, L_{Res} with respect to d. 20

2.10 Sensitivities $s\,(p)$ with respect to d, where p is one of the parameters from the legend. 21

3.1 Microstrip coupled complementary split ring resonators (CSRRs) on a printed circuit board (PCB), loaded with a sample under test (SUT) in Ansys High Frequency Structure Simulator (HFSS). Top layer (a), and bottom layer (b). 23

3.2 $|S_{21}|$ for different combinations of the sample under test (SUT)'s ε_r' and $\tan\delta$ for $h_{\mathrm{SUT}} = 10\,\mathrm{mm}$. The black line represents the unloaded complementary split ring resonator (CSRR). 25

3.3 Equivalent circuit model for the complementary split ring resonator (CSRR). 26

3.4 L_{Res} for different combinations of the sample under test (SUT)'s ε_r' and $\tan\delta$ with Variation 1 from Tab. 3.5. 27

3.5 l_{Line} for different combinations of the sample under test (SUT)'s ε_r' and $\tan\delta$ with Variation 1 from Tab. 3.5. 27

3.6 C_{Cpl} for different combinations of the sample under test (SUT)'s ε_r' and $\tan\delta$ with Variation 2 from Tab. 3.5. 28

3.7 C_{Res} for different combinations of the sample under test (SUT)'s ε_r' and $\tan\delta$ with Variation 2 from Tab. 3.5. 28

3.8 C_{Res} for different combinations of the sample under test (SUT)'s ε_r' and $\tan\delta$ with Variation 3 from Tab. 3.5. 29

3.9 G_{Res} for different combinations of the sample under test (SUT)'s ε_r' and $\tan\delta$ with Variation 3 from Tab. 3.5. 30

3.10 Q for different combinations of the sample under test (SUT)'s ε_r' and $\tan\delta$ with Variation 3 from Tab. 3.5. 30

3.11 L_{Res} for different combinations of the sample under test (SUT)'s ε_r' and $\tan\delta$ with Variation 3 from Tab. 3.5. 31

3.12 Resulting values for S for each combination of h_{SUT}, ε_r', and $\tan\delta$ after the optimizations. 33

3.13 Values for S from Fig. 3.12 divided by χ. 34

3.14 $\tilde{Q}^{-1}$ for different combinations of the sample under test (SUT)'s ε_r' and $\tan\delta$. 35

4.1 Full PCB (a) and one half (b) . . . 38
4.2 De-embedding the wave port up to the connector-microstrip-line interface. . 38
4.3 Top view of the optimized footprint for the coaxial launch connector. 39
4.4 Results for $|S_{11}|$ and $|S_{21}|$ for a simulated printed circuit board (PCB) with two connectors with the optimized footprint. . . . 40
4.5 Example of a TRL calibration kit and labels for its elements. . . . 41
4.6 Resonant frequency of an unloaded complementary split ring resonator (CSRR) $f_{\text{res},0}$ as function of the side length d. Dots represent exact values. The dashed curve is the approximation (4.2). . . . 43
4.7 Top layer (top) and bottom layer (bottom) of the complementary split ring resonator (CSRR) test fixture. . . . 45

5.1 Map of used materials listed in Tab. 5.1. . . . 47
5.2 Photo of the measurement setup. . . . 49
5.3 *MultilineTRL* GUI window. . . . 50
5.4 A sample loading CSRR 5 on the test fixture. . . . 51
5.5 A sample is pressed against a complementary split ring resonator (CSRR) with a block of Rohacell during measurement. . . . 51
5.6 Values for S after optimization using measurement data. . . . 53
5.7 Values for S/χ_{nom} after optimization using measurement data. . . . 54
5.8 Values for $\tilde{Q}^{-1}$ after optimization using measurement data. . . . 58
5.9 Values for Q_{Res} after optimization using measurement data. . . . 59

A.1 Example of `CalKitConf.txt`. . . . 64
A.2 Example of the first lines of `gammaEstimate.txt`. . . . 65
A.3 Screenshot of TxLine. . . . 65

List of Tables

1.1 Accuracy of common measurement methods. 3

2.1 Dimensions of the simulated complementary split ring resonators (CSRRs). 12

2.2 Implementations of dashed circuit elements for selected circuit models highlighted in Fig. 2.4. 16

3.1 Dimensions of the simulated complementary split ring resonator (CSRR). . 23

3.2 Values for h_{SUT}, ε_r' and $\tan\delta$. Models with all combinations were simulated. 23

3.3 Convergence and meshing criteria for the used Ansys High Frequency Structure Simulator (HFSS) simulations. 24

3.4 Optimized equivalent circuit parameters for the unloaded complementary split ring resonator (CSRR). 24

3.5 Variations in which circuit parameters to optimize and which to constrain. . 26

3.6 Relative errors for ε_r' at $h_{\mathrm{SUT}} = 10\,\mathrm{mm}$ using (3.8). 33

3.7 Absolute Errors for $\tan\delta$ for $h_{\mathrm{SUT}} = 10\,\mathrm{mm}$ when using the approximation in (3.13). 35

4.1 Dimensions for the footprint in Fig. 4.3. 40

4.2 Additional lengths of the line elements for the thru, reflect, line (TRL) calibration kit. The 20°- and 160°-Frequencies are the frequencies at which the additional electrical length of the line is 20 and 160 degrees, respectively. 42

4.3 Values for d for the complementary split ring resonators (CSRRs) in the test fixture. 43

5.1 Used materials with known relative complex permittivity, and the frequency at which it was measured. Blank spaces indicate missing data in datasheets. 47

5.2 Number of samples, their individual thickness, and the maximum thickness of all samples stacked on top of each other. 48

5.3 SOLT calibration settings. 49
5.4 Range for S/χ_{nom} for each of the five complementary split ring resonators (CSRRs). 55
5.5 Values for $a\,(10\,\mathrm{mm})$ and limits for e_χ for each of the five complementary split ring resonators (CSRRs). 55

List of Abbreviations

Q-factor quality factor

AFR auto fixture removal

CSRR complementary split ring resonator

E-cal electronic calibration

FWS 3-D full-wave simulation

GUI graphical user interface

HFSS Ansys High Frequency Structure Simulator

MUT material under test

PCB printed circuit board

RF radio frequency

RMSE root mean square error

RMSRE root mean square relative error

S-matrix scattering matrix

S-parameter scattering parameter

SCR split-cylinder resonator

SDR split-dielectric resonator

SOLT short, open, load, thru

SRR split ring resonator

SUT sample under test

TRL thru, reflect, line

VNA vector network analyzer

1 Introduction

The relative complex permittivity ε_r is arguably the most decisive property of a dielectric in radio frequency (RF) engineering. It relates the electric field strength $\vec{E}$ to the electric flux density $\vec{D}$ with the equation

$$\vec{D} = \varepsilon_r \varepsilon_0 \vec{E}, \tag{1.1}$$

where ε_0 is the vacuum permittivity, and

$$\varepsilon_r = \varepsilon_r' - j\varepsilon_r'', \tag{1.2}$$

where ε_r' and ε_r'' are the real and imaginary parts of ε_r respectively, and are used to define the loss tangent $\tan\delta$ as

$$\tan\delta = \frac{\varepsilon_r''}{\varepsilon_r'}. \tag{1.3}$$

For the rest of the thesis, I refer to ε_r' simply as relative permittivity. Knowing any dielectric's permittivity is crucial when incorporating it into any RF system, as the geometry of transmission lines, resonators, and antennas strongly depends on the permittivity of nearby dielectrics. The quest for extracting said knowledge gave rise to an abundance of measurement methods in the scientific literature [1], commercially available measurement devices [2, 3], and standards [4, 5, 6] over the last decades. Fig. 1.1 shows a map of measurement methods studied comprehensively in the literature, together with their suitable frequency and loss tangent range. Their accuracy is listed in Tab. 1.1. Every method has advantages and disadvantages, on the applicable frequency range, the required sample material shape and size, and the precision to which ε_r can be extracted.

There are two ways to categorize existing measurement techniques by their working principle:

(i) Invasive vs. noninvasive. This distinction pertains to necessary modifications to material samples. The material whose complex permittivity is being measured is called the material under test (MUT). The measurement requires one or many samples of the MUT, called samples under test (SUTs). Invasive methods require an SUT to be machined precisely to a shape with given dimensions to fit into a sample holder. The sample holder is usually made of metal and ensures that no energy is radiated into free space during the measurement, thus minimizing measurement errors. Downsides to invasive methods

arise from the shape and size constraints that samples must obey. Samples of the required size or shape might not be available or are prone to break when machining them into the required shape, as is the case with glass. Noninvasive methods generally do not have these strict requirements.

(ii) Resonant vs. nonresonant. The complex relative permittivity is a frequency-dependent property. When measuring a material's ε_r, one faces a trade-off between certainty in the measured value for ε_r and certainty in the frequency at which the measured value applies [1]. Resonant methods are ideal for achieving high certainty in the value of ε_r. Specifically, a higher quality factor (Q-factor) yields greater certainty in the value of ε_r at the cost of greater uncertainty in the applicable frequency. Resonant methods feature a resonator that is either coupled or loaded using an SUT. Resonators are loaded by placing an SUT where the electric field strength is greatest. That location is either inside a cavity or above a leaking slit. The unloaded resonator, where no SUT is present, exhibits a different resonant frequency and Q-factor than the loaded resonator. Common methods of determining an SUT's ε_r with resonators map the frequency shift to the real part of ε_r and the difference in Q-factors to the SUT's loss tangent. Nonresonant methods involve a transmission line that can be modified such that a wave propagates wholly or partly inside the SUT. The SUT locally alters the wave impedance and the group velocity on the transmission line. These changes allow for determining the SUT's permittivity [1].

This thesis provides a new method to determine an MUT's complex permittivity based on a test fixture that is low-cost and easy to manufacture. A low-cost, easily manufactured test fixture is a useful tool in work environments that design RF systems that are embedded in components whose complex permittivity must be measured in order to complete the design, but lack high-cost measuring devices to characterize dielectrics. Examples are start-ups or small-sized companies that specialize in the internet of things or e-ink displays that contain antennas. The permittivity's real part of nearby components plays a more critical role than the loss tangent, as the resonant frequency of antennas shifts with the presence of dielectrics. By contrast, the loss tangent of nearby dielectrics can often be neglected, as printed circuit boards (PCBs) antenna losses are governed by the PCB's substrate's loss tangent. Hence, this thesis puts a stronger focus on measuring an SUT's real permittivity than its loss tangent.

In the rest of this chapter, I discuss some of the measurement methods from Fig. 1.1, as well as their advantages and disadvantages. I introduce commercially available dielectric characterization mechanisms and explain their working principle in Section 1.1. Section 1.2 is dedicated to some methods thoroughly covered in the current literature which have not made their way to commercial applications. This includes the use of complementary split ring resonators (CSRRs), which serve as a basis for this thesis. Section 1.3 lays the groundwork for the rest of the thesis. CSRRs emerge as the best candidate that fulfills our specifications. I explain the shortcomings of the current methods of obtaining an SUT's permittivity using CSRRs and provide a summary of proposed improvements to the state-of-the-art that I implement in this thesis.

The rest of this thesis is structured as follows: In Chapter 2, I explain the derivation of an improved equivalent circuit model for unloaded CSRRs. Chapter 3 takes one step forward, where I simulate CSRRs loaded with a variety of SUTs using 3-D full-wave simulations (FWSs). The scattering parameters (S-parameters) of the simulation results are used to establish a relation between the SUT's complex permittivity and the values of the

equivalent circuit elements. In Chapter 4 an experimental test fixture is designed that contains multiple CSRRs. The test fixture serves to verify the established relations from Chapter 3 in Chapter 5. This work is concluded in Chapter 6.

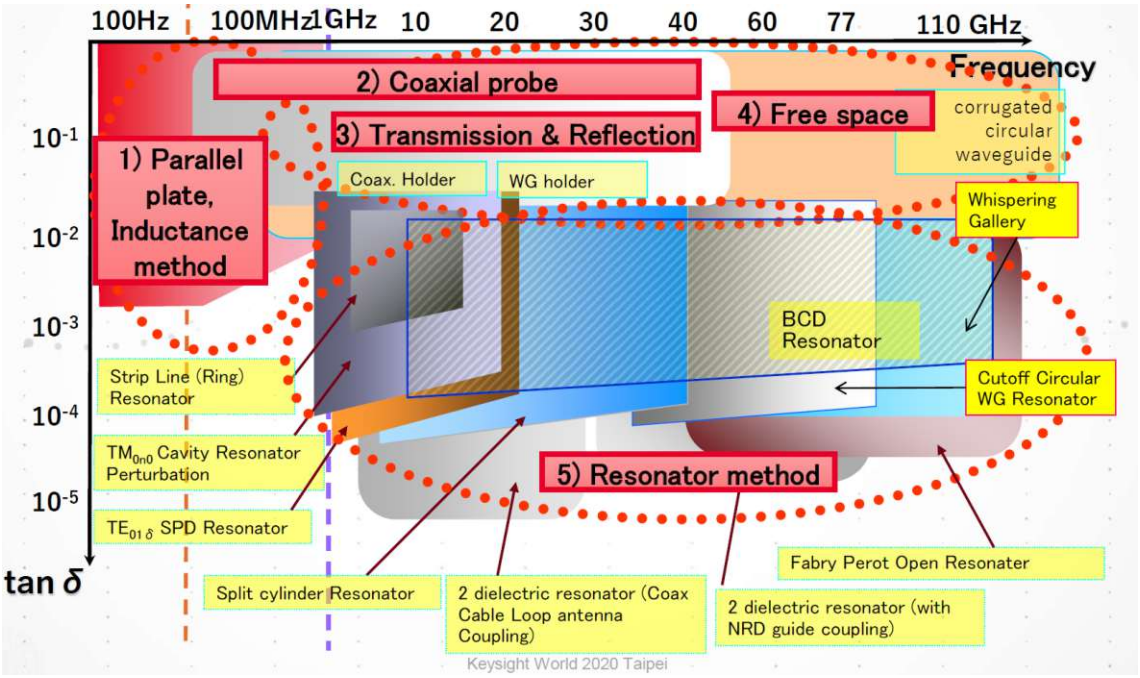

Figure 1.1: Measurement methods for determining a material's ε_r, and their applicable range regarding frequency and loss tangent. Figure from [7].

Table 1.1: Accuracy of common measurement methods.

Method	Accuracy	Resonant	Invasive
Split-Cylinder Resonator	$\approx 1\,\%$ for ε_r' [8] $\approx 10^{-4}$ for $\tan\delta$ [8]	Yes	No
Split-Dielectric Resonator	$\approx 1\,\%$ for ε_r' [9] $\approx 5\,\%$ for $\tan\delta$ [9]	Yes	No
Parallel Plate	$< 35\,\%$ for ε_r' at 100 Hz – 10 MHz [10] < 0.1 for $\tan\delta$ at 1 kHz – 10 MHz [10] < 0.01 for $\tan\delta$ at 100 kHz [10]	No	No
Coaxial Probe	> 0.2 for $\varepsilon_r = 10 - j0.01$ at 0.5 GHz – 2.5 GHz [11]	No	No
Transmission / Reflection	$< 2\,\%$ for ε_r' at 3 GHz [12] $< 9\,\%$ for ε_r'' at 3 GHz [12]	No	Yes

1.1 Commercial State-of-the-Art

In this section, I introduce measurement methods that are the principle behind commercially available measurement devices for characterizing solid, isotropic dielectrics.

1.1.1 Split-Cylinder Resonators

A split-cylinder resonator (SCR) is a hollow metal cylinder split into two identical halves. Joining the two halves together yields a closed cavity, the unloaded resonator. When measuring a sample's permittivity, the sample is placed between the two cylinder halves, as shown in Fig. 1.2. Inserting the sample changes the SCR's resonant frequency and Q-factor. The change in resonant frequency and Q-factor is used to determine the sample's complex permittivity. SCRs are available at frequencies from 10 GHz to 80 GHz [13].

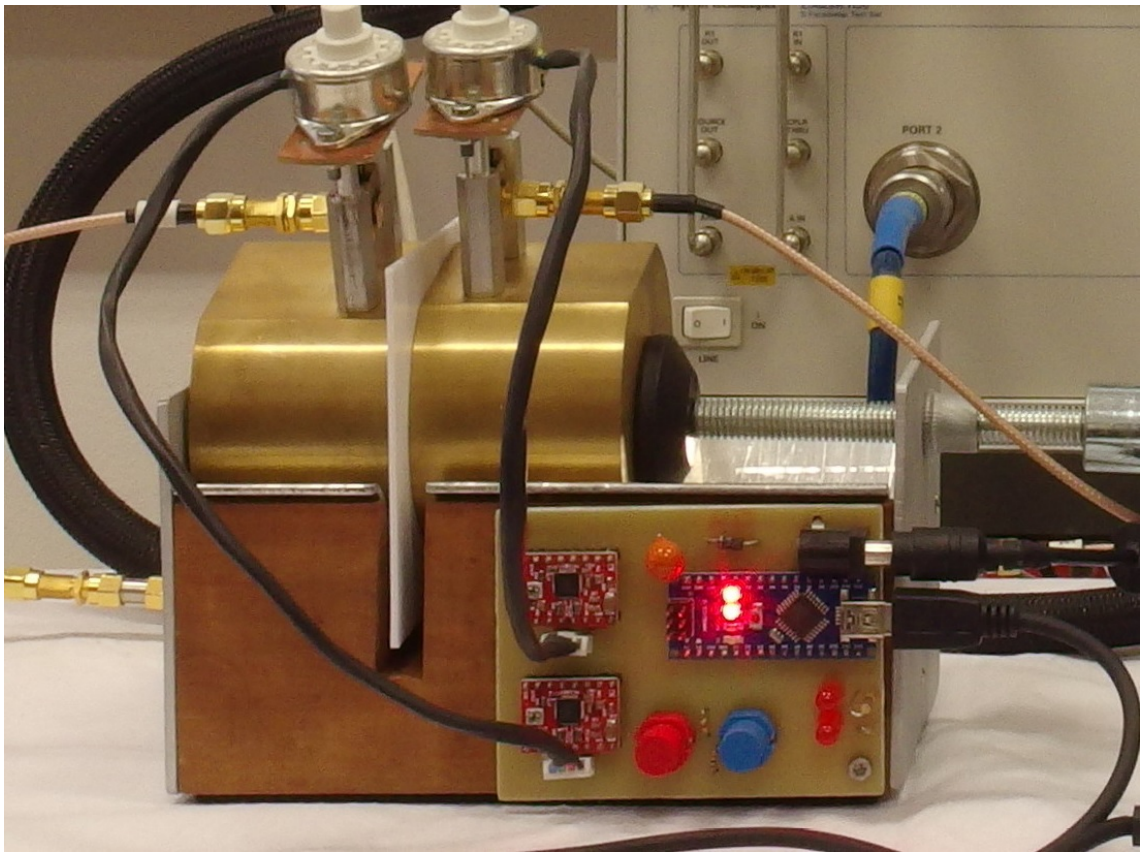

Figure 1.2: An SCR loaded with a sample. Figure from [14].

The SCR has some distinct advantages over other methods. Firstly, it features Q-factors on the order of 10^4 for 10 GHz [14], enabling a loss-tangent measurement of low-loss materials. Furthermore, no calibration involving a sample material with an already known permittivity is required.

One main disadvantage of using SCRs pertains to the sample requirements. The SUT's thickness must be uniform and accurately known. For 10 GHz, the uncertainty in the SUT's thickness must not be greater than 0.02 mm [4]. A greater uncertainty results in

inaccurate results for the SUT's complex permittivity. This effect is explained in Fig. 1.3, which shows the resonant frequency's strong dependence on the SUT's thickness. Furthermore, for 10 GHz, a sample should have a minimum diameter (for a circular sample) or a minimum side length (for a square sample) of 50 mm [4], and a thickness of no more than 3 mm [8]. This minimum sample size is proportional to the wavelength, thus limiting the applicable frequency range.

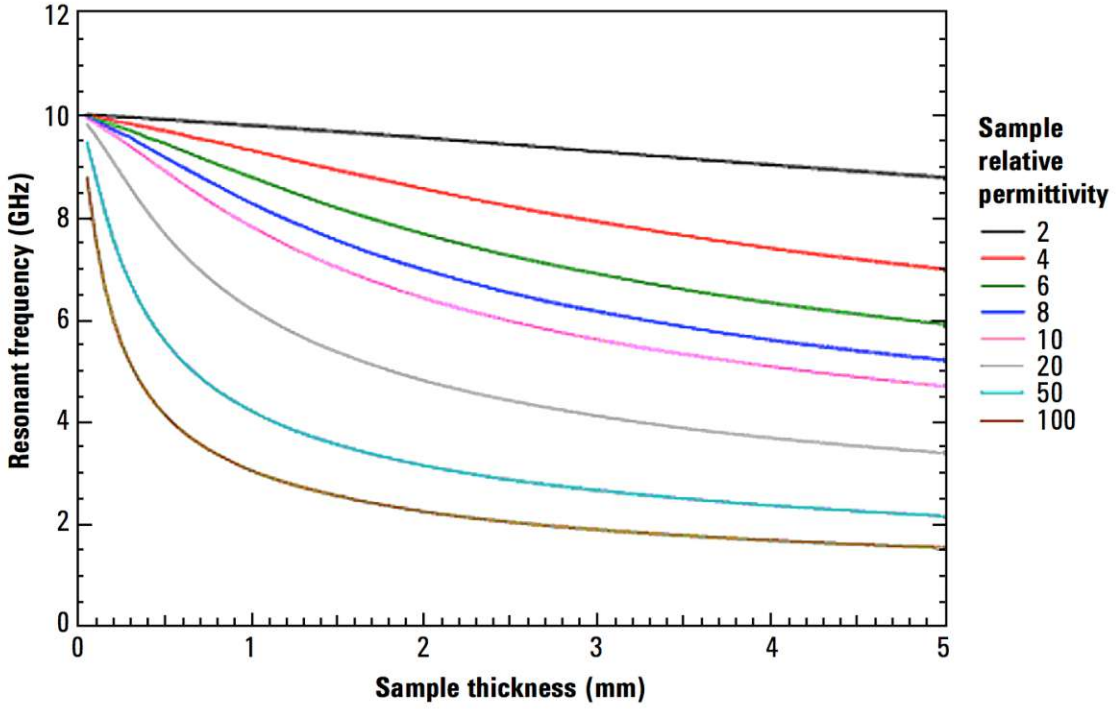

Figure 1.3: Sample Thickness influence on the resonant frequency of an SCR. Figure from [8].

1.1.2 Split-Dielectric Resonators

The split-dielectric resonator (SDR) employs a similar principle as the SCR, using two resonators with a sample in-between. Unlike the SCR, which consists of two metal-bounded, air-filled resonator halves, the SDR uses two dielectric resonators shaped as flat cylinders. Fig. 1.4 shows a schematic cross section of an SDR, where a sample is placed between two dielectric resonators. The coupling loops serve to couple the field into the inside of the metal enclosure and excite the dielectric resonators. The dielectric resonators are excited in the $TE_{01\delta}$ mode, whose electric field strength is zero perpendicular to the sample. The electric field strength of two closely spaced dielectric resonators is shown in Fig. 1.5a. Introducing a sample between the two resonators increases their coupling and shifts the resonant frequency. The corresponding electric field strength is shown in Fig. 1.5b. The sample's permittivity determines the shift in the resonant frequency.

SDRs are commercially available in the frequency range from 1 GHz to 20 GHz [3, 9, 15]. SDRs are suitable for thin films, as the sample thickness h is limited to no more than

approximately [9]

$$h < \frac{10\,\text{mm}}{f_{\text{res}}/1\,\text{GHz}} \tag{1.4}$$

and must be known to a precision of around 0.7% [9].

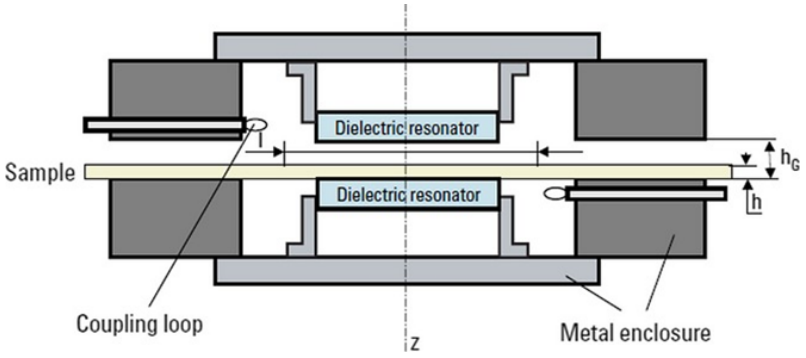

Figure 1.4: Schematic cross-section of a split post dielectric resonator. Figure from [16].

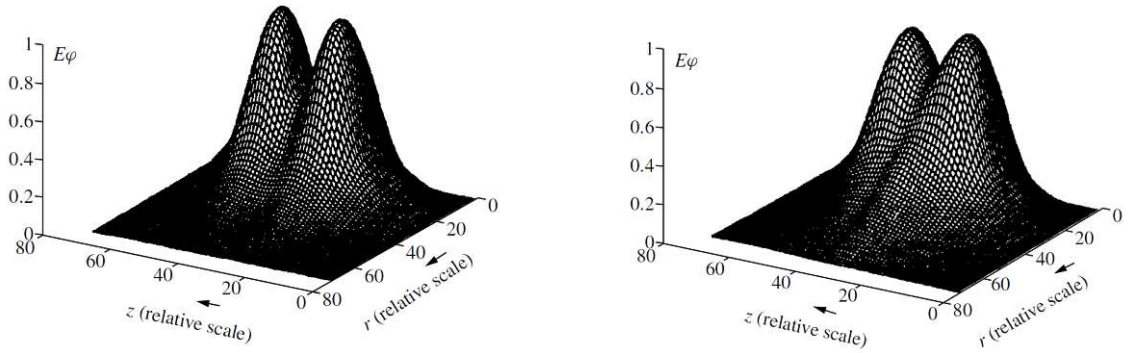

(a) **(b)**

Figure 1.5: E_φ in an unloaded SDR (a), and in an SDR loaded with an SUT (b). Figure from [1].

1.1.3 Parallel Plate Method

In the parallel plate method, the SUT is clamped between two parallel circular metal plates. The two parallel plates then act as a capacitor, with the SUT acting as the dielectric. The parallel plate's capacitance C_P and loss tangent $\tan\delta$ can be measured with an impedance analyzer. The SUT's permittivity can be calculated with the equations [17]

$$\varepsilon_r' = \frac{C_\text{P}\, t}{\varepsilon_0 \pi\, (d/2)^2}, \tag{1.5}$$

$$\varepsilon_r'' = \varepsilon_r' \tan\delta, \tag{1.6}$$

where t is the thickness of the SUT, and d is the plate's diameter. Equation (1.5) only applies if the electric field inside the SUT is uniform. However, in a parallel plate capacitor, the electric field fringes at the edges of the plates, and the electric field vector follows a curved path, as shown in Fig. 1.6a. This fringing field creates an additional stray capacitance between the two electrodes A and B and invalidates (1.5). This effect is

overcome with the solution in Fig. 1.6b. One electrode is split into two: a sensing electrode (B) and a guard electrode (C) [18]. The sensing- and guard electrodes are forced to the same potential with an auto-balancing bridge. With B and C having the same potential, the electric field in the SUT is the same as in Fig. 1.6a. Although the electric field still fringes at the edges, it is uniform between electrodes A and B, and (1.5) between the two electrodes applies. Commercially available parallel plate test fixtures are available at frequencies from 20 Hz to 1 GHz [10].

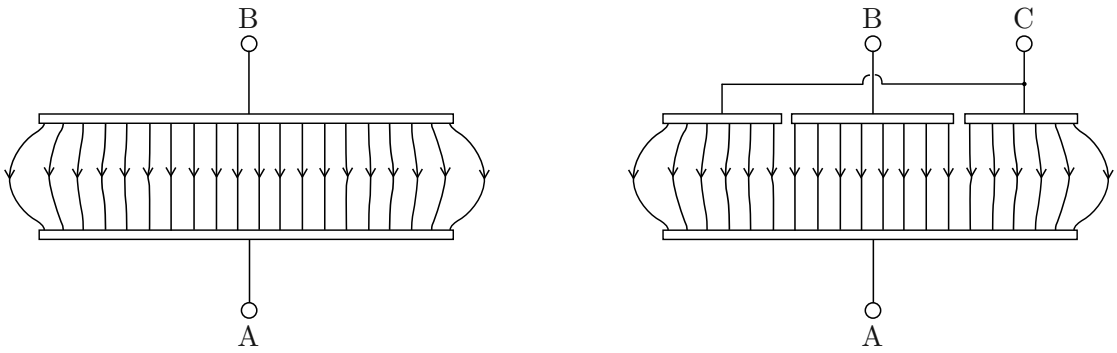

(a) (b)

Figure 1.6: Electric field in a parallel plate capacitor without (a) and with guard electrode (b) [17, 19, 20].

1.1.4 Coaxial Probe

The coaxial probe consists of an abruptly ending coaxial waveguide, whose end is pressed against an SUT. A schematic is shown in Fig. 1.7a. The SUT can be backed by air, metal, or another dielectric with known permittivity. The sample's ε_r is obtained from the reflection coefficient at the interface between the probe and the sample [1]. Coaxial probe measurement devices are commercially available up to 67 GHz [21]. Fig. 1.7b shows an equivalent circuit representation of the sample at the interface, where the reference plane contains the points A and A' in Fig. 1.7a. The capacitance C_f represents the capacitance of the probe, and $C(\varepsilon_r)$ represents the additional capacitance caused by the SUT.

A particular problem arises when there is a gap between the coaxial flange and the MUT. The size of this air gap has a significant impact on the termination impedance. The open-ended coaxial probe is a prevalent method for characterizing liquids, as there is no air gap between the flange and the MUT [1, 2]. The air gap is mitigated when characterizing solids by pressing the probe against the SUT with force. Furthermore, the coaxial probe must be calibrated using samples with known permittivity. The residual error arising from the air gap can then be mitigated using an algorithm by Baker-Jarvis [11].

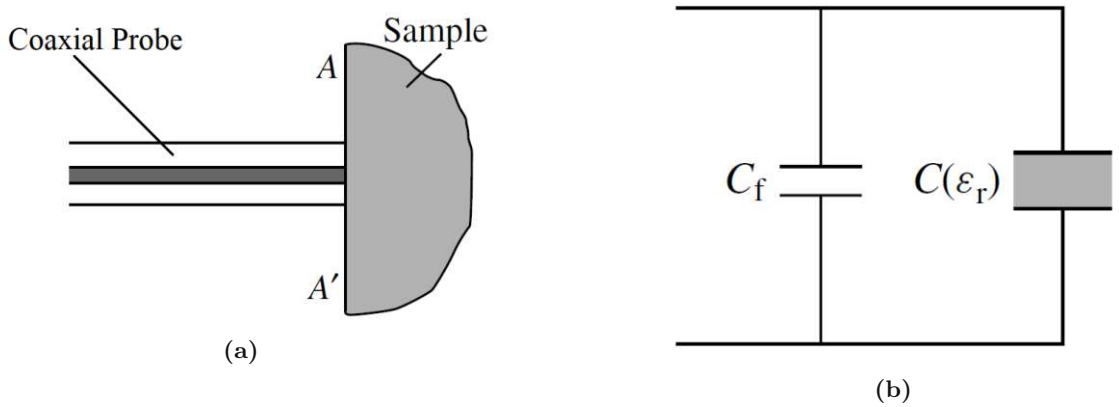

Figure 1.7: Schematic cross section of a coaxial probe pressed against an SUT (a). Equivalent circuit (b). Figures from [1].

1.2 Emerging Methods

Some measurement methods have not made their way to commercial applications despite being studied thoroughly. I provide a brief description of some of these methods in this section.

1.2.1 Transmission/Reflection Method

The transmission/reflection method consists of a waveguide (e.g., coaxial or rectangular), where the SUT is placed inside a sample holder. An example is shown in Fig. 1.8. A transmission line containing the SUT has different S-parameters than the same line without the SUT. The S-parameters of both cases allow for calculating the SUT's complex permittivity. Notable algorithms for this purpose include the Nicolson–Ross–Weir (NRW) algorithm [22, 23] and its improvement, the Baker-Jarvis algorithm [12, 24].

The transmission/reflection method's main advantage lies in its wide bandwidth when using a coaxial transmission line. The main downside lies in the strict geometric constraints of the SUT. The SUT must fit perfectly into the sample holder. Otherwise, the method leads to inaccurate results.

1.2.2 Complementary Split Ring Resonators

Using planar microstrip-coupled resonators for determining a material's permittivity gained much attention in the last decade. Planar resonators require samples that only need to lay flat on a PCB and not be machined to a specific shape or size while still providing the greater accuracy of a resonant method. Due to being resonators, they can measure the relative complex permittivity only in a narrow band around the resonant frequency. Hence, measuring the permittivity over a broad range of frequencies requires multiple resonators. This downside is overcome by the low production cost and complexity, as planar microstrip-coupled resonators are built on PCBs, thus making them so appealing.

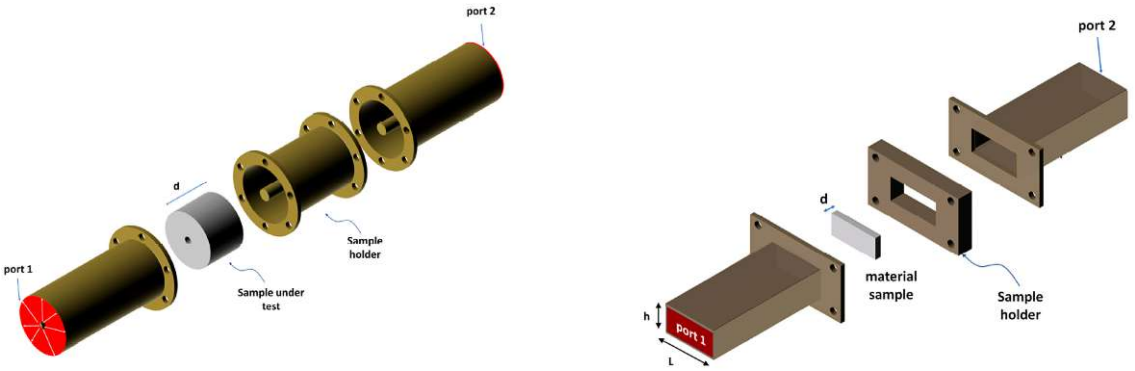

(a) (b)

Figure 1.8: Coaxial (a) and rectangular (b) waveguides with an inserted SUT. Figure from [25].

A particularly common resonator for measuring a material's permittivity is a CSRR. A CSRR is a resonator on a two-layer PCB, where two split rings are removed from the ground plane beneath a microstrip line. The ground plane thus consists of a split ring resonator (SRR)'s complement. The rings in CSRRs are most commonly square- or circular-shaped, but other shapes, such as hexagons, have also been used [26]. In the rest of this thesis, I focus exclusively on rectangular CSRRs.

Fig. 1.9 shows a microstrip-coupled CSRR on a PCB with coaxial launch connectors terminating the microstrip line. When using CSRRs for measuring a material's permittivity, the two connectors are connected to a vector network analyzer (VNA), which measures the S-parameters, as shown in Fig. 1.10a. The minimum for $|S_{21}|$ lies at the frequency $f_{\mathrm{res},0}$, the resonant frequency of the unloaded CSRR. When performing the same measurement while placing a sample on top of the CSRR, the resonant frequency and absolute value for S_{21} change. The new minimum for $|S_{21}|$ lies at $f_{\mathrm{res,MUT}}$, the resonant frequency of the loaded CSRR. Fig. 1.10b shows an example of this effect.

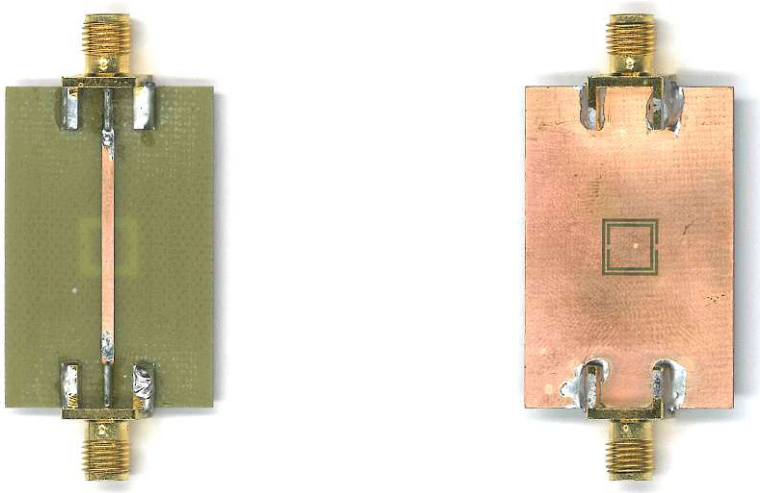

(a) (b)

Figure 1.9: CSRR on a PCB with coaxial launch connectors. Top layer (a) and bottom layer (b).

The frequency shift from $f_{\mathrm{res},0}$ to $f_{\mathrm{res,MUT}}$ is used to determine a material's ε_r'. The

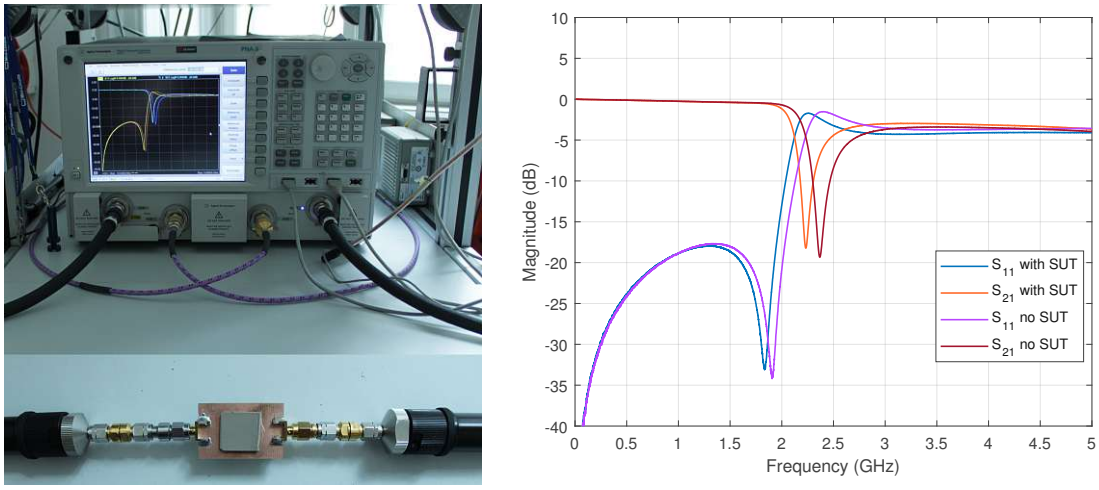

(a) Meausurement setup. **(b)** Results.

Figure 1.10: Measuring a CSRR's S-parameters using a VNA. Measurement setup (a). Effect of the SUT on the resonant frequency (b).

material's loss tangent is calculated by using both ε_r' and the Q-factor, which is derived from $|S_{21}|$.

1.3 Proposed Method Outline

CSRRs with a desired resonant frequency can easily be manufactured on a PCB and provide low-cost methods to measure an MUT's permittivity. This thesis introduces a new method of obtaining an MUT's complex permittivity from the measured S-parameters of loaded and unloaded CSRRs. As of the writing of this thesis, only four real numbers are used to determine the MUT's complex permittivity in the literature, the resonant frequency of the loaded and unloaded CSRRs, and the absolute values of S_{21} at those frequencies. This procedure discards the complex scattering matrix (S-matrix) in the vicinity of the resonant frequency, which I deem useful in acquiring more accurate results.

This thesis demonstrates how to measure an MUT's permittivity by exploiting the CSRR's equivalent circuit representation. The values for the elements in the equivalent circuit are obtained by exploiting the CSRRs' S-matrices over a wide frequency range, and minimizing a least-squares-based distance metric between the equivalent circuit and the simulated or measured CSRR. Instead of resorting to resonant frequency shifts and changes in $|S_{21}|$, I demonstrate how to measure an MUT's permittivity based on the changes in the values of the elements in a CSRR's equivalent circuit when loaded with an SUT. Equations that relate the changes in the values of the elements in a CSRR's equivalent circuit to the loading SUT's permittivity and loss tangent are formulated based on simulation results and verified using measurement data.

2 Modelling Complementary Split Ring Resonators

Since their introduction in 2004 [27], CSRRs have found many applications in the literature, including sensors for material characterization, measuring blood glucose levels, and as a tool for miniaturizing antennas on PCBs [26, 28, 29, 30, 31, 32]. Microstrip coupled CSRRs are made on two-layer PCBs. They consist of a microstrip line on the top layer, and a ground plane on the bottom layer, from which an SRR is removed. The ground plane is therefore an SRR's complement. The rings can be circular or rectangular. For the rest of this thesis, I consider only rectangular CSRRs unless stated otherwise.

So far, determining the elements is done in one of two ways: (i) By using an analytical model, such as in [33]. (ii) By assuming a lossless transmission line and solving equations that involve four frequencies, those of minimum and maximum transmission and reflection [31, 34, 35]. The solutions of either approach are validated by comparing them to the solutions of an FWS or measurements, though only for at most a few different CSRR sizes. How the equivalent circuit elements relate to the CSRR size according to FWS results over a range of CSRR sizes is yet to be documented.

For each size of the CSRR, I use the error metric to determine the values of each element. In particular, the values for each element are found when the error is minimized. The determined values for each element in the equivalent circuit are thus the solutions to an optimization problem. I proceed to investigate the resulting errors for various CSRR sizes and circuit models, to determine the circuit model with the lowest error. Having determined the one that approximates an FWS best, I study how each element of the equivalent circuit changes with respect to the CSRR size. I further use the error metric to show how much the error increases after varying each circuit element, which I call an element's sensitivity.

I introduce a study on equivalent circuit models for CSRRs, where microstrip-coupled rectangular CSRRs are simulated over a range of sizes using Ansys High Frequency Structure Simulator (HFSS), and the effect of the CSRR's size on every element in the equivalent circuit is discussed. Instead of relying on a few frequency points to determine the equivalent circuit's element values, I incorporate hundreds to thousands of frequency points and define the equivalent circuit elements as solutions to a least squares problem.

First, I define an error metric between two S-matrices, that of an HFSS simulation and that of an equivalent circuit, using the Frobenius norm. The frequency range that the

error metric takes into account spans a factor of four, with the frequency of minimum transmission of the microstrip-coupled CSRR as the geometric mean. The error metric fulfills two purposes: It serves to find optimal values for the elements in the equivalent circuits, i.e., I can determine the values for each element in an equivalent circuit by minimizing the resulting error. Further, it enables a fair comparison between different circuit models, i.e., after having optimized each element in each equivalent circuit model, better circuit models yield smaller errors.

For each size of the CSRR, I use the error metric to determine the values of each element. In particular, the values for each element are found when the error is minimized. The determined values for each element in the equivalent circuit are thus the solutions to an optimization problem. I proceed to investigate the resulting errors for various CSRR sizes and circuit models, to determine the circuit model with the lowest error. Having determined the one that approximates an FWS best, I study how each element of the equivalent circuit changes with respect to the CSRR size. I further use the error metric to show how much the error increases after varying each circuit element, which I call an element's sensitivity.

This chapter is structured as follows: In Section 2.1, I define the equivalent circuit models, the FWS of the CSRR, and my proposed error metric. In Section 2.2, I optimize the elements of each equivalent circuit to the FWS results and conclude which equivalent circuit performs best. I proceed to a detailed analysis on how the equivalent circuit's elements change with respect to the CSRR's size and which element is most sensitive to the error.

2.1 Design and Simulation

Fig. 2.1 shows the layout of the microstrip line and the CSRR on a large PCB. The dimensions from Fig. 2.1 are listed in Tab. 2.1. The substrate height and the copper thickness are 0.8 mm and 17 µm, respectively. The substrate material is FR-4, with a relative permittivity of 4.4 and a loss tangent of 0.02.

Table 2.1: Dimensions of the simulated CSRRs.

Property	a	b	c	d	g	w_{ms}
Length in mm	0.39	0.22	0.38	2.5–20.0	0.22	1.47

I generate the PCBs in HFSS according to the definitions in Fig. 2.1 and Tab. 2.1. Wave ports are used on each end of the microstrip line as excitations. Both ports are de-embedded to the center of the PCB, as indicated by the dashed line in Fig. 2.1.

Fig. 2.2 shows the HFSS results for S_{11} and S_{21}. The fundamental resonant frequency drops with increasing d. The CSRR with $d = 12$ mm was simulated up to a frequency that is high enough to show the second resonant frequency appearing at 6.5 times the fundamental resonant frequency. For the rest of this thesis, I consider only the fundamental resonant frequency, and ignore higher order resonant frequencies.

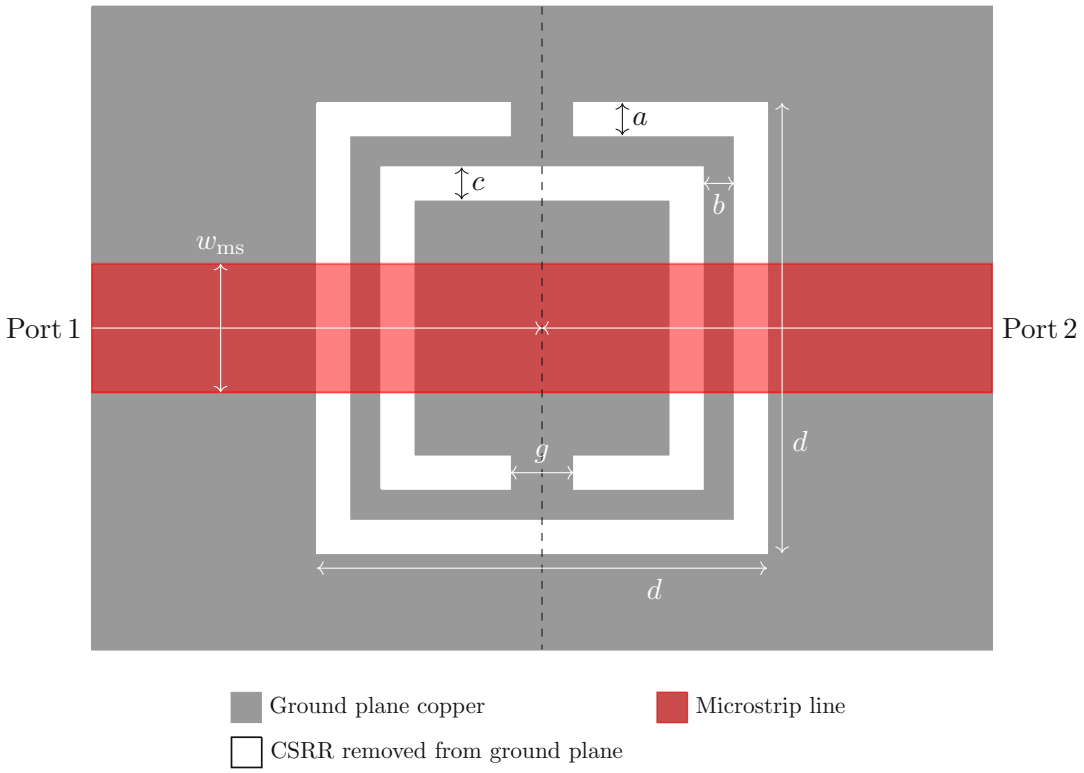

Figure 2.1: Top view of the PCB with a microstrip-coupled CSRR.

2.1.1 Equivalent Circuit Models

The circuit in Fig. 2.3 serves as the basis for the circuit model variations that I compare. The models differ in how the dashed elements are implemented. The microstrip lines, also used in [35], have a length of l_{Line}, and are implemented according to [36]. I expect the sign of l_{Line} to be negative, given that the reference planes of both ports are at the center of the structure in the FWS. This is equivalent to shifting the reference planes apart in the FWS by $2\,|l_{\mathrm{Line}}|$ and removing the microstrip lines in the equivalent circuit. Removing all dashed elements (replacing all series resistors with a short, and shunt capacitors and resistors with an open) corresponds to the equivalent circuit proposed in [33], aside from the microstrip line. The shunt capacitor C_{Neg} is an attempt to emulate the negative permittivity for microstrip lines where CSRRs are periodically removed from the ground plane [33, 35]. The shunt resistors G_{Cpl} and G_{Res} take losses into account [26]. I further investigate the influence of the series resistors R_{Res} and R_{Line}. The following variations are studied: The elements C_{Neg}, G_{Cpl}, and G_{Res} are either allowed to have nonzero values for the capacitance and conductance, or they are replaced with an open, resulting in eight variations. The series resistors R_{Res} and R_{Line} can be implemented in three different ways: They can be replaced by a short, have a value that is constant over frequency, or they can obey the skin effect, using the relations

$$R_{\mathrm{Line}}(f) = R_{\mathrm{Line},0}\sqrt{\frac{f}{1\,\mathrm{GHz}}}, \tag{2.1}$$

$$R_{\mathrm{Res}}(f) = R_{\mathrm{Res},0}\sqrt{\frac{f}{1\,\mathrm{GHz}}}, \tag{2.2}$$

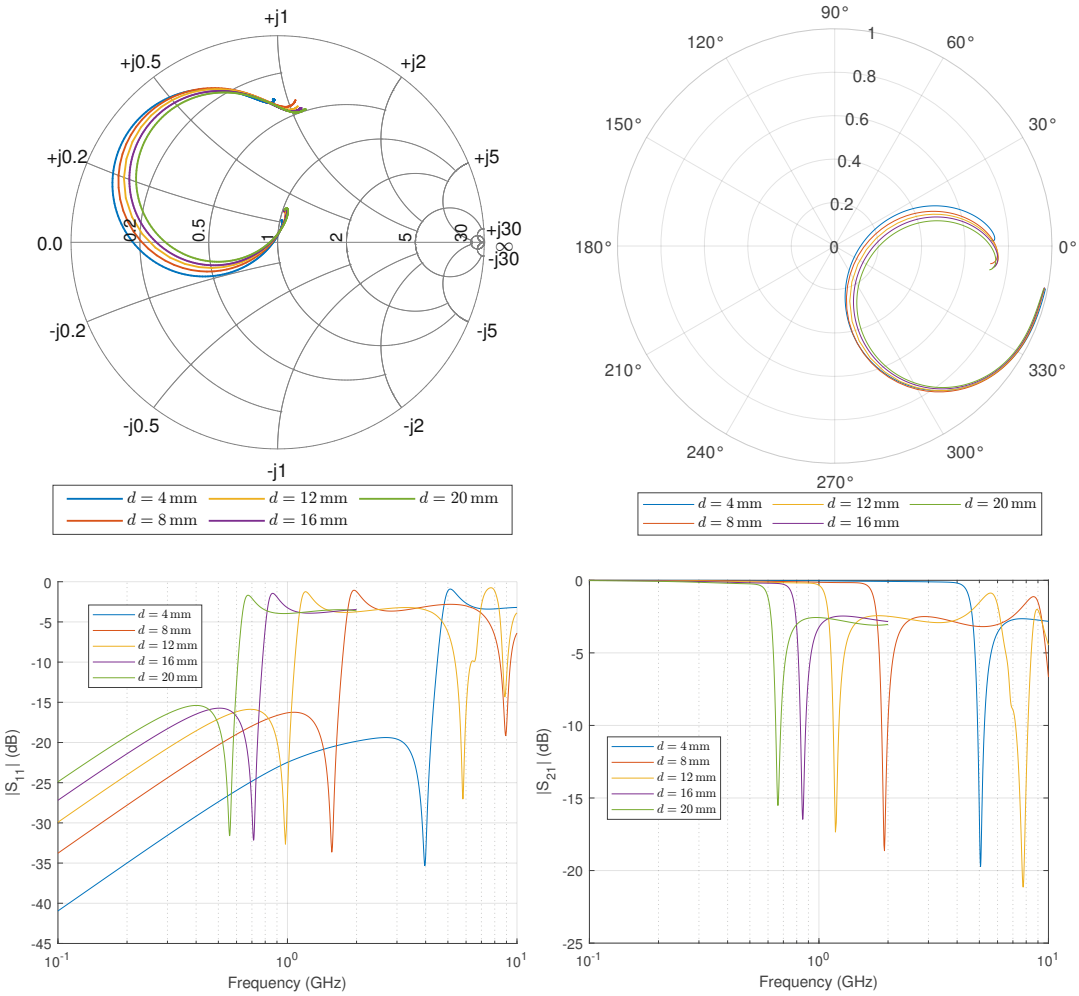

Figure 2.2: S_{11} (left) and S_{21} (right) for different values of d.

resulting in 9 variations. In total, there are 72 possible circuits.

2.1.2 Optimization

The following procedure is performed independently for every value of d: The S-matrix of the HFSS simulation $S^{(\mathrm{EM})}$ is computed over a frequency range that contains over 160 linearly spaced frequency points f_k in the interval $[f_{\mathrm{res}}/2, 2f_{\mathrm{res}}]$, where f_{res} is the frequency where $\left|S_{21}^{(\mathrm{EM})}\right|$ has its first local minimum. The equivalent circuit parameters are found by minimizing the error E, defined as

$$E = \frac{1}{k_{\max} - k_{\min} + 1} \sum_{k=k_{\min}}^{k_{\max}} \left\| S^{(\mathrm{EM})}(f_k) - S^{(\mathrm{EC})}(f_k) \right\|_F^2, \tag{2.3}$$

where $\left|S_{21}^{(\mathrm{EC})}\right|$ is the S-matrix for the equivalent circuit, and the definitions $f_{k_{\min}} = f_{\mathrm{res}}/2$ and $f_{k_{\max}} = 2\, f_{\mathrm{res}}$ apply.

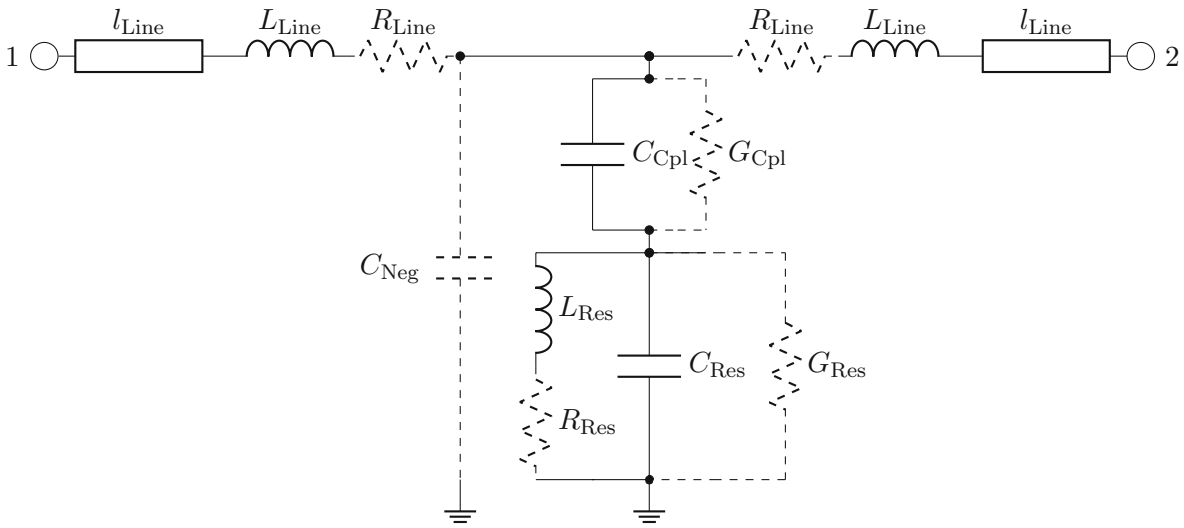

Figure 2.3: Equivalent circuit for a microstrip-coupled CSRR. Dashed elements are implemented in different ways.

2.2 Results

In this section, the equivalent circuit parameters are always optimized according to the procedure described in Section 2.1.2.

2.2.1 Equivalent Circuit Comparison

Fig. 2.4 shows the error E for all 72 circuit variations. Eleven of these are marked and are defined in Tab. 2.2. The lossless models (Models 1 and 2) have the largest error (above $4 \cdot 10^{-3}$). Adding only C_{Neg} or R_{Line} (Models 2, 3, and 4) does not significantly reduce E. Adding G_{Res}, G_{Cpl}, or R_{Res} reduces E by an order of magnitude (Models 7, 8, and 9). Using all elements and making the series resistors R_{Res} and R_{Line} obey the skin effect yields the smallest error (Model 5). However, incorporating C_{neg} causes the system to be overdetermined and does not noticeably reduce the error. The overdetermination causes some of the circuit elements to have relations with d that follow no obvious patterns. An example is shown in Fig. 2.5. Furthermore, when including both R_{Res} and G_{Res} in Model 11, the optimized values for R_{Res} go to zero, except at two values for d, where the error spikes up. These are indications that Model 11 is also overdetermined. Model 10, which involves neither C_{Neg} nor R_{Res}, yields similar results as Model 5, despite lacking two degrees of freedom. In conclusion, Model 10 from Tab. 2.2 represents a CSRR in an FWS most accurately. The equivalent circuit for Model 10 is shown in Fig. 2.6.

2.2.2 Optimal Equivalent Circuit

In this subsection, Model 10 from Tab. 2.2 is studied in more detail. Fig. 2.7 shows a comparison between the results for S_{11} and S_{21} from HFSS and Model 10 for $d = 7\,\text{mm}$.

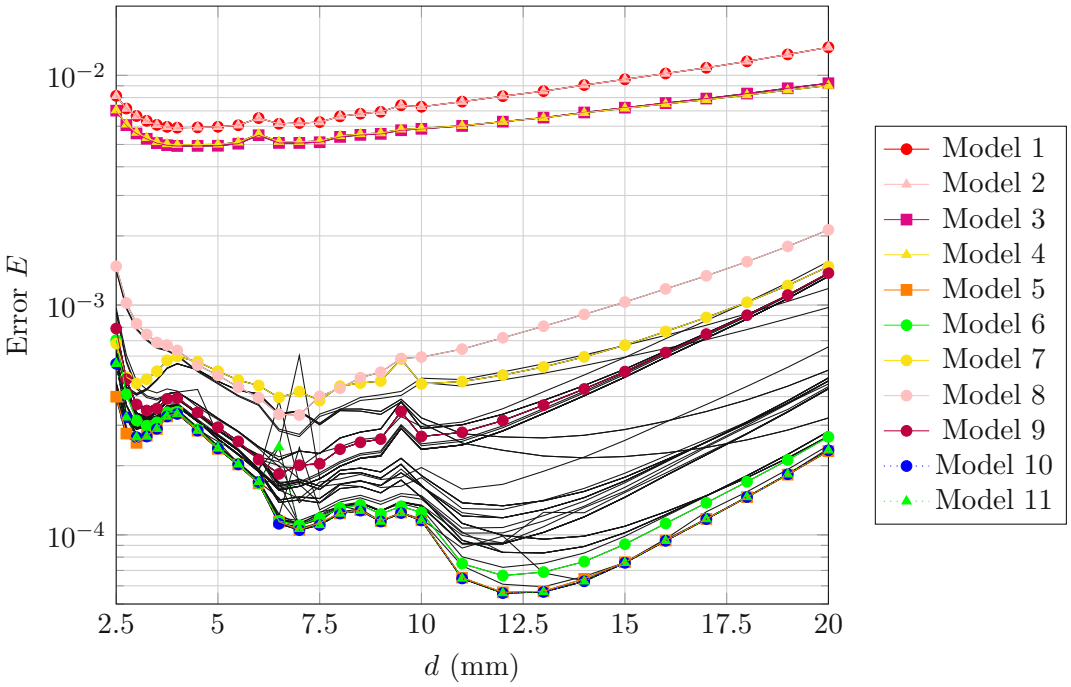

Figure 2.4: Error with respect to d for all circuit models. Models from Tab. 2.2 are in the legend.

Table 2.2: Implementations of dashed circuit elements for selected circuit models highlighted in Fig. 2.4.

Model	C_{Neg}	G_{Cpl}	G_{Res}	R_{Line}	R_{Res}
Model 1	open	open	open	short	short
Model 2	$<0\,\text{F}$	open	open	short	short
Model 3	open	open	open	const. over f	short
Model 4	open	open	open	$\propto \sqrt{f}$	short
Model 5	$<0\,\text{F}$	$>0\,\text{S}$	$>0\,\text{S}$	$\propto \sqrt{f}$	$\propto \sqrt{f}$
Model 6	open	$>0\,\text{S}$	open	$\propto \sqrt{f}$	$\propto \sqrt{f}$
Model 7	open	open	$>0\,\text{S}$	short	short
Model 8	open	$>0\,\text{S}$	open	short	short
Model 9	open	open	open	short	const. over f
Model 10	open	$>0\,\text{S}$	$>0\,\text{S}$	$\propto \sqrt{f}$	short
Model 11	open	$>0\,\text{S}$	$>0\,\text{S}$	$\propto \sqrt{f}$	$\propto \sqrt{f}$

The magnitude of S_{21} reaches a minimum at 2.3 GHz. The error E is therefore minimized between 1.15 GHz and 4.6 GHz. The weight function is the reciprocal of the number of frequencies used to minimize E in the range from 1.15 GHz to 4.6 GHz and zero outside of it. The trajectories for S_{11} and S_{21} in the Smith chart and polar plot are only shown in the frequency range from 1.15 GHz to 4.6 GHz. Between 1.15 GHz and 4.6 GHz, the S-parameters of the HFSS simulations and Model 10 show a good agreement.

The results for l_{Line}, G_{Res}, G_{Cpl}, ad $R_{\text{Line},0}$ are shown in Fig. 2.8. The negative sign for l_{Line} means that the CSRR acts as a lumped element with a length of $2\,|l_{\text{Line}}|$. The monotonic increase of $|l_{\text{Line}}|$ with d is consistent with the growing length of the CSRR

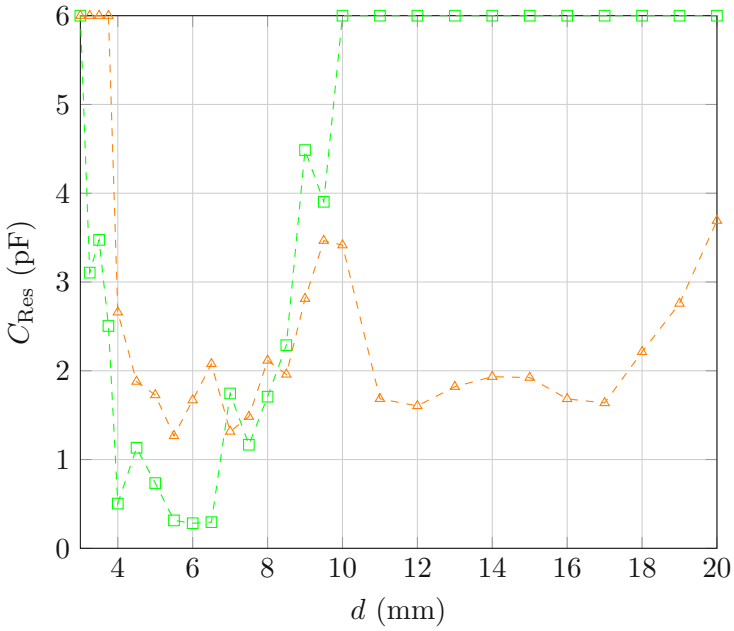

Figure 2.5: Examples for values of C_{Res} with respect to d for some models that involve C_{Neg}.

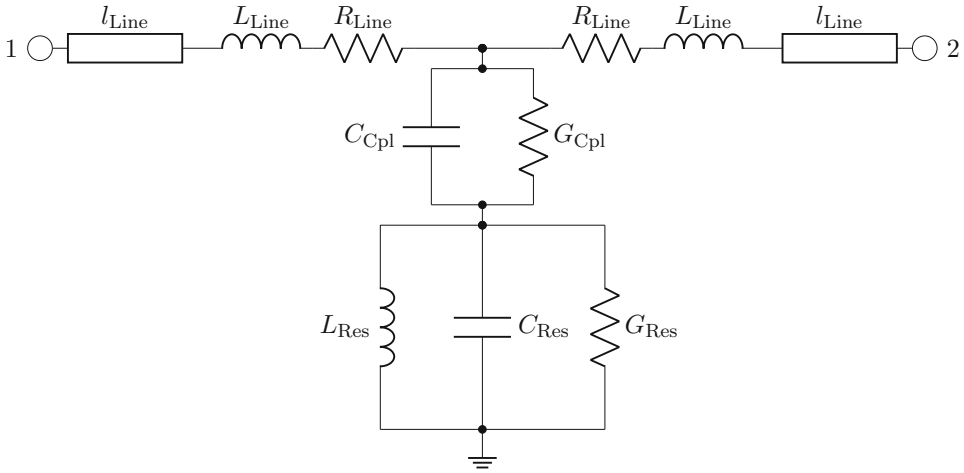

Figure 2.6: Optimal circuit for a microstrip-coupled CSRR (Model 10).

parallel to the microstrip line.

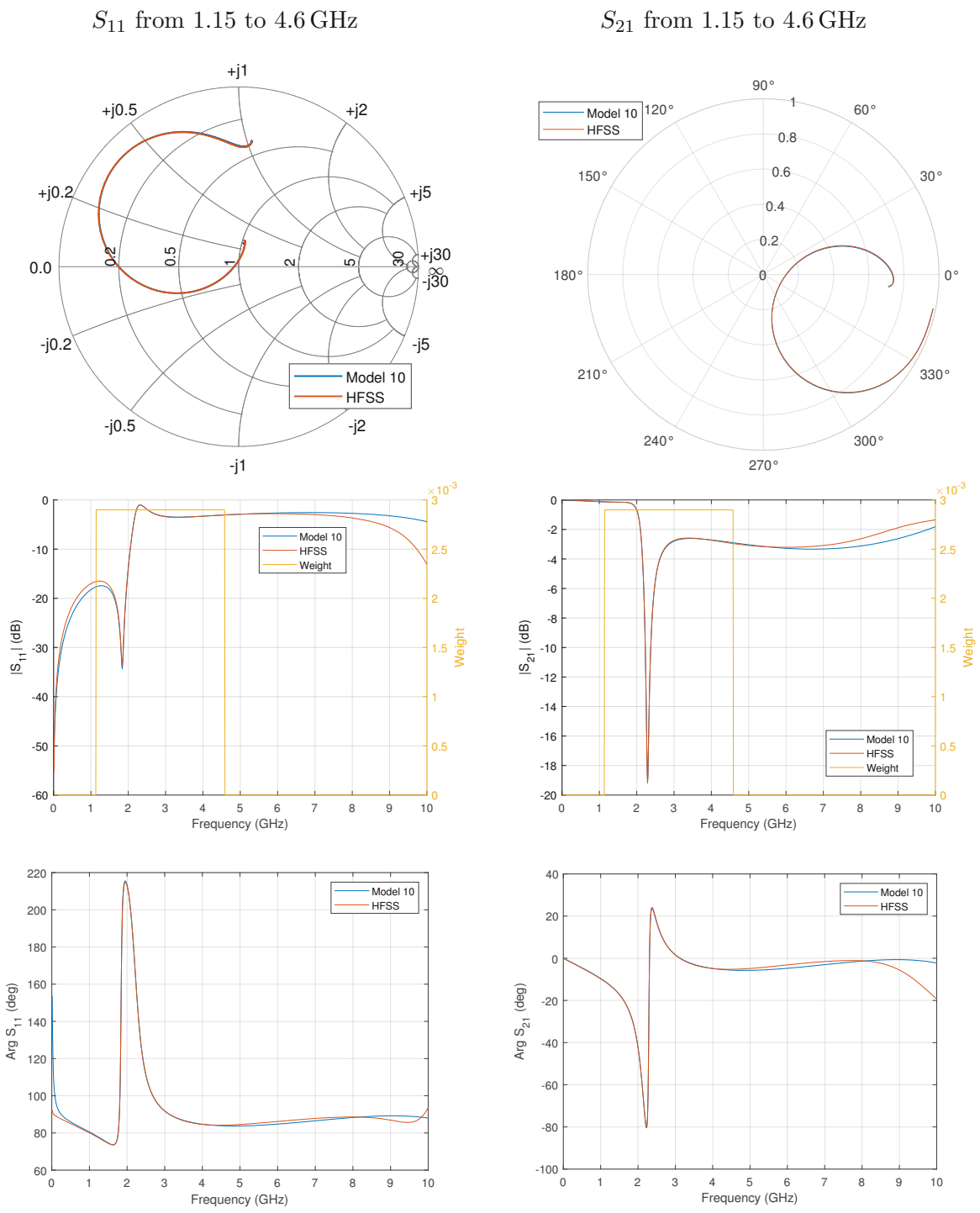

Figure 2.7: Comparison of S_{11} (left) and S_{21} (right) between the HFSS simulations and the solution for Model 10 for $d = 7\,\text{mm}$.

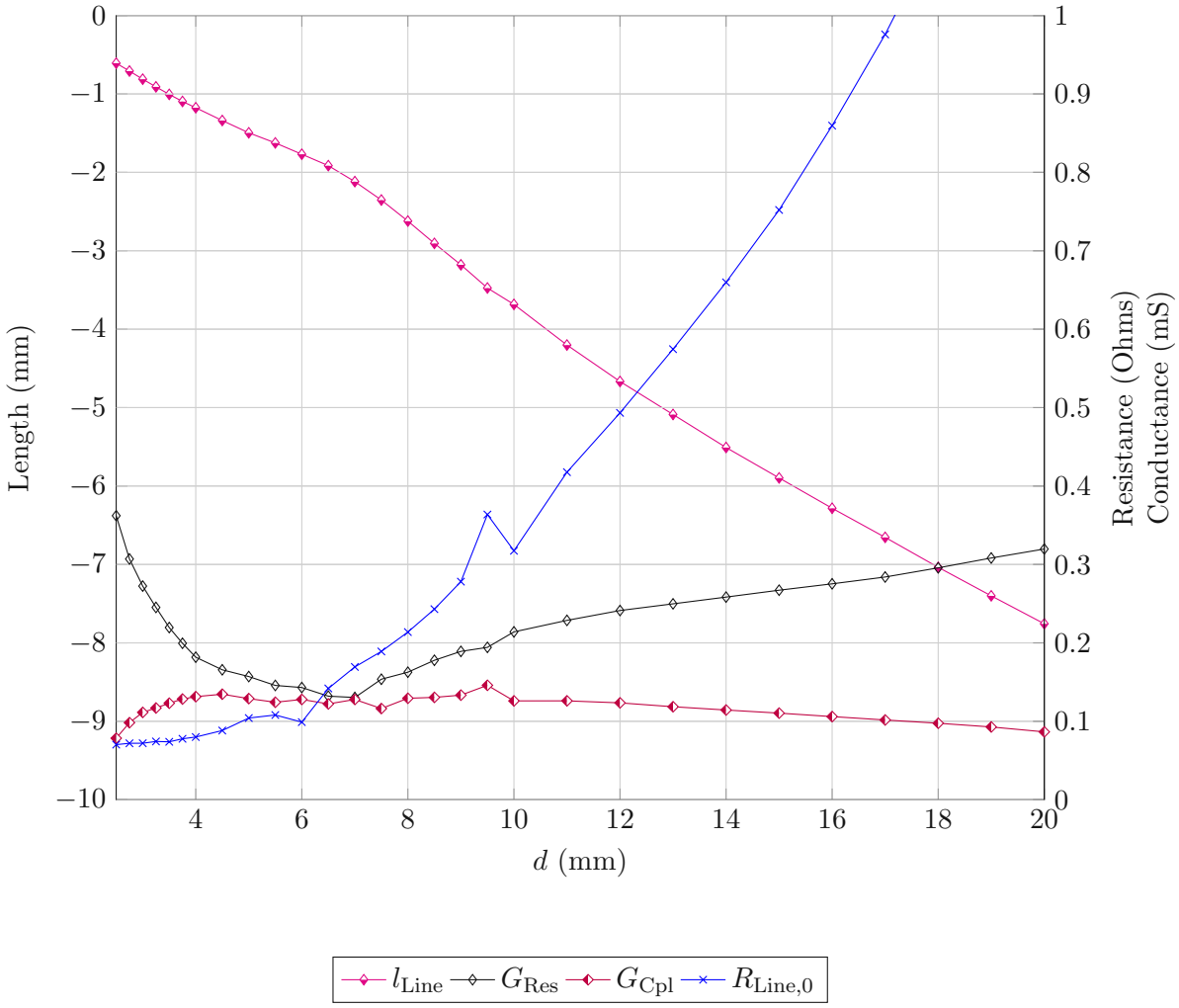

Figure 2.8: Length of the microstrip line with respect to d.

The results for C_{Line}, C_{Cpl}, L_{Line}, and L_{Res} are shown in Fig. 2.9. The values for C_{Line} and L_{Line} grow approximately linearly with d. The same can be said for L_{Res}, C_{Res}, and $|l_{\text{Line}}|$ except for the interval between approximately 3 mm and 10 mm. In this region, the quality factor Q of the unloaded resonator, which consists only of L_{Res}, C_{Res}, and G_{Res}, reaches a peak of 51 at $d = 7\,\text{mm}$. By comparison, an eigenmode simulation in HFSS of the same PCB without the microstrip line yields $Q = 55$, with conductor losses considered.

I further investigate how E responds to a change to each parameter from the equivalent circuit. For each parameter p of the equivalent circuit, I define the sensitivity $s\,(p)$ as

$$s\,(p) = \frac{E_p - E}{E \cdot \frac{\Delta p}{p}}, \tag{2.4}$$

where E_p is the error from (2.3), when the parameter p is substituted by $p + \Delta p$. The values for $s\,(p)$ are shown in Fig. 2.10 for $\Delta p = 0.01\,p$. The results show that the error is most sensitive towards L_{Res}, and that $s\,(L_{\text{Res}})$ is four to ten times greater than $s\,(C_{\text{res}})$. Furthermore $s\,(C_{\text{Cpl}}) > s\,(C_{\text{Res}})$ means that the coupling effect from the microstrip line

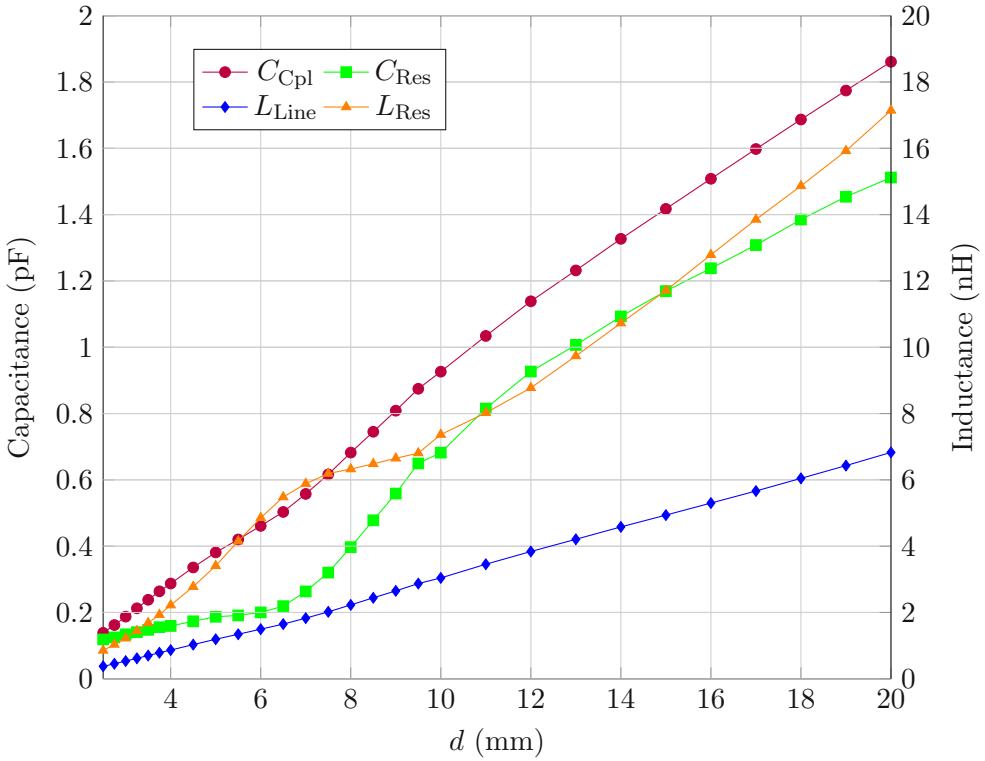

Figure 2.9: Values for C_{Cpl}, C_{Res}, L_{Line}, L_{Res} with respect to d.

has a greater impact on E than the CSRR's capacitance C_{Res}. This implies that $s\,(C_{\mathrm{Cpl}})$ and $s\,(C_{\mathrm{Res}})$ should be optimized jointly.

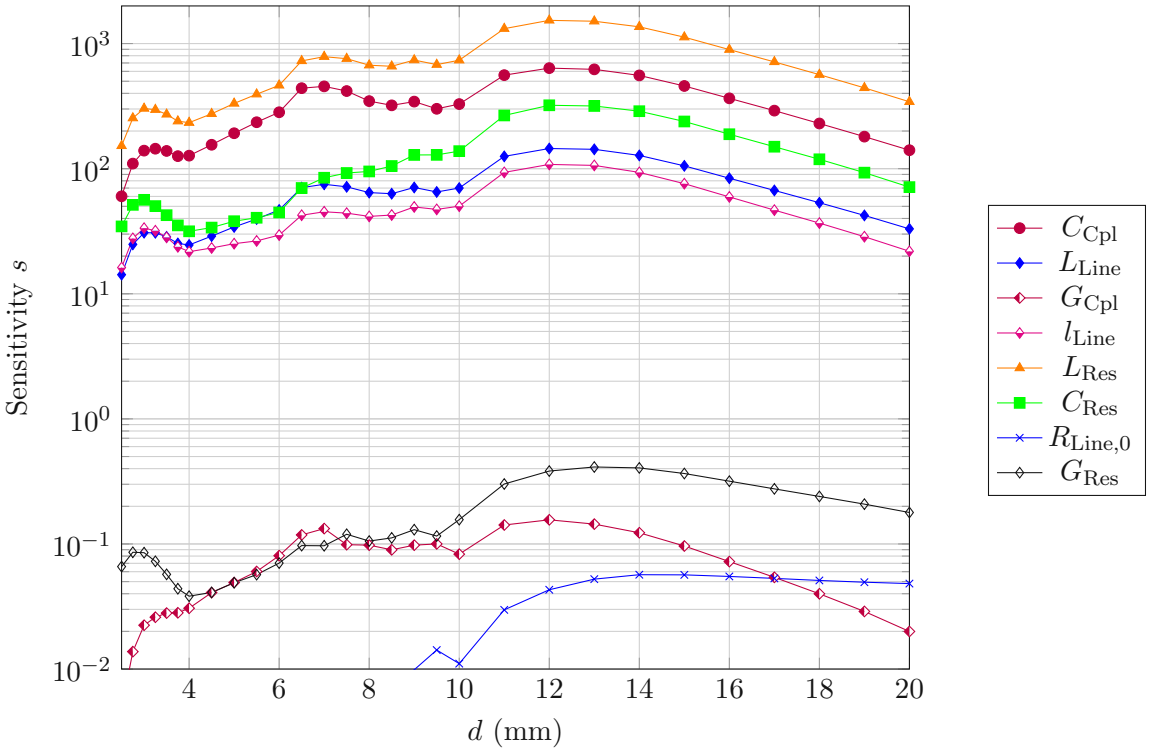

Figure 2.10: Sensitivities $s\,(p)$ with respect to d, where p is one of the parameters from the legend.

3 Simulation-Based Permittivity Determination

Chapter 2 introduced an improved model for determining an equivalent circuit for CSRRs. This chapter provides a simulation-based method to describe how the presence of an SUT changes the parameters in the CSRR's equivalent circuit. This chapter concludes with a method to estimate the SUT's relative complex permittivity and an accompanying error bound.

This thesis aims to provide a simple method that allows characterizing dielectrics using the S-matrices obtained from measurements where a CSRR is loaded with an SUT. Before delving into measurements, I develop a simulation-backed method to determine an SUT's complex permittivity. Simulations offer a distinct advantage over measurements because they allow for arbitrary values of ε_r, instead of being restricted to materials that can be obtained easily, as is the case with measurements. I simulate one CSRR backed by SUTs with a variety of sample heights, permittivites, and loss tangents that are common in RF engineering. I derive a procedure for calculating an SUT's permittivity using the simulation results and provide estimates for uncertainties in the estimated values for ε_r' and $\tan\delta$.

The second step is to apply the optimization algorithm from Chapter 2 to the S-parameters from the simulation results of a loaded CSRR. I assume the same circuit topology for loaded as for unloaded CSRRs. In the optimized circuit model from Chapter 2, the parameters in the equivalent circuit show a smooth variation over the unloaded CSRR's size, with most parameters showing monotonic behavior with respect to d. I used that criterion to rule out other circuit models, where the values for some elements showed no apparent relation to the CSRR's size. I deemed models with such a behavior overdetermined and thus ruled them out. The question, which of the circuit elements is affected by an SUT, poses a similar problem. It is possible to minimize the error metric from (2.3) by optimizing the values for all elements in the equivalent circuit. However, such an approach might result in an overdetermined system. Such an overdetermination can be avoided by constraining some of the elements of a loaded CSRR to those of an unloaded CSRR with the same shape and PCB substrate.

While Chapter 2 explored which elements to incorporate into the equivalent circuit at all, this chapter examines which circuit elements are suitable to exhibit changes caused by the SUT, and which elements must be constrained to those of an unloaded CSRR. I provide

an analysis that shows which elements one must constrain, and which to optimize anew, and formulate a new optimization algorithm for loaded CSRRs. I determine the equivalent circuit for all FWSs that contain a CSRR loaded with a variety of SUTs using the newly derived optimization method.

In the remainder of the chapter, I discuss the relations between the equivalent circuit elements and the SUT's complex permittivity. I further derive expressions for ε_r' and $\tan\delta$ and estimations for their uncertainty.

3.1 Field Simulations

Fig. 3.1 shows the design of a simulated CSRR in HFSS. The PCB is similar to that from Chapter 2, with the added SUT adjacent to the ground plane. Tab. 3.1 contains the dimensions of the simulated CSRR using the definitions from Fig. 2.1. The PCB is enclosed by an air box that is 80 mm wide and 80 mm high. The simulations are carried out using the broadband solution, from 10 MHz to 9 GHz, with a frequency step of 1 MHz, using an interpolated sweep type.

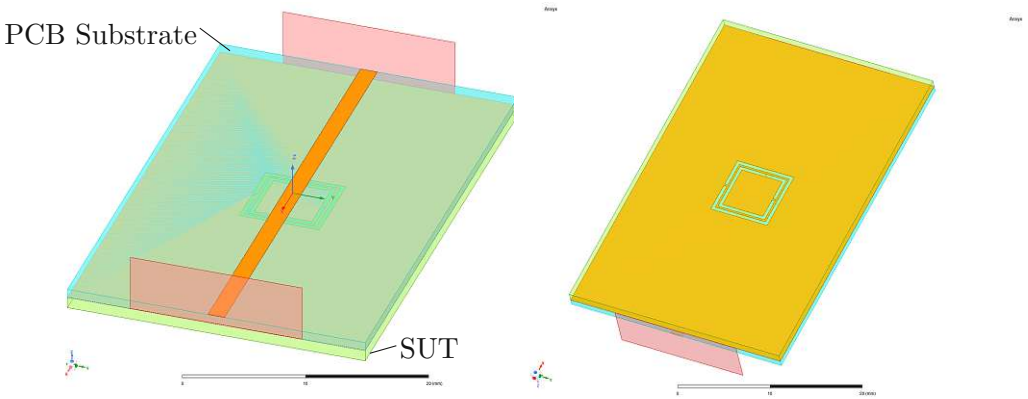

(a) Top Layer **(b)** Bottom Layer

Figure 3.1: Microstrip coupled CSRRs on a PCB, loaded with an SUT in HFSS. Top layer (a), and bottom layer (b).

Table 3.1: Dimensions of the simulated CSRR.

Property	PCB width	PCB length	a	b	c	d	g	w_{ms}
Length in mm	26	40	0.39	0.22	0.38	7.0	0.22	1.47

Table 3.2: Values for h_{SUT}, ε_r' and $\tan\delta$. Models with all combinations were simulated.

$$\frac{h_{\mathrm{SUT}}}{1\,\mathrm{mm}} \in \{0.10,\ 0.25,\ 0.46,\ 1.00,\ 2.15,\ 4.64,\ 10.00\}$$
$$\varepsilon_r' \in \{2,\ 4,\ 7,\ 10\}$$
$$\tan\delta \in \{0.001,\ 0.005,\ 0.01,\ 0.05,\ 0.1\}$$

Quantization noise can degrade the accuracy of FWS results. In order to minimize the quantization noise, the convergence and meshing criteria are set according to Tab. 3.3.

Table 3.3: Convergence and meshing criteria for the used HFSS simulations.

Maximum Delta S	0.001
Minimum Number of Passes	20
Minimum Converged Passes	2
Maximum Refinement per Pass	30%
Order of Basis Functions	Mixed Order

3.1.1 Results

Fig. 3.2 shows $|S_{21}|$ for the variations from Tab. 3.2 with an SUT thickness of 10 mm. An increase in ε_r' causes a decrease in the resonant frequency, and an increase in $\tan\delta$ decreases the Q-factor. The relation between the frequency shift and ε_r' is also stated as [28]

$$f_{\mathrm{res,SUT}}^{-2} - f_{\mathrm{res},0}^{-2} \propto \varepsilon_r, \tag{3.1}$$

where $f_{\mathrm{res},0}$ and $f_{\mathrm{res,SUT}}$ are the frequencies at which $|S_{21}|$ of the unloaded and loaded resonator reach their first local minimum. Fig. 3.2 shows that an increase in $\tan\delta$ also shifts $f_{\mathrm{res,SUT}}$ to a higher frequency. Thus, relying only on $f_{\mathrm{res,SUT}}$ to determine ε_r' disregards useful information. Similarly, the value that $|S_{21}|$ reaches at $f_{\mathrm{res,SUT}}$ increases with both ε_r' and $\tan\delta$.

3.2 Equivalent Circuit Variations

This section studies how the circuit elements change when the CSRR is loaded with an SUT. The CSRR's equivalent circuit is shown in Fig. 3.3. Applying the method from Chapter 2 to the unloaded CSRR yields the equivalent circuit parameters in Tab. 3.4. Four different approaches are compared to determine which elements must be constrained to those of the unloaded CSRR and which must be optimized anew. Tab. 3.5 contains a description of four different models. The constrained elements preserve their values from Tab. 3.4. The values for the optimized elements are determined with the method from Chapter 2.

Table 3.4: Optimized equivalent circuit parameters for the unloaded CSRR.

R_{Line}	C_{Line}	L_{Line}	G_{Cpl}	l_{Line}	L_{Res}	C_{Res}	G_{Res}
64 m Ω	0.55 pF	1.8 nH	0.12 mS	−2.1 mm	5.7 nH	0.26 pF	0.13 mS

In the following sections, results are color- and marker-coded to allow for a more straightforward discussion of results. Colors correspond to constant values of ε_r', and markers correspond to constant values of $\tan\delta$. This means that whenever bundles of curves with the same color appear, a particular property is strongly dependent on the SUT's ε_r'. Conversely, tight bundles of curves with the same marker indicate a strong dependence of that property on the SUT's $\tan\delta$.

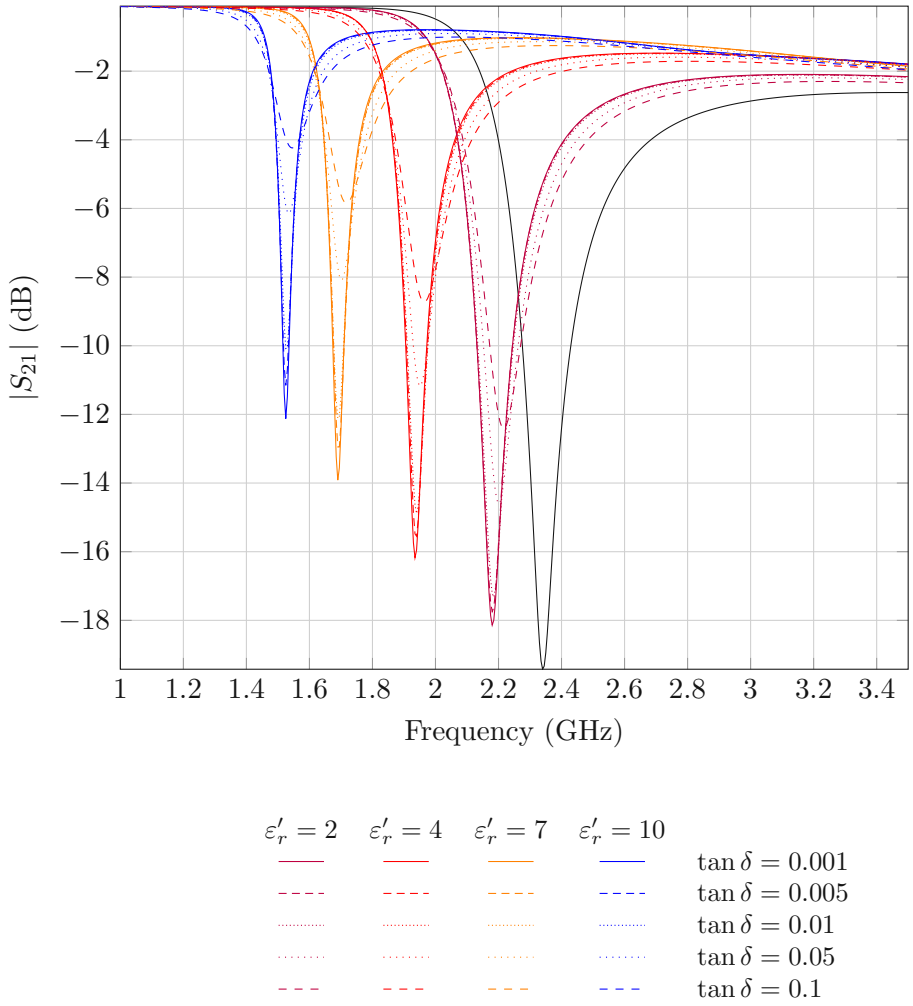

Figure 3.2: $|S_{21}|$ for different combinations of the SUT's ε'_r and $\tan\delta$ for $h_{\mathrm{SUT}} = 10\,\mathrm{mm}$. The black line represents the unloaded CSRR.

3.2.1 Variation 1 - Variation in All Parameters

Fig. 3.4 shows the results for L_{Res} for all variations from Tab. 3.2. For $\varepsilon'_r = 2$ and $\varepsilon'_r = 4$, L_{Res} increases monotonically with h_{SUT}. For $\varepsilon'_r = 7$ and $\varepsilon'_r = 10$, L_{Res} increases monotonically with h_{SUT}, as long as h_{SUT} does not exceed 1 mm. The nonmonotonic relations justify the conclusion that a variation in all parameters overdetermines the system when h_{SUT} exceeds the height of the PCB substrate. Fig. 3.5 shows the results for l_{Line}, which show a strong correlation to the values for L_{Res}.

Given that the SUT backs the ground plane, I constrain the elements R_{Line}, L_{Line}, and l_{Line}.

3.2.2 Variation 2 - Variation in the Resonator and Coupling Capacitor

Fig. 3.6 shows that C_{Cpl} is almost independent of the SUT's ε'_r and $\tan\delta$ as long as $h_{\mathrm{SUT}} \leq 10\,\mathrm{mm}$. The sudden drops of C_{Cpl} for $\varepsilon'_r = 10$ coincide with the sudden jump

Table 3.5: Variations in which circuit parameters to optimize and which to constrain.

Variation	Optimized Elements	Constrained Elements
Variation 1	G_{Res}, G_{Cpl}, C_{Res}, C_{Cpl}, R_{Line}, L_{Line}, L_{Res}, l_{Line}	none
Variation 2	G_{Res}, C_{Res}, C_{Cpl}, L_{Res}	R_{Line}, L_{Line}, l_{Line}, G_{Cpl}
Variation 3	G_{Res}, C_{Res}, L_{Res}	R_{Line}, L_{Line}, l_{Line}, G_{Cpl}, C_{Cpl}
Variation 4	G_{Res}, C_{Res}	R_{Line}, L_{Line}, l_{Line}, G_{Cpl}, C_{Cpl}, L_{Res}

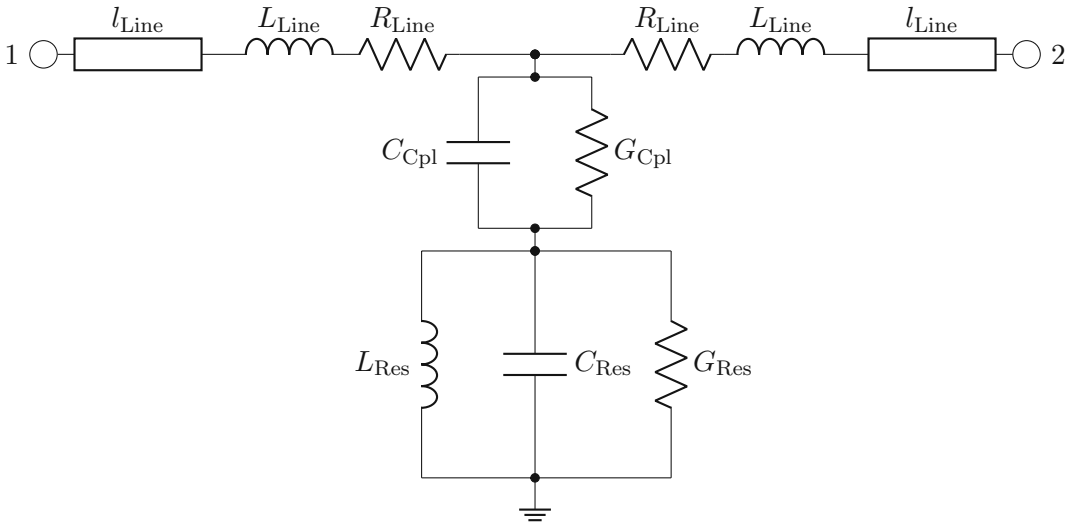

Figure 3.3: Equivalent circuit model for the CSRR.

in C_{Res} (shown in Fig. 3.7) which grows monotonically with h_{SUT} before the jump. I conclude that optimizing C_{Cpl} results in overdetermination, and justify constraining C_{Cpl} to the value of the unloaded CSRR.

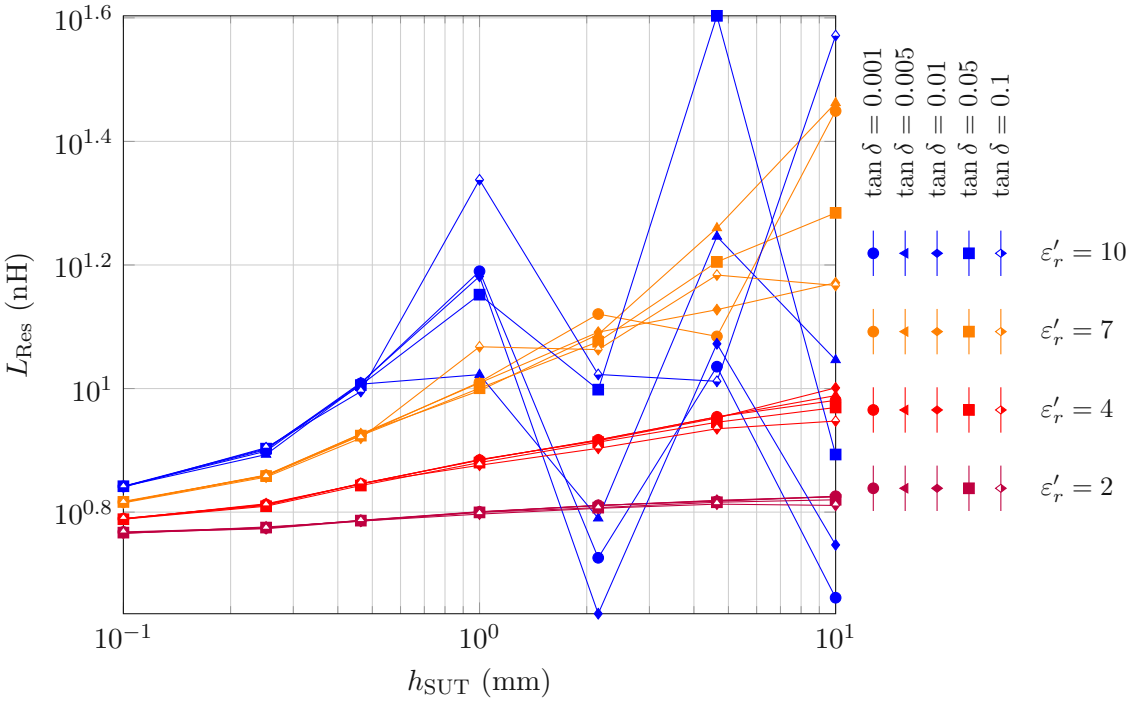

Figure 3.4: L_{Res} for different combinations of the SUT's ε'_r and $\tan\delta$ with Variation 1 from Tab. 3.5.

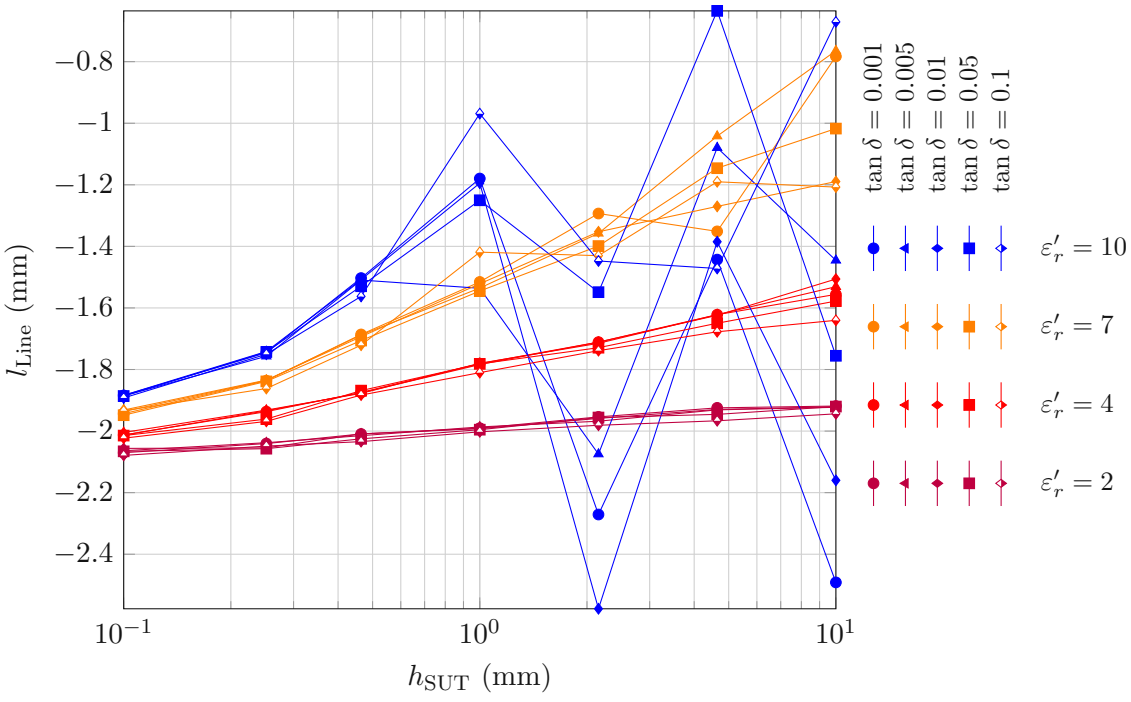

Figure 3.5: l_{Line} for different combinations of the SUT's ε'_r and $\tan\delta$ with Variation 1 from Tab. 3.5.

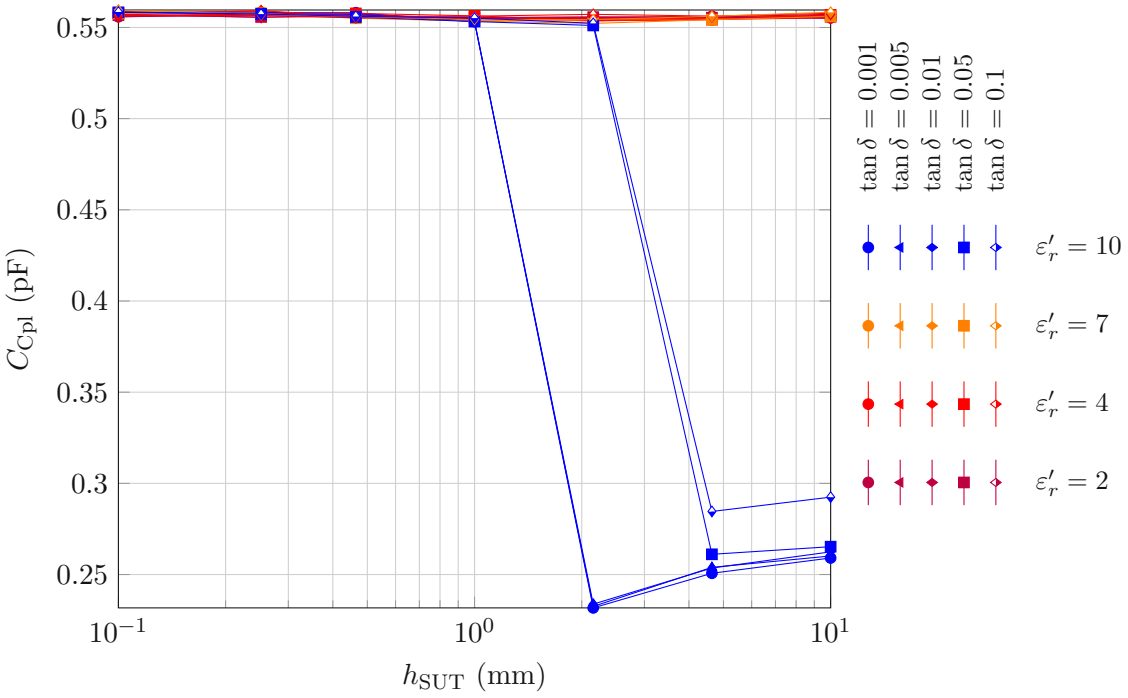

Figure 3.6: C_{Cpl} for different combinations of the SUT's ε'_r and $\tan\delta$ with Variation 2 from Tab. 3.5.

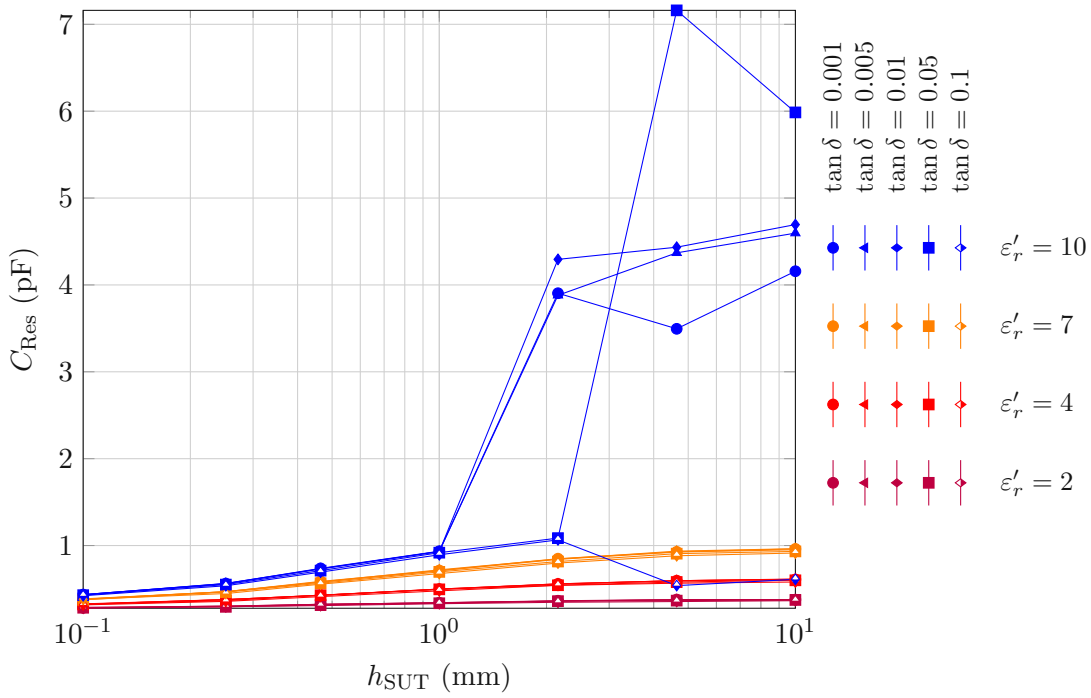

Figure 3.7: C_{Res} for different combinations of the SUT's ε'_r and $\tan\delta$ with Variation 2 from Tab. 3.5.

3.2.3 Variations 3 and 4 - Variation In Only the Resonator

Fig. 3.8 shows the results for C_{Res} for Variation 3 from Tab. 3.5. The curves for C_{Res} form tight bundles for constant values of ε_r', rising monotonically with h_{SUT}, proving C_{Res} a suitable quantity to calculate the SUT's ε_r'.

Fig. 3.9 shows that G_{Res} grows monotonically with h_{SUT}, except for SUTs with a loss tangent of 0.001. One explanation of this effect is that the CSRR's Q-factor increases when loaded with an SUT whose loss tangent is lower than that of the substrate. Indeed, the loaded resonator's Q-factor, given as

$$Q_{\mathrm{Res}} = \sqrt{\frac{C_{\mathrm{Res,SUT}}}{L_{\mathrm{Res}}}} \cdot \frac{1}{G_{\mathrm{Res,SUT}}}, \tag{3.2}$$

increases when the CSRR is loaded with a sample whose loss tangent is below that of the PCB substrate, and, conversely, decreases when the CSRR is loaded with a sample whose loss tangent is greater. This effect can be observed in Fig. 3.10, which moreover shows that an increase in the SUT's ε_r' increases the magnitude by which Q_{Res} is raised or reduced. Reoptimizing the three elements G_{Res}, L_{Res}, and C_{Res} results in a decrease in G_{Res} when Q_{Res} is large enough.

Fig. 3.11 shows that the results for L_{Res} vary slightly over h_{SUT} and the SUT's permittivity. I therefore constrain the values for L_{Res} to that from Tab. 3.4, i.e., use only Variation 4 from Tab. 3.5 to determine the SUT's permittivity in Section 3.3. Plots for C_{Res} and G_{Res} for Variation 4 are skipped in this subsection.

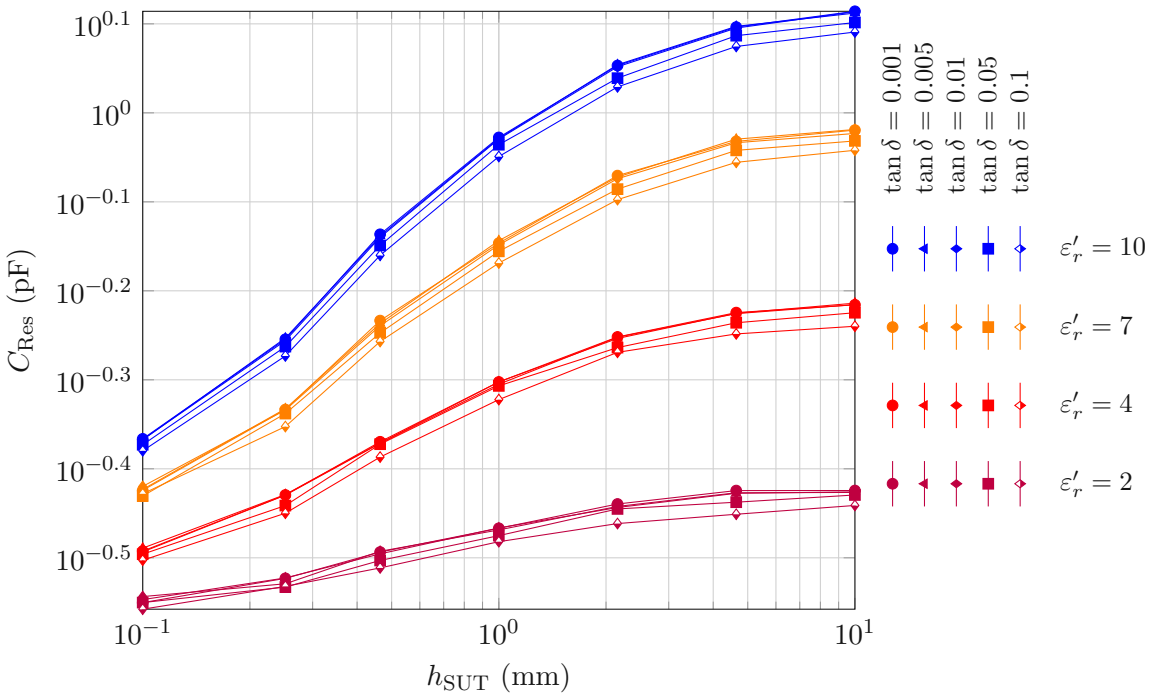

Figure 3.8: C_{Res} for different combinations of the SUT's ε_r' and $\tan\delta$ with Variation 3 from Tab. 3.5.

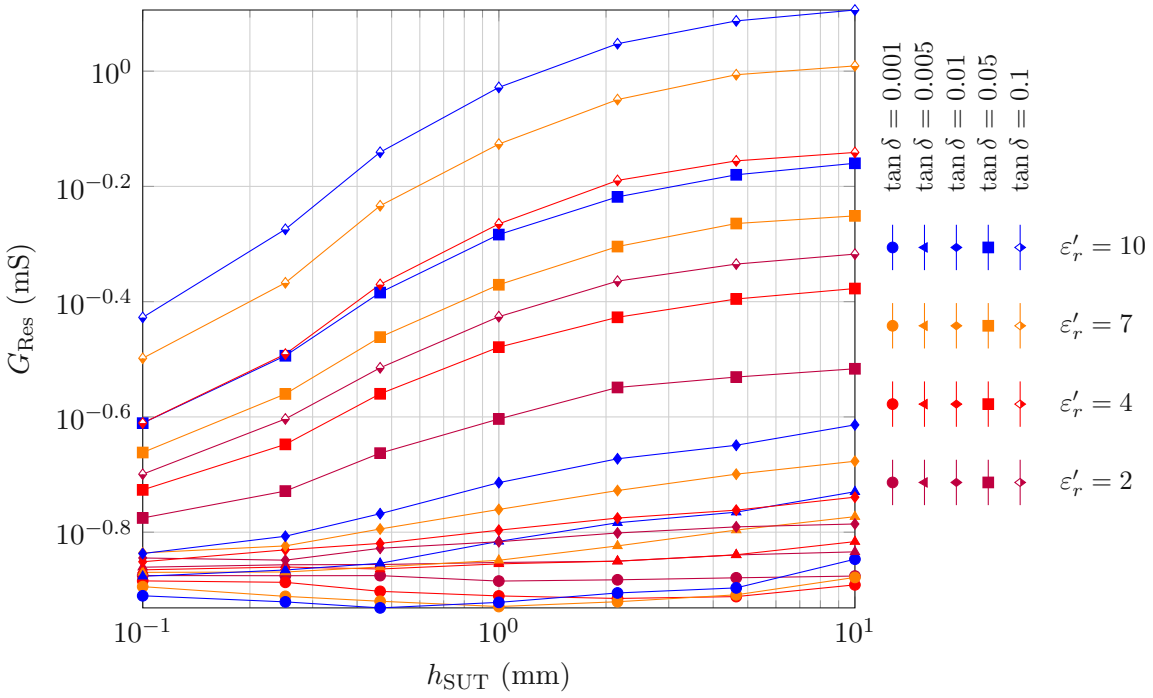

Figure 3.9: G_{Res} for different combinations of the SUT's ε'_r and $\tan\delta$ with Variation 3 from Tab. 3.5.

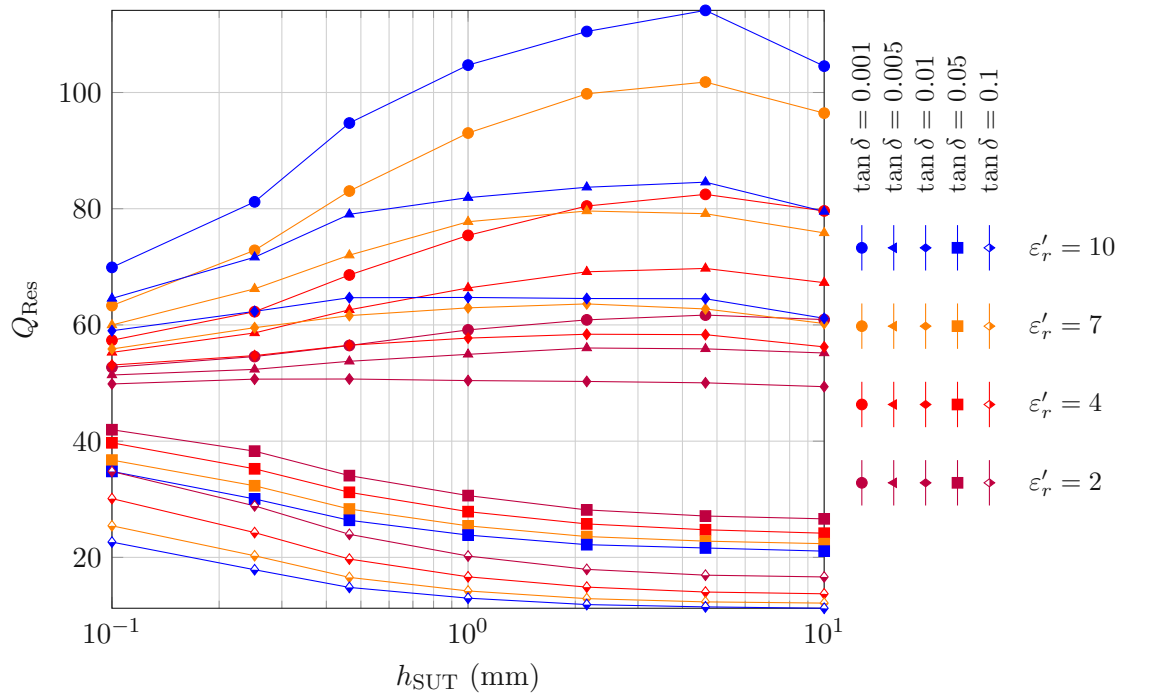

Figure 3.10: Q for different combinations of the SUT's ε'_r and $\tan\delta$ with Variation 3 from Tab. 3.5.

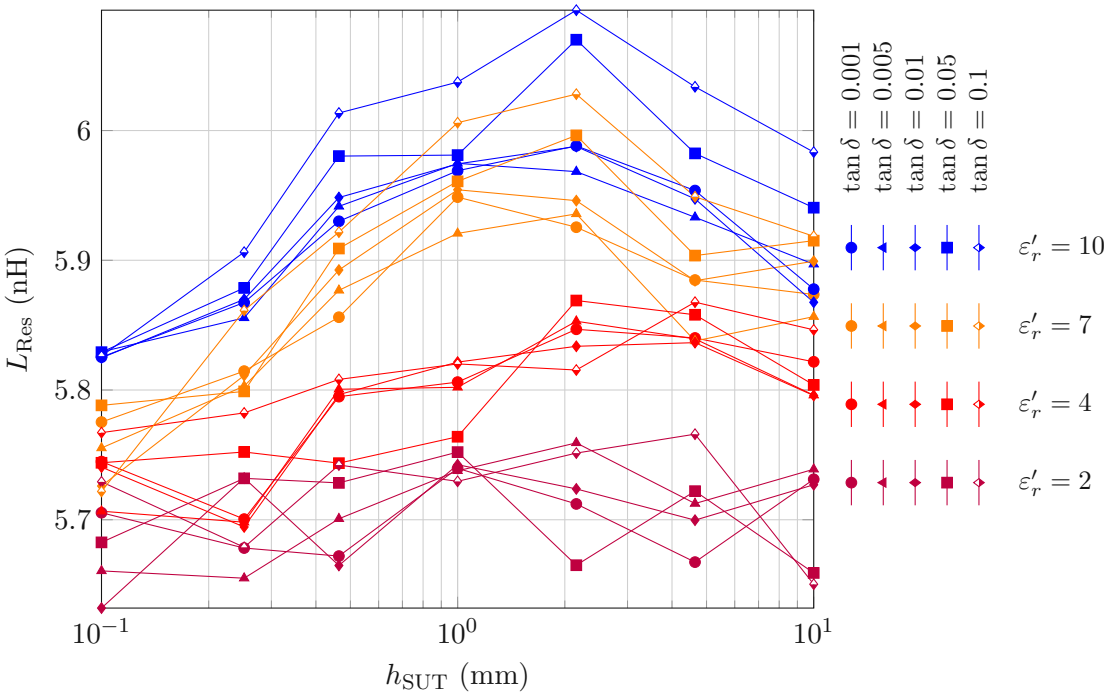

Figure 3.11: L_{Res} for different combinations of the SUT's ε'_r and $\tan\delta$ with Variation 3 from Tab. 3.5.

3.3 Determining an SUT's Complex Permittivity

The results for the equivalent circuit elements from Section 3.2 indicate that optimizing every circuit element of a loaded CSRR leads to an overdetermined system. By contrast, optimizing only C_{Res} and G_{Res}, i.e., Variation 4 from Tab. 3.5 yields more stable results. In this section, I discuss how to express an MUT's ε_r and loss tangent using values for the equivalent circuit elements.

3.3.1 Real Permittivity

The capacitance C_{Res} increases with rising $\varepsilon_r\prime$. One suitable parameter to determine an SUT's permittivity is given with

$$S = \frac{C_{\text{Res,SUT}} - C_{\text{Res,0}}}{C_{\text{Res,0}}}, \tag{3.3}$$

where the parameters $C_{\text{Res,0}}$ and $C_{\text{Res,SUT}}$ correspond to C_{Res} of the unloaded and loaded CSRR, respectively. Hence, S represents the ratio between the increase in C_{Res} caused by the SUT to C_{Res} when no SUT is present.

Fig. 3.12 shows the resulting values for S as function of h_{SUT} for all variations from Tab. 3.2. The curves for constant ε_r' form tight bundles that do not overlap. On top of that, the value for S appears to converge at $h_{\text{SUT}} = 10\,\text{mm}$, except for the case where $\varepsilon_r' = 2$ and $\tan\delta = 0.1$ and 0.05, where S slightly dips down.

The parameter S represents the ratio between the increase in C_{Res} caused by the SUT to C_{Res} when no SUT is present. When loading the CSRR with an SUT, the SUT displaces air in the CSRR's vicinity, and raises the permittivity by the MUT's susceptibility χ, defined as

$$\chi = \varepsilon_r' - 1. \tag{3.4}$$

This raises the question of whether the susceptibility of an SUT backing a CSRR is proportional to the increase of the CSRR's capacitance. The answer lies in the ratio S/χ, which is shown in Fig. 3.13, where the curves for S/χ appear as an overlapping bundle, re-enforcing the direct proportionality between S and χ. Hence, I express the relation between ε_r' and S as

$$\varepsilon_r' \approx a\,(h_{\text{SUT}}) \cdot S + 1. \tag{3.5}$$

An estimate for a at $h_{\text{SUT}} = (10\,\text{mm})$ is obtained by minimizing the root mean square relative error (RMSRE) $E_{\varepsilon_r'}$ between the known values for ε_r and their approximation according to (3.5) as

$$E_{\varepsilon_r'} = \sqrt{\frac{1}{NM}\sum_{n=1}^{N}\sum_{m=1}^{M}\left|\frac{a\cdot S\left(\varepsilon_{r,n}', \tan\delta_m\right) + 1 - \varepsilon_{r,n}'}{\varepsilon_{r,n}'}\right|^2}, \tag{3.6}$$

where k and m are indices for elements in the sets for ε_r' and $\tan\delta$ from Tab. 3.2. Minimizing $E_{\varepsilon_r'}$ from (3.6) yields

$$a\,(10\,\text{mm}) = 2.123. \tag{3.7}$$

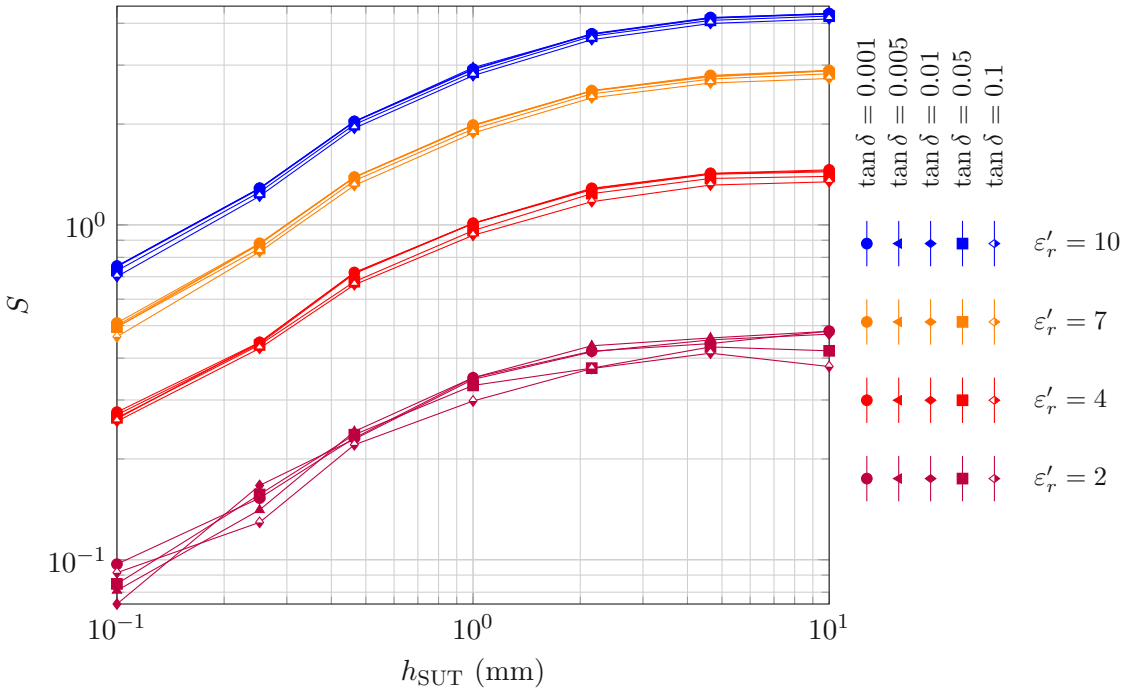

Figure 3.12: Resulting values for S for each combination of h_{SUT}, ε'_r, and $\tan\delta$ after the optimizations.

Substituting for (3.5) yields the approximation

$$\varepsilon'_r \approx 2.123 \cdot S + 1 \tag{3.8}$$

for $h_{\mathrm{SUT}} = 10\,\mathrm{mm}$ with an RMSRE of $E_{\varepsilon'_r} = 3\%$. The relative errors for the different values for ε'_r and $\tan\delta$ are given in Tab. 3.6.

The fact the S flattens out after a certain threshold of h_{SUT} offers one advantage over the methods discussed in Chapter 1: The SUT thickness does not have to be known, as long as it exceeds a certain threshold.

Table 3.6: Relative errors for ε'_r at $h_{\mathrm{SUT}} = 10\,\mathrm{mm}$ using (3.8).

		ε'_r			
		2	4	7	10
$\tan\delta$	0.001	1.23%	2.64%	2.23%	1.00%
	0.005	1.18%	2.12%	1.88%	1.00%
	0.01	0.17%	1.60%	2.01%	0.60%
	0.05	5.25%	0.77%	0.19%	0.61%
	0.1	9.84%	3.51%	2.58%	2.34%

The simulations show that an SUT's susceptibility can be approximated as a linear function of S. Therefore, ε'_r can be accurately derived using the values for S alone. The residual error is below 10% for a variety of combinations of ε'_r and $\tan\delta$.

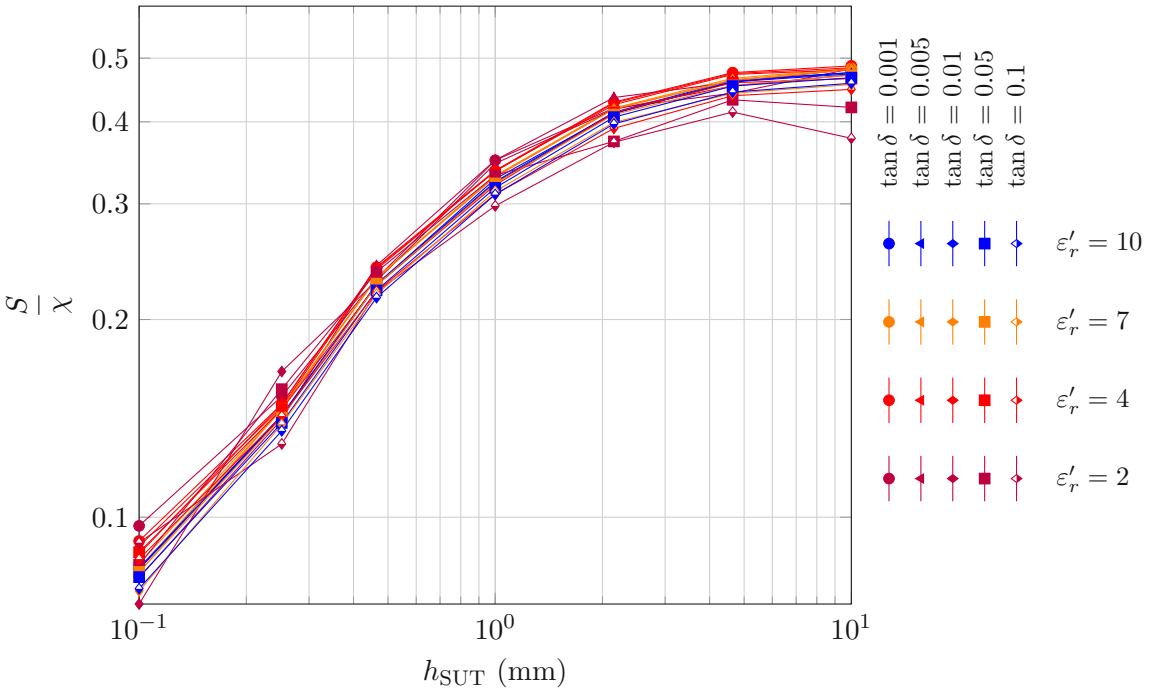

Figure 3.13: Values for S from Fig. 3.12 divided by χ.

3.3.2 Loss Tangent

Unlike the permittivity's real part, the SUT's loss tangent is not a function of any individual circuit parameter. In other studies, $\tan\delta$ is linked to the resonator's Q-factor and the SUT's ε'_r [26, 37]. I link the SUT's $\tan\delta$ to a variable $\tilde{Q}^{-1}$, which I define as

$$\tilde{Q}^{-1} = \sqrt{\frac{L_{\mathrm{Res}}}{C_{\mathrm{res,SUT}} - C_{\mathrm{Res,0}}}} \cdot \left(G_{\mathrm{res,SUT}} - G_{\mathrm{Res,0}}\right), \tag{3.9}$$

where the parameters $C_{\mathrm{Res,0}}$ and $C_{\mathrm{Res,SUT}}$ correspond to C_{Res} of the unloaded and loaded CSRR respectively. The parameters $G_{\mathrm{Res,0}}$ and $G_{\mathrm{Res},SUT}$ correspond to G_{Res} of the unloaded and loaded CSRR respectively. Fig. 3.14 shows the values for $\tilde{Q}^{-1}$. Curves with different colors and the same marker form bundles that do not overlap, indicating that $\tilde{Q}^{-1}$ is a suitable property to determine the SUT's $\tan\delta$. Similar as for ε'_r, I establish the relation

$$\tan\delta \approx b\left(h_{\mathrm{SUT}}\right) \cdot \tilde{Q}^{-1} \tag{3.10}$$

for $h_{\mathrm{SUT}} = 10\,\mathrm{mm}$ and estimate b by minimizing the root mean square error (RMSE) $E_{\tan\delta}$ defined as

$$E_{\tan\delta} = \sqrt{\frac{1}{NM}\sum_{n=1}^{N}\sum_{m=1}^{M}\left|b \cdot \tilde{Q}^{-1}\left(\varepsilon'_{r,n}, \tan\delta_m\right) - \tan\delta_m\right|^2}. \tag{3.11}$$

Minimizing the error in (3.11) yields

$$b\left(10\,\mathrm{mm}\right) = 1.244 \tag{3.12}$$

and substituting for (3.10) yields

$$\tan\delta \approx 1.244 \cdot \tilde{Q}^{-1} \tag{3.13}$$

for h_{SUT} with $E_{\tan\delta} = 2.6 \cdot 10^{-3}$.

Tab. 3.7 contains the absolute errors for $\tan\delta$ when using the approximation in (3.13). When the loss tangent of the SUT becomes small compared to that of the PCB substrate, $\tilde{Q}^{-1}$ can reach negative values. For example, $\tilde{Q}^{-1}$ becomes negative for $\tan\delta = 10^{-3}$ and $\varepsilon'_r = 4$. Minimizing the RMSRE when $\tilde{Q}^{-1}$ can obtain both positive and negative values for the same $\tan\delta$ leads to meaningless results. I rather hypothesize that the absolute error in measuring $\tan\delta$ is proportional to the PCB substrate's loss tangent.

The RMSE $E_{\tan\delta}$ is equal to $2.6 \cdot 10^{-3}$, and the largest error from Tab. 3.7 is $5.7 \cdot 10^{-3}$. Thus, the absolute measurement uncertainty for determining an SUT's loss tangent is shown to be smaller than the loss tangent of the PCB substrate by a factor of at least 4.

Table 3.7: Absolute Errors for $\tan\delta$ for $h_{\mathrm{SUT}} = 10\,\mathrm{mm}$ when using the approximation in (3.13).

		ε'_r			
		2	4	7	10
$\tan\delta$	0.001	$0.9 \cdot 10^{-3}$	$1.6 \cdot 10^{-3}$	$1.0 \cdot 10^{-3}$	$0.1 \cdot 10^{-3}$
	0.005	$1.3 \cdot 10^{-3}$	$1.9 \cdot 10^{-3}$	$1.0 \cdot 10^{-3}$	$0.1 \cdot 10^{-3}$
	0.01	$1.6 \cdot 10^{-3}$	$2.3 \cdot 10^{-3}$	$1.5 \cdot 10^{-3}$	$0.0 \cdot 10^{-3}$
	0.05	$0.9 \cdot 10^{-3}$	$5.0 \cdot 10^{-3}$	$2.7 \cdot 10^{-3}$	$0.6 \cdot 10^{-3}$
	0.1	$5.1 \cdot 10^{-3}$	$5.7 \cdot 10^{-3}$	$0.4 \cdot 10^{-3}$	$4.5 \cdot 10^{-3}$

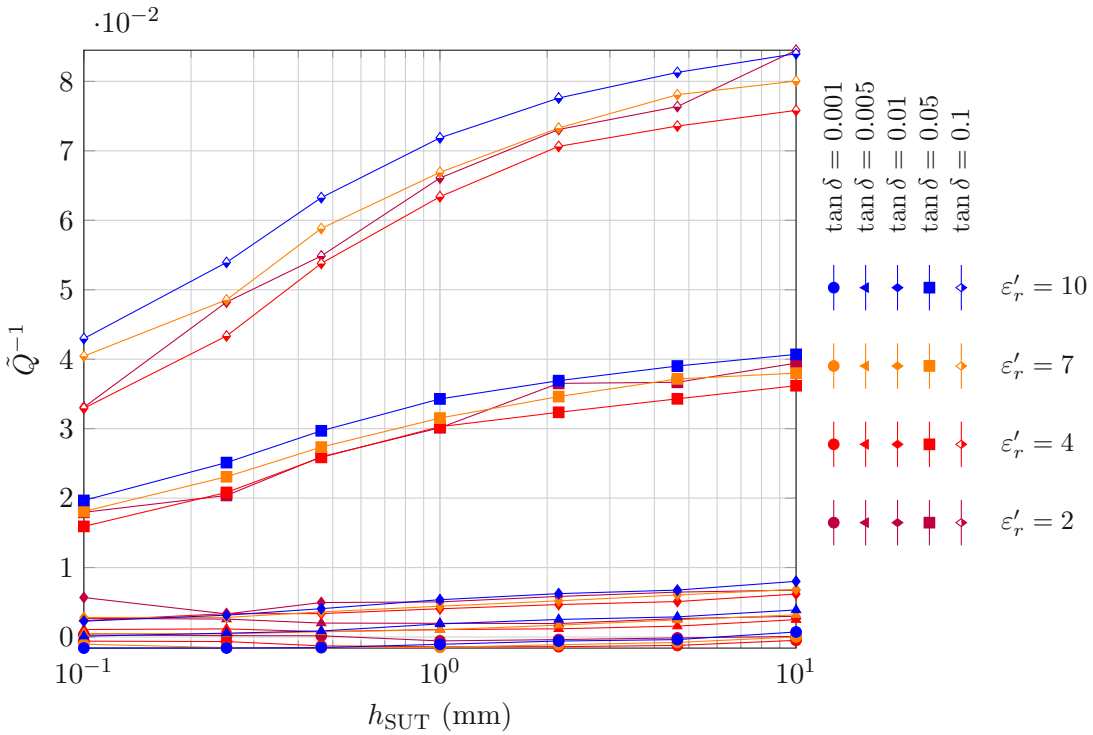

Figure 3.14: $\tilde{Q}^{-1}$ for different combinations of the SUT's ε'_r and $\tan\delta$.

4 Experimental Test Fixture

Chapter 3 introduced a simulation-backed method to measure an MUT's complex permittivity. This chapter describes the simulation-assisted design of a test fixture to verify that method experimentally, which is done later in Chapter 5. The test fixture is a PCB with 0.8 mm thick FR-4 as a substrate, and contains multiple CSRRs with different resonant frequencies around which materials are characterized. The layout of the PCB is concluded after considering the following three factors.

(i) The size and amount of CSRRs. The complex permittivity of any material is frequency-dependent. The result of any ε_r measurement using a CSRR is only valid around a specific frequency. I make the simplifying assumption that the measured value for the MUT's ε_r is valid around the resonant frequency of the loaded CSRR. The resonant frequency of an unloaded CSRR is approximately proportional to d^{-1}, where d is the CSRR's side length as shown in Fig. 2.1. The CSRR's resonant frequency further decreases when loaded with an SUT. For example, loading the CSRR from Chapter 3 with a 10 mm thick SUT with $\varepsilon'_r = 10$ reduces the resonant frequency by 35%. The choice of the CSRR's size, therefore, decides the frequency range for which the measured value of ε_r applies.

(ii) The thru, reflect, line (TRL) calibration kit. Determining a CSRR's equivalent circuit requires the reference planes for both ports to be at the center of the CSRR. One suitable calibration method to shift the reference planes to an arbitrary position on the PCB is the TRL calibration. The TRL calibration requires additional microstrip line elements. To ensure proper calibration, the substrate for the CSRRs must have the same permittivity as the substrate for the line elements belonging to the TRL calibration kit. Placing the TRL calibration kit and all CSRRs on the same PCB ensures that this condition is always met.

(iii) The end launch connector footprint. Microstrip lines provide a strong coupling to CSRRs due to the strong electric field perpendicular to the ground plane [33]. The test-fixture contains multiple microstrip-coupled CSRRs. The microstrip lines on the PCB must be connected to a VNA in order to measure the CSRR's S-parameters. VNAs typically use coaxial cables as transmission lines. In order to connect the PCB with the VNA, the microstrip lines must be terminated with a connector that can be connected to a coaxial cable at the edge of the PCB. Such a connector is called an end launch connector. The end launch connector is soldered onto both layers of the PCB in a section of the PCB called the footprint. In order to de-embed the connectors in the TRL calibration, all connectors on the PCB must have S-parameters that are either similar or small in

magnitude compared to the S-parameters of the CSRRs. Because the connectors are soldered to the PCB by hand, they all exhibit different S-parameters. The connectors' $|S_{11}|$ parameters must therefore be minimized in order for them to be small compared to the CSRRs' $|S_{11}|$.

The rest of this chapter is organized as follows: Section 4.1 explains the design of a suitable footprint for the coaxial launch connector. Section 4.2 specifies the TRL calibration kit. The size and amount of CSRRs is concluded in Section 4.3. Section 4.4 concludes the design and shows photos of a manufactured text fixture.

4.1 Footprint Optimization

The end launch connector fulfills a central role. It converts the TEM wave from the coaxial waveguide to the quasi-TEM mode on the microstrip line and vice-versa. Unavoidably, the connector reflects some of the energy of the incident wave. Furthermore, the connector together with its footprint — a resonant structure — radiate a significant fraction of the accepted power at specific frequencies. A good footprint minimizes both effects.

The end launch connectors used for this test fixture are Pasternack PE44206 connectors [38]. Although the manufacturer provides a footprint for the connector, there are two reasons why I decide to design my own. First, the connector slightly extends beyond the recommended footprint on the top layer of the PCB [38]. This can cause the solder to coat areas that should not be covered on the top layer of the PCB. Secondly, the manufacturer does not specify a substrate or permittivity for a suitable substrate.

Fig. 4.1a shows a model of a PCB with a microstrip line and a Pasternack PE44206 connector on each end in HFSS. The inside of the connector is modeled as a coaxial transmission line until it touches the edge of the PCB. The connectors are fed using wave ports that are de-embedded shortly before the edge of the PCB, as shown in Fig. 4.2.

The entire model is symmetric along the XY plane. The symmetry allows to split it in half along the XY plane, and apply the symmetry bound to the symmetry plane. Fig. 4.1b shows the model from Fig. 4.1a split in half along the XY plane. This results in less computational complexity. When the ports are split in half to take advantage of the symmetry, one must set the port impedance multiplier to 0.5. Fig. 4.3 shows a top view schematic of the footprint. The individual dimensions were optimized with the help of HFSS's tune tool. Tab. 4.1 contains the dimensions for the optimized footprint. Fig. 4.4 shows the magnitudes for S_{11} and S_{22} for the connector with the optimized footprint. The magnitude of S_{11} stays below $-25\,\mathrm{dB}$ under $12\,\mathrm{GHz}$, and below $-30\,\mathrm{dB}$ for most frequencies below $10\,\mathrm{GHz}$. The magnitude of S_{21} dips down at $16\,\mathrm{GHz}$, where the connector footprint radiates a significant fraction of the available incoming wave.

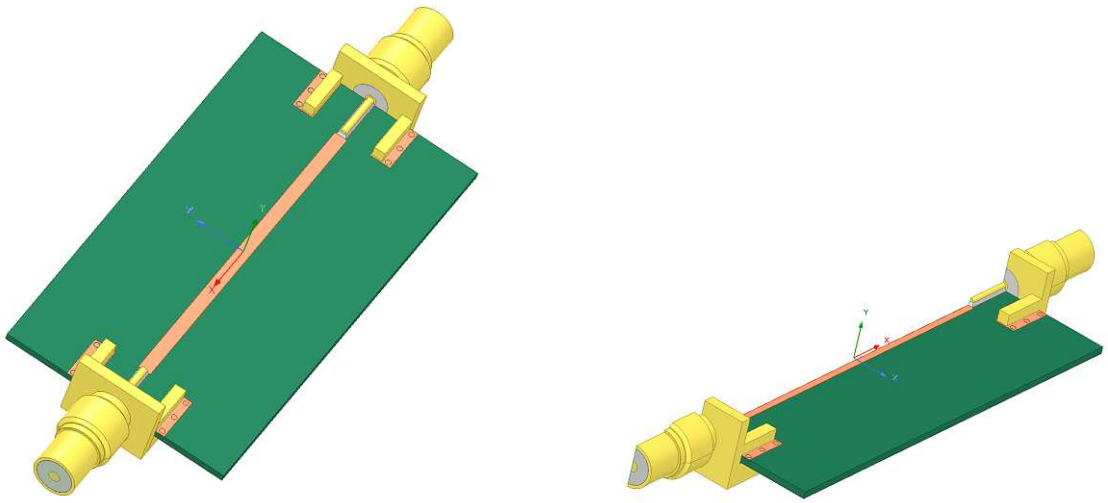

(a) **(b)**

Figure 4.1: Full PCB (a) and one half (b)

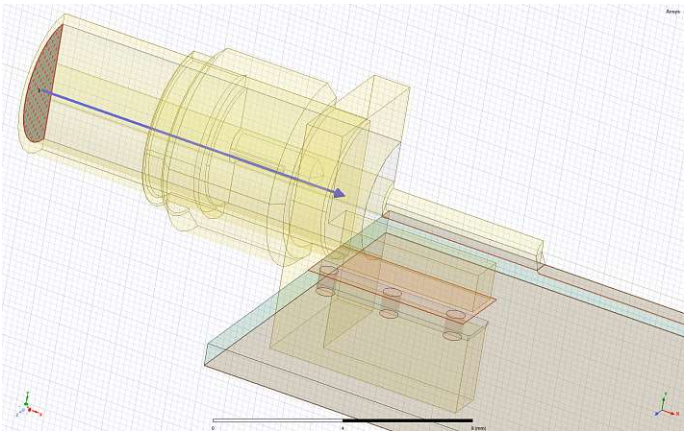

Figure 4.2: De-embedding the wave port up to the connector-microstrip-line interface.

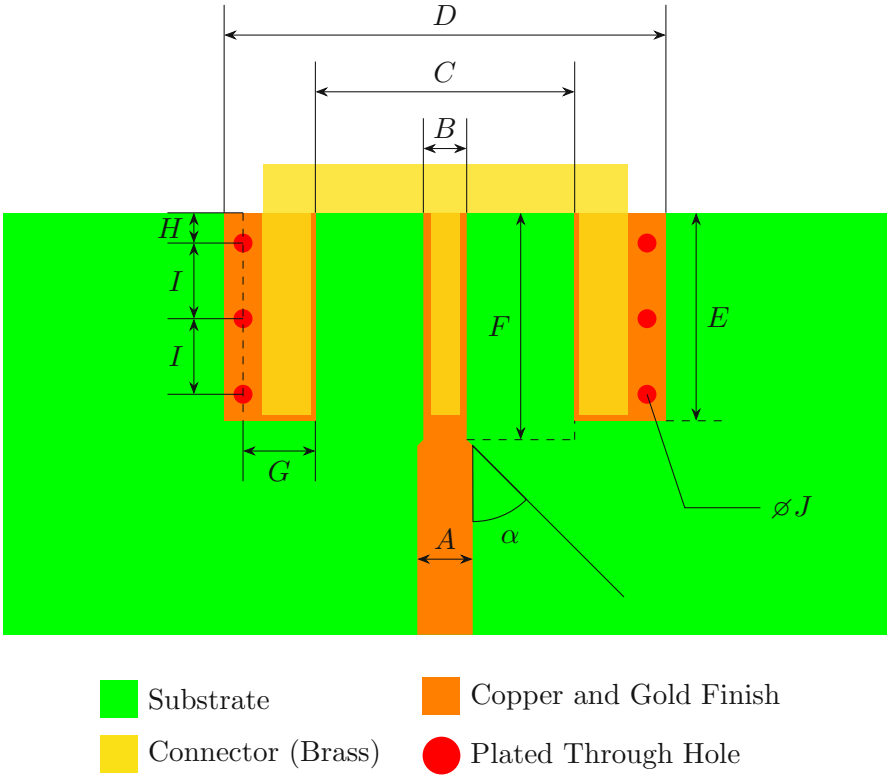

Figure 4.3: Top view of the optimized footprint for the coaxial launch connector.

Table 4.1: Dimensions for the footprint in Fig. 4.3.

Property	Dimension
A	1.466 mm
B	1.146 mm
C	6.858 mm
D	11.684 mm
E	5.500 mm
F	5.500 mm
G	1.913 mm
H	0.500 mm
I	2.250 mm
J	0.600 mm
α	45°

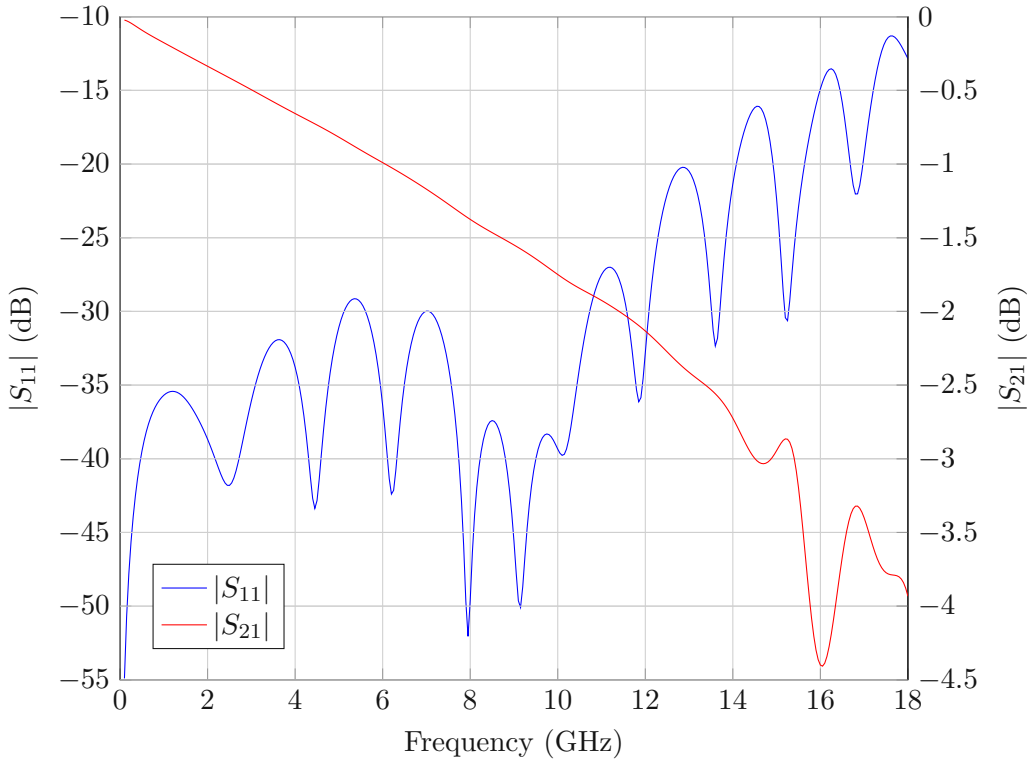

Figure 4.4: Results for $|S_{11}|$ and $|S_{21}|$ for a simulated PCB with two connectors with the optimized footprint.

4.2 TRL Calibration Kit

Similar as in Chapters 2 and 3, the reference planes for both ports must lie at the center of the CSRR. The short, open, load, thru (SOLT) calibration shifts the reference planes to the connectors at the end of the VNA's cables. A TRL calibration shifts the reference planes past the connectors and onto the PCB, by a distance called the de-embedding distance. A TRL calibration kit provides the VNA with the necessary tools for that. Fig. 4.5 shows an example of a TRL calibration kit with four elements in total.

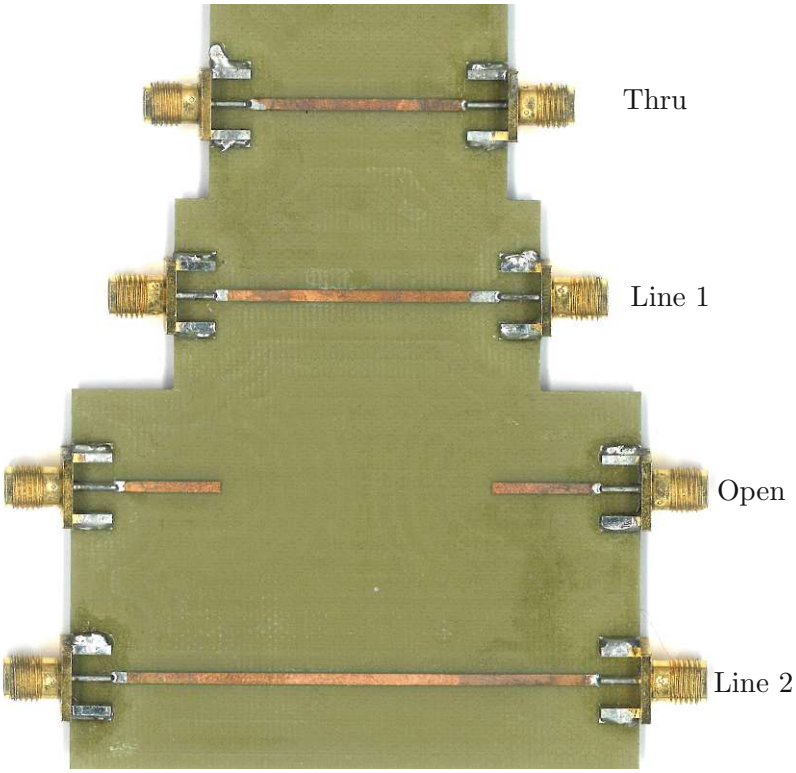

Figure 4.5: Example of a TRL calibration kit and labels for its elements.

1. A thru element. The thru line is a line whose length is equal to the sum of the distances between each PCB launch connector and its corresponding reference plane. In the case of this test fixture, the thru element consists of a line that is as long as the microstrip line above each CSRR.

2. One or more line elements. A line element is similar to a thru element but longer. The additional length is determined by the frequency range for which the calibration is performed. When only one line element is present, the recommended frequency range is such that the additional electrical length of the line is between 20 and 160 degrees. Adding multiple line elements in one TRL calibration kit allows for a frequency range that vastly exceeds the union of the frequency ranges that each line element would allow for individually [39]. For this test fixture, I aim to perform a calibration for the frequency range from 250 MHz to 8 GHz. The TRL calibration kit for the test fixture contains the line elements specified in Tab. 4.2.

3. A reflect element. A reflect element is a line whose length equals the distance between the launch-connector and the center of the CSRR. The reflect element is terminated with an open or a short. For the calibration kit in this test fixture, I use an open. If both reference planes are equally far apart from the launch connectors, only one reflect element is required. Two reflect elements are only necessary when the de-embedding distances for the two ports are not equal. Despite not being necessary, I place two reflect elements on the PCB. This allows attaching both connectors of the VNA to a reflect element simultaneously which saves time during the calibration procedure.

Line	ΔLength	20°-Frequency	160°-Frequency
Line 1	9.1 mm	1.00 GHz	8 GHz
Line 2	30.4 mm	0.30 GHz	2.4 GHz
Line 3	36.5 mm	0.25 GHz	2 GHz

Table 4.2: Additional lengths of the line elements for the TRL calibration kit. The 20°- and 160°-Frequencies are the frequencies at which the additional electrical length of the line is 20 and 160 degrees, respectively.

4.3 Size and Number of CSRRs

Measuring an MUT's complex permittivity over a range of frequencies requires multiple CSRRs with different resonant frequencies. Placing multiple CSRRs on one PCB can be done in one of two ways.

(i) All CSRRs are placed in series, coupled to the same microstrip line. The concatenation of multiple CSRRs yields several resonant frequencies, and all of them shift when being loaded. The permittivity is estimated by observing the shift in each resonant frequency. Such an approach is not applicable to the equivalent circuit model in this thesis, as the valid frequency range for each CSRR's equivalent circuit is different. Furthermore, concatenating CSRRs with different resonant frequencies poses another problem when their fundamental resonant frequency is sufficiently far apart: One CSRR's fundamental resonant frequency might overlap with the higher order resonant frequency of another CSRR, making any visual distinction between the two impossible.

(ii) Each CSRR is placed on a different microstrip line. Placing all CSRRs on separate microstrip lines allows to apply the equivalent circuit model from Chapter 2.

In this thesis, I aim to measure SUTs's complex permittivity in the frequency range from 1 GHz to 2.5 GHz, for materials with $\varepsilon_r' \leq 10$. The sizes of the CSRRs are therefore chosen such that some of their fundametnal resonant frequencies lie in the range from 1 GHz to 2.5 GHz when loaded with an SUT whose $\varepsilon_r' \leq 10$. I define the saturated resonant frequency $f_{\text{res,sat}}$ as the resonant frequency of a CSRR loaded with a sufficiently thick SUT whose real permittivity is the maximum specified permittivity for the test fixture. A sample is considered sufficiently thick if an increase in its thickness does not further shift the resonant frequency of the CSRR it is loading. In Chapter 3, loading a CSRR with a 10 mm thick sample with $\varepsilon_r' = 10$ reduced the resonant frequency by 35%. Given that the

resonant frequency does not shift further after increasing h_{SUT}, and that $\varepsilon_r' = 10$ is the greatest permittivity I aim to measure in this thesis, I define $f_{\mathrm{res,sat}}$ as

$$f_{\mathrm{res,sat}} = f_{\mathrm{res},0} \cdot 0.65, \tag{4.1}$$

where $f_{\mathrm{res},0}$ is the resonant frequency of the unloaded CSRR.

The test fixture contains five CSRRs, each with its own microstrip line. Fig. 4.6 shows f_{res} over d, where the remaining dimensions are fixed to the values in Tab. 2.1. Using least squares, the relation between $f_{\mathrm{res},0}$ and d is approximated as

$$f_{\mathrm{res},0} = \frac{12.42\,\mathrm{GHz}}{\frac{d}{1\,\mathrm{mm}} - 1.554}. \tag{4.2}$$

I place five CSRRs on the PCB whose $f_{\mathrm{res},0}$ are logarithmically spaced from 1 GHz to 4 GHz. Tab. 4.3 contains the values for d for each CSRR. The choice for the values of d allows for characterizing MUTs with $\varepsilon_r' \leq 10$ around multiple frequencies between 1 GHz and 2.5 GHz.

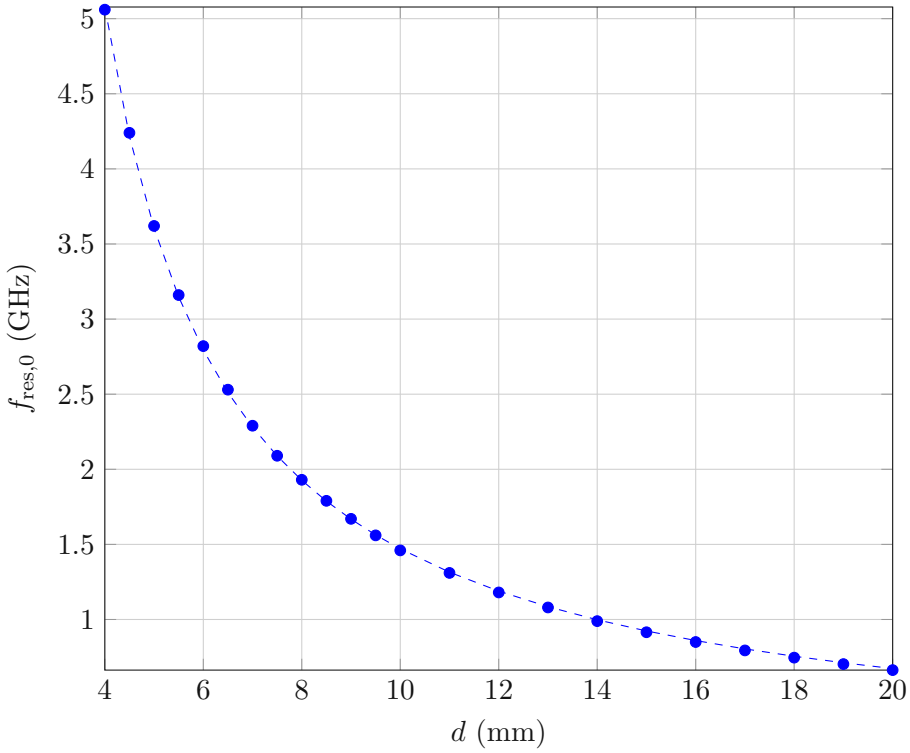

Figure 4.6: Resonant frequency of an unloaded CSRR $f_{\mathrm{res},0}$ as function of the side length d. Dots represent exact values. The dashed curve is the approximation (4.2).

Table 4.3: Values for d for the CSRRs in the test fixture.

d	13.9 mm	10.3 mm	7.7 mm	6.0 mm	4.7 mm
$f_{\mathrm{res},0}$	1 GHz	1.41 GHz	2 GHz	2.83 GHz	4 GHz
$f_{\mathrm{res,sat}}$	0.65 GHz	0.92 GHz	1.3 GHz	1.84 GHz	2.6 GHz

4.4 Board Layout

The two remaining aspects to be clarified are the distance between nearby CSRRs and the maximum size of a sample that shall fit onto the test fixture.

An SUT must be large enough to cover the CSRR, putting a lower limit on the SUT's size. An upper limit to the SUT's size is given with the line (and, correspondingly, the distance between two launch connectors on opposing edges of the PCB) and the length that the launch connector occupies on both layers of the PCB. I choose a microstrip line length of 180 mm, to ensure that samples with a shorter side length of up to 169 mm can still be mounted over all CSRRs.

With all CSRRs placed on the same ground plane, it is possible that surface currents make their way from one CSRR to another, causing a coupling effect between nearby CSRRs. Such a coupling is not accounted for in the models devised in Chapters 2 and 3 and must therefore be mitigated. The coupling is reduced by placing the CSRRs apart by 50 mm.

Fig. 4.7 shows photos of the top and bottom layer of the test fixture. The CSRRs are designed according to the definitions in Fig. 2.1 and the values from Tab. 2.1, where the values for d are listed in Tab. 4.3. The test fixture contains the five TRL calibration kit elements and the five CSRRs, as indicated in the silk-screen close to each connector.

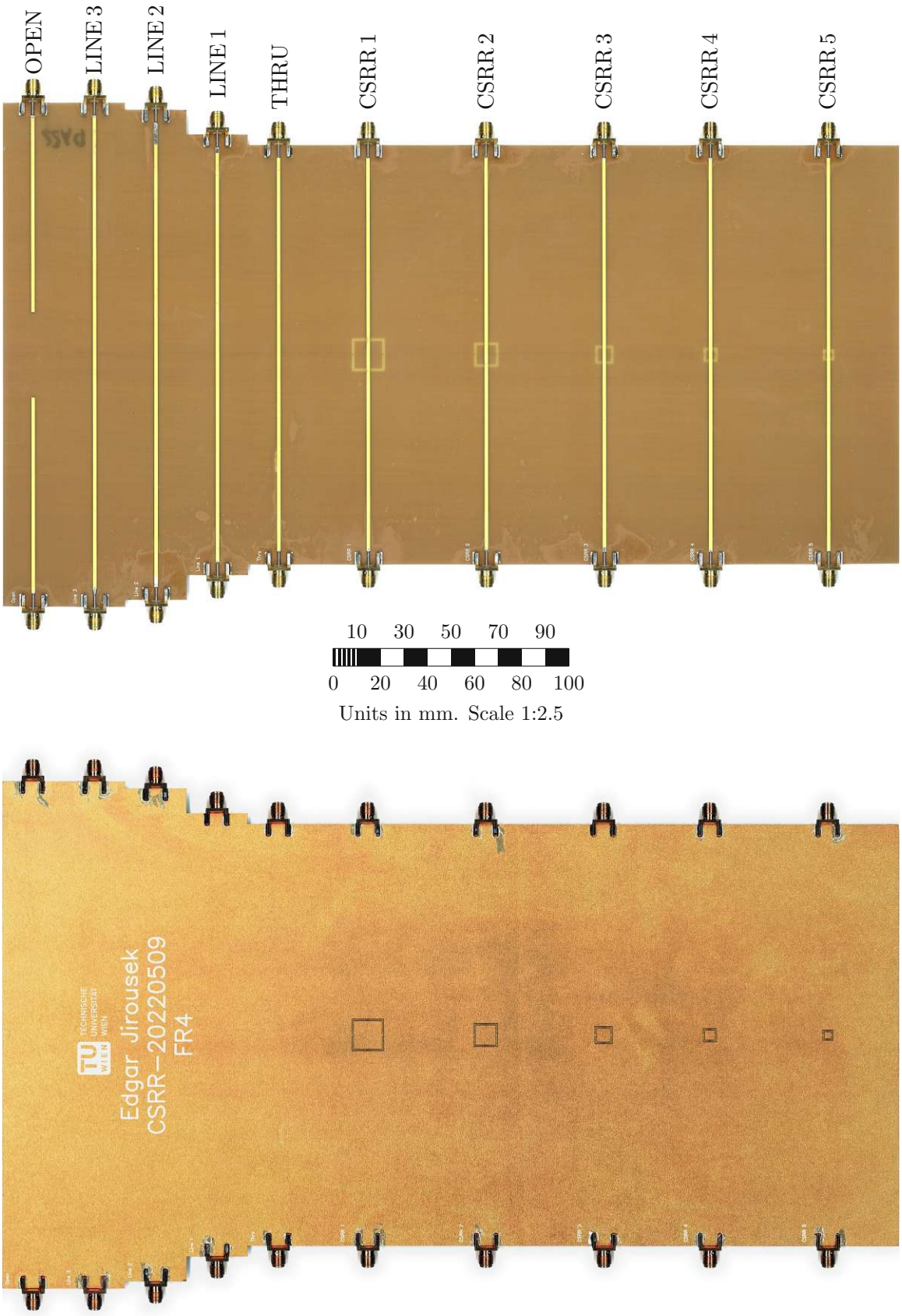

Figure 4.7: Top layer (top) and bottom layer (bottom) of the CSRR test fixture.

5 Measurement-Based Permittivity Determination

Chapter 3 contains a description of how to calculate a material's complex permittivity from the equivalent circuit parameters using simulation results. Figs. 3.12 and 3.14 in Chapter 3 visualized the direct proportional relations between S and the SUT's susceptibility, and between $\tilde{Q}^{-1}$ and the SUT's loss tangent. In this chapter, I produce similar plots and verify the aforementioned relations using the test fixture from Chapter 4 and a variety of material samples. Only material samples whose complex permittivity is known are used during the measurements, in order to easily verify the measurement results.

The rest of this chapter is structured as follows. Section 5.1 gives an overview of the materials used to carry out the measurements. The measurement setup is described in Section 5.2. Section 5.3 describes the calibration. In Section 5.4, I describe the measurement procedure. The measurement results are presented and discussed in Section 5.5.

5.1 Material Samples

Verifying the measurement results for a given MUT's ε_r' and $\tan\delta$ requires knowledge of these properties obtained by a proven test method. That knowledge can be obtained in two ways. One can measure ε_r' and $\tan\delta$ for all materials with another measurement method. That is beyond the scope of this thesis. The other way is to reduce the choice of MUTs to materials whose complex permittivity was measured before and is provided. One group of such materials are RF substrates. Manufacturers provide information about substrates' complex permittivity, applicable frequency, and measurement methods used to obtain that information in data sheets.

Tab. 5.1 and Fig. 5.1 contain details about the materials used as samples in this chapter. The materials are RF substrates and are typically copper-clad. To measure their permittivity, the copper is removed by a chemical etching process. The samples' thicknesses range from 0.508 mm to 3.175 mm, depending on the material. The samples' width and height are both in the range from 4 mm to 5.5 mm. In Chapter 3, the sample thickness h_{SUT} must reach around 10 mm so that the parameter C_{Res}, linked to ε_r', does not increase with an increase in the sample's thickness. Reaching a thickness on that order offers the advantage that the exact value of h_{SUT} does not need to be known in order to calculate ε_r'.

Table 5.1: Used materials with known relative complex permittivity, and the frequency at which it was measured. Blank spaces indicate missing data in datasheets.

Material		ε_r'	$\tan\delta$	Frequency	Manufacturer
Polyguide PG-A	[40]	2.32 ± 0.005	$0.5 \cdot 10^{-3}$	10 GHz	Crane Polyflon
GML 1000	[41]	3.05 ± 0.05 3.05 ± 0.05	$3.0 \cdot 10^{-3}$ $5.0 \cdot 10^{-3}$	2.5 GHz 10 GHz	GIL
AD255A	[42]	2.55 2.55	$1.5 \cdot 10^{-3}$ $1.3 \cdot 10^{-3}$	10 GHz 1 MHz	Arlon
RF-35	[43]	3.5	$1.8 \cdot 10^{-3}$	1.9 GHz	Taconic
CER-10	[44]	9.5 ± 0.5	$3.5 \cdot 10^{-3}$	10 GHz	Taconic
TMM 10i	[45]	9.20 ± 0.23 9.8	$2.2 \cdot 10^{-3}$	10 GHz 8 GHz–40 GHz	Rogers
RO3006	[46]	6.15 ± 0.15 6.5	$2.0 \cdot 10^{-3}$	10 GHz 8 GHz–40 GHz	Rogers
RO4360	[47]	6.15 ± 0.15 6.15 ± 0.15	$3.8 \cdot 10^{-3}$	10 GHz 2.5 GHz	Rogers

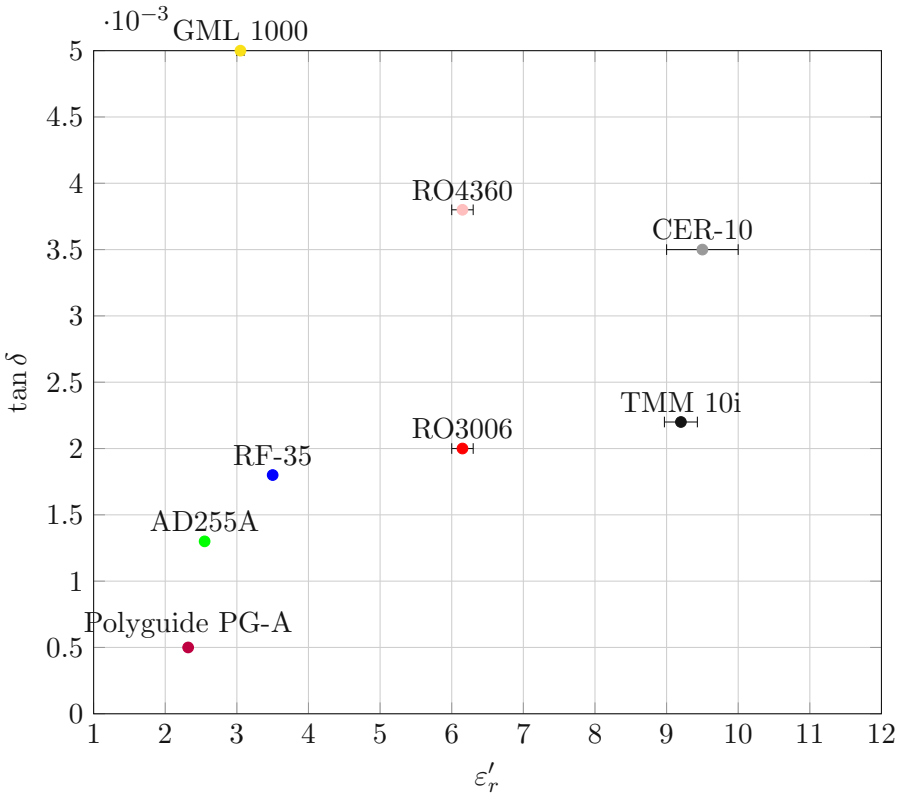

Figure 5.1: Map of used materials listed in Tab. 5.1.

To reach a thickness on the order of 10 mm, I stack several samples of the same material on top of each other. Tab. 5.2 contains details about the thickness of each individual sample and the maximum thickness that can be obtained when all available samples are stacked on top of each other.

Table 5.2: Number of samples, their individual thickness, and the maximum thickness of all samples stacked on top of each other.

Material	Number of Samples	Sample Thickness		Maximum Thickness	
		in mil	in mm	in mil	in mm
Polyguide PG-A	9	125	3.175	1125	28.575
GML 1000	4	20	0.508	80	2.032
AD255A	14	30	0.762	420	10.668
RF-35	12	60	1.524	720	18.288
CER-10	20	25	0.635	500	12.700
TMM 10i	9	50	1.270	450	11.430
RO3006	16	25	0.635	400	10.160
RO4360	21	20	0.508	420	10.668

5.2 Measurement Setup

Fig. 5.2 shows a photo of the measurement setup. A Keysight PNA-X is the VNA that measures the S-parameters. The test fixture is placed on a piece of Rohacell [48] with its bottom layer facing upwards. That way, the CSRRs are loaded by placing SUTs directly on top. The VNA's coaxial connectors are mounted on the end launch connectors of the test fixture. The coaxial cables rest on blocks of Rohacell to prevent the test fixture from bending under the weight of the VNA's connectors. Each of the VNA's connectors rest on a piece of Rohacell so that they are at the same height as the test fixture's connectors. Otherwise, the test fixture would bend under the VNA's connectors' weight, which could in turn distort the measurement results.

5.3 Calibration

The calibration serves to shift the reference planes to the desired location on the test fixture. In accordance with the equivalent circuit model from Chapter 2, the reference planes are shifted to the center of the CSRR. This reference plane shift is achieved by two consecutive calibrations. First, I perform an SOLT calibration to define the reference planes at the ends of the VNA's coaxial cables. From there, the reference planes are shifted to the center of the microstrip line, which coincides with the center of the CSRR with a TRL calibration.

An electronic calibration (E-cal) kit by Keysight Technologies is used for an SOLT calibration. The frequency settings are listed in Tab. 5.3.

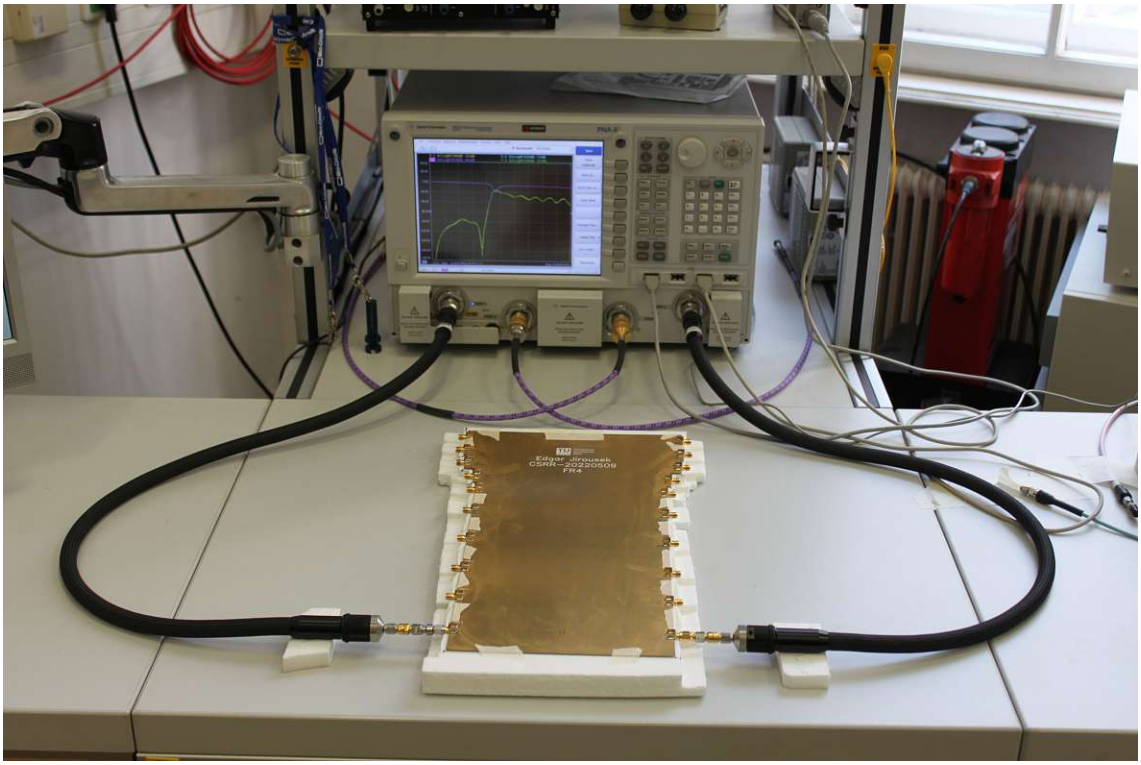

Figure 5.2: Photo of the measurement setup.

Table 5.3: SOLT calibration settings.

Minimum Frequency	Maximum Frequency	Frequency Step	IF Bandwidth
10 MHz	9 GHz	1 MHz	10 kHz

The algorithm proposed in [39] enables a TRL calibration from 10 MHz to 9 GHz with the five elements (thru, open, lines 1-3) on the test fixture. A MATLAB implementation of the algorithm, *MultilineTRL*, is used to perform the calibration. It is available on GitHub [49]. A screenshot of *MultilineTRL*'s graphical user interface (GUI) is shown in Fig. 5.3. *MultilineTRL* requires the following information for a calibration:

- The S-parameters for the thru, short, and line elements.
- The desired frequency range for the calibration
- An estimation for the microstrip lines' propagation constant for each frequency

The S-parameters for the thru, short, and line elements are measured with the VNA. The results are stored in Touchstone s2p files.

The propagation constant for the desired frequency points is exported from a simulation in HFSS, where a microstrip line with the same dimensions and substrate is simulated. The magnitude and phase of the propagation constant are exported for frequencies from 10 MHz to 9 GHz in steps of 1 MHz and stored in a table.

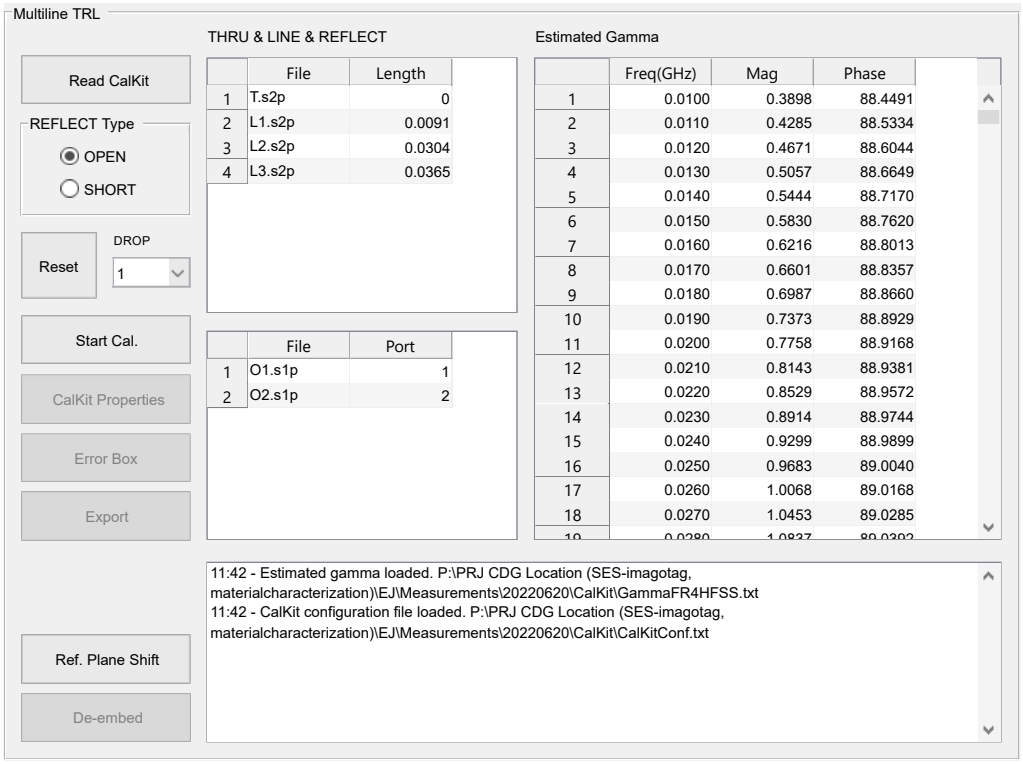

Figure 5.3: *MultilineTRL* GUI window.

5.4 Measurement Procedure

The following procedure is carried out for all five CSRRs and all materials from Tab. 5.1 independently. One sample is placed on the test fixture, so that it backs one of the five CSRRs, as shown in Fig. 5.4. When placing a sample on the test fixture, there is an air gap between the sample and the test fixture. Such an air gap varies in size from one sample to another and alters the measurement results. Not mitigating the air gap, therefore, causes inconsistent changes in the measurement results. To minimize the air gap, the sample is pressed against the test fixture with a block of Rohacell, as in Fig. 5.5. Rohacell is a suitable material for pressing against the sample, as its permittivity is comparable to air. Hence, the CSRR is only loaded by the sample, and the effects of the Rohacell block in the CSRR's vicinity can be neglected. The S-parameters of the CSRR loaded with the SUT are measured. The same measurement is repeated after stacking multiple samples of the same material on top of each other.

The measurement procedure yields the S-parameters from 10 MHz to 9 GHz for all sample heights and CSRRs. The S-parameters serve to calculate the equivalent circuit parameters as in Chapter 3. The results and the derivation of the materials' ε_r are discussed in

Section 5.5.

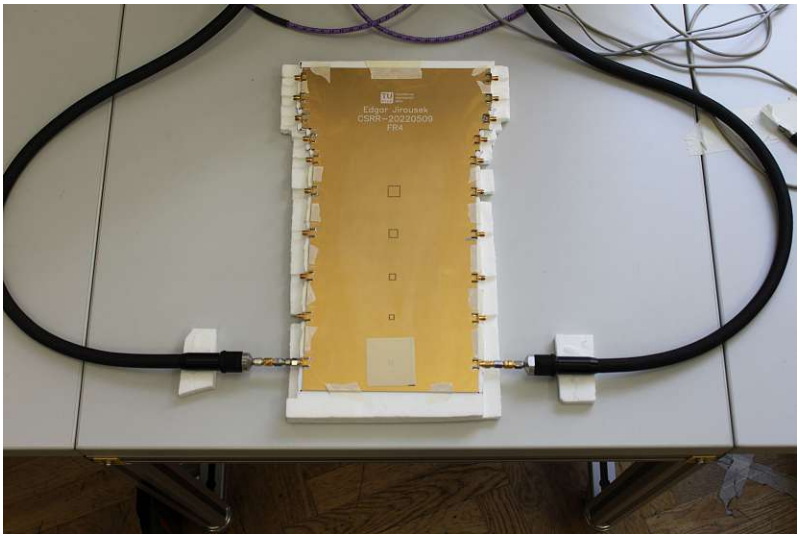

Figure 5.4: A sample loading CSRR 5 on the test fixture.

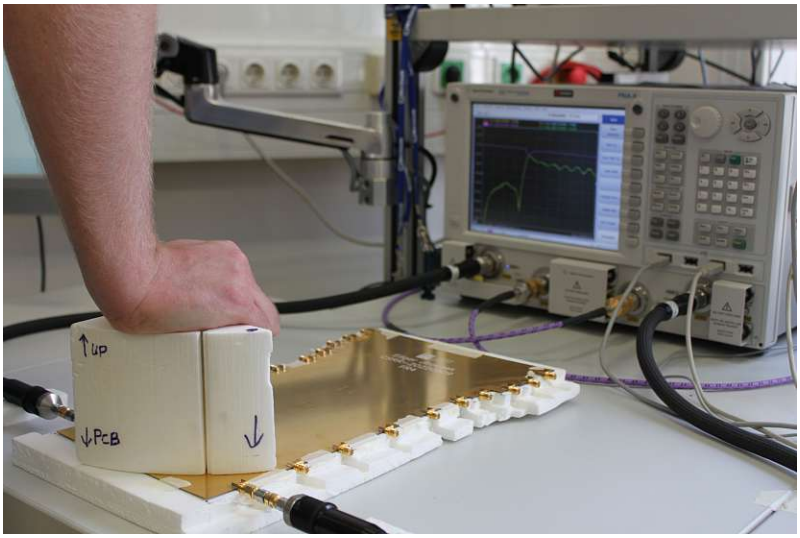

Figure 5.5: A sample is pressed against a CSRR with a block of Rohacell during measurement.

5.5 Results and Discussion

The measured S-parameters of the unloaded CSRRs are used to obtain the values for the equivalent circuit as discussed in Chapter 2. The measured S-parameters of the loaded CSRRs are used to obtain the values for the equivalent circuit elements C_{Res} and G_{Res} as discussed in Chapter 3. The MUTs' permittivity and loss tangent are estimated based on the changes in C_{Res} and G_{Res} as in Chapter 3. In order to compare the measurement results for ε_r' and $\tan\delta$ to those in the data sheets, I assume that the MUTs' permittivities are constant and correspond to the values in Tab. 5.1. A better method to verify the

measurement results would be to measure the MUTs' ε_r' and $\tan\delta$ with a proven test method from Section 1.1, and to compare the results to the ones obtained by using CSRRs.

It is shown that a material's permittivity's real part can be measured accurately with the test fixture. The loss tangents of the materials from Tab. 5.1 range from $5\cdot10^{-4}$ to $5\cdot10^{-3}$, which is on the order of the measurement uncertainty for $\tan\delta$ with an FR-4 based test fixture. Therefore, exact values for the materials' loss tangents cannot be measured, but it can be shown that they are on the order of 10^{-3}. Furthermore, exact values for the loss tangent are not provided for the CSRRs' resonant frequencies, making a comparison to precise values impossible.

5.5.1 Real Permittivity

Fig. 5.6 shows the results for S, as defined in (3.3), over the thickness of the stack of material samples h_{SUT}. For all five CSRRs, the values for S, and consequently for C_{SUT} converge around 12 mm. S does not increase monotonically with h_{SUT} for all materials. Occasional downticks are noticeable in CER-10 and RF-35. The clamping pressure between the stack of SUTs and the PCB is applied manually, and can therefore vary from one measurement to another, resulting in variations in the compressed SUT's thickness, and possible air gaps between SUTs.

The observed convergence of S with respect to increasing h_{SUT} is in line with the simulation results from Chapter 3, where S also converges for MUTs with a loss tangent of 0.001 or 0.005. Measuring with five different CSRRs reveals a relation unseen in the simulations, where only one CSRRs was considered: The parameter S converges faster for CSRRs with higher resonant frequency.

Comparing the results from Fig. 5.6 to the material properties in Tab. 5.1 further reveals that the S-curves for materials with similar values for ε_r' are close, if not even overlapping. In particular, the S-curves for RO3006 and RO4360 — both with $\varepsilon_r' = 6.15$ according to the datasheet — overlap in all five CSRRs. More insight is given by dividing S by the susceptibility of each material. I define the nominal susceptibility χ_{nom} as

$$\chi_{\mathrm{nom}} = \varepsilon_r' - 1, \tag{5.1}$$

where ε_r' is the corresponding value from Tab. 5.1. For TMM 10i and RO3006 I choose ε_r' for 10 GHz. Fig. 5.7 shows the results for S/χ_{nom} over h_{SUT}. The curves are almost overlapping, thus strengthening the established linear relation

$$S \approx a\,(h_{\mathrm{SUT}}) \cdot \chi_{\mathrm{nom}}. \tag{5.2}$$

Like in Chapter 3, values for $a\,(h_{\mathrm{SUT}})$ and the measurement uncertainty shall be established for $h_{\mathrm{SUT}} = 10\,\mathrm{mm}$. No stack of samples reaches a thickness of exactly 10 mm. In order to obtain values for S for $h_{\mathrm{SUT}} = 10\,\mathrm{mm}$, I linearly interpolate S for the two values for h_{SUT} closest to 10 mm. Tab. 5.4 contains the range of values for S/χ_{nom} at $h_{\mathrm{SUT}} = 10\,\mathrm{mm}$. The smallest occuring value for S/χ_{nom} is denoted min S/χ_{nom}, and the largest max S/χ_{nom}. Their reciprocals are denoted max χ_{nom}/S and min χ_{nom}/S.

Using the values max χ_{nom}/S and min χ_{nom}/S, I derive the relation between S and χ_{nom} as

$$\chi_{\mathrm{nom}} = a\,(10\,\mathrm{mm}) \cdot S \cdot (1 \pm e_\chi)\,, \tag{5.3}$$

where e_χ is the relative error for χ_{nom}. The values for a and e_χ are listed in Tab. 5.5.

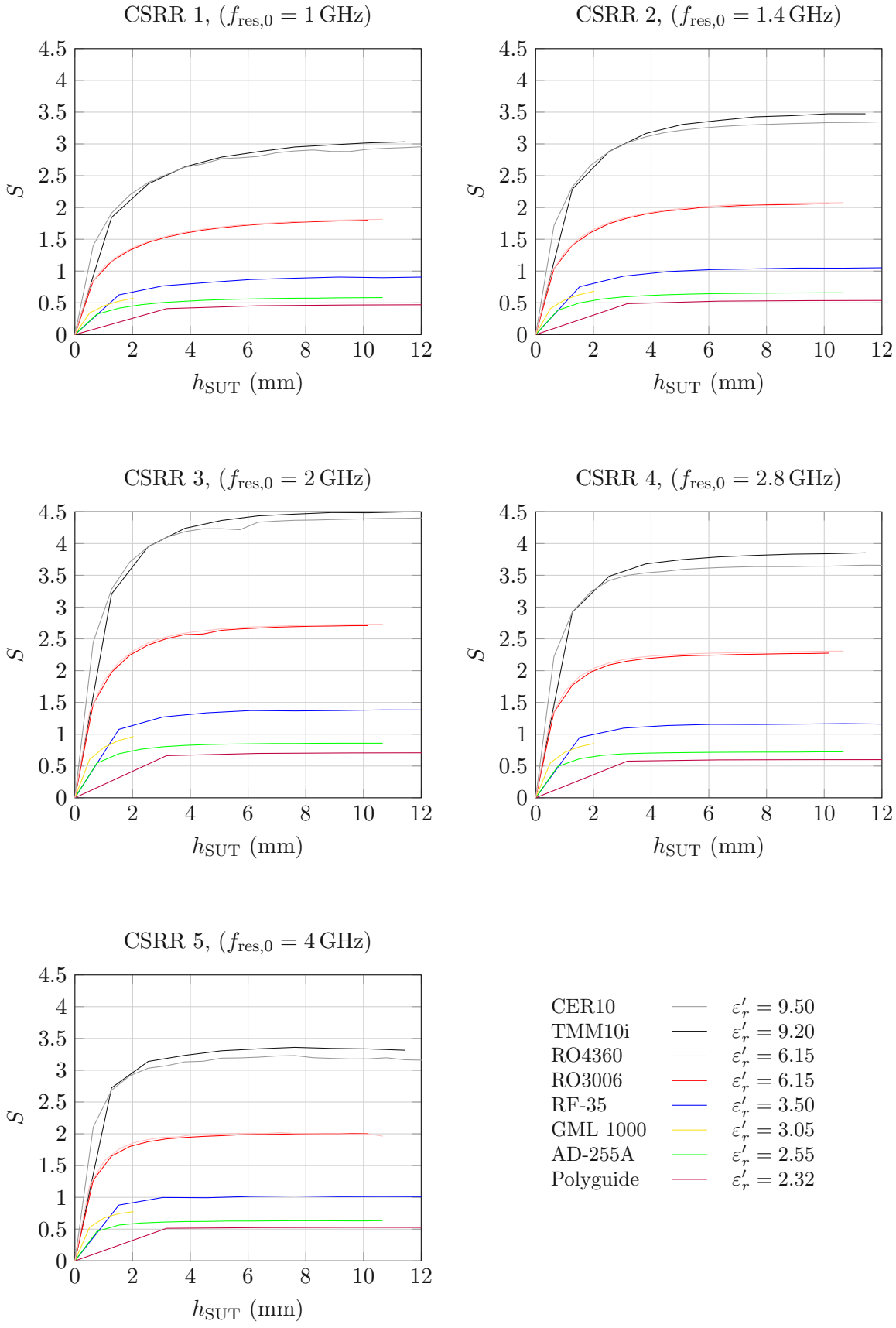

Figure 5.6: Values for S after optimization using measurement data.

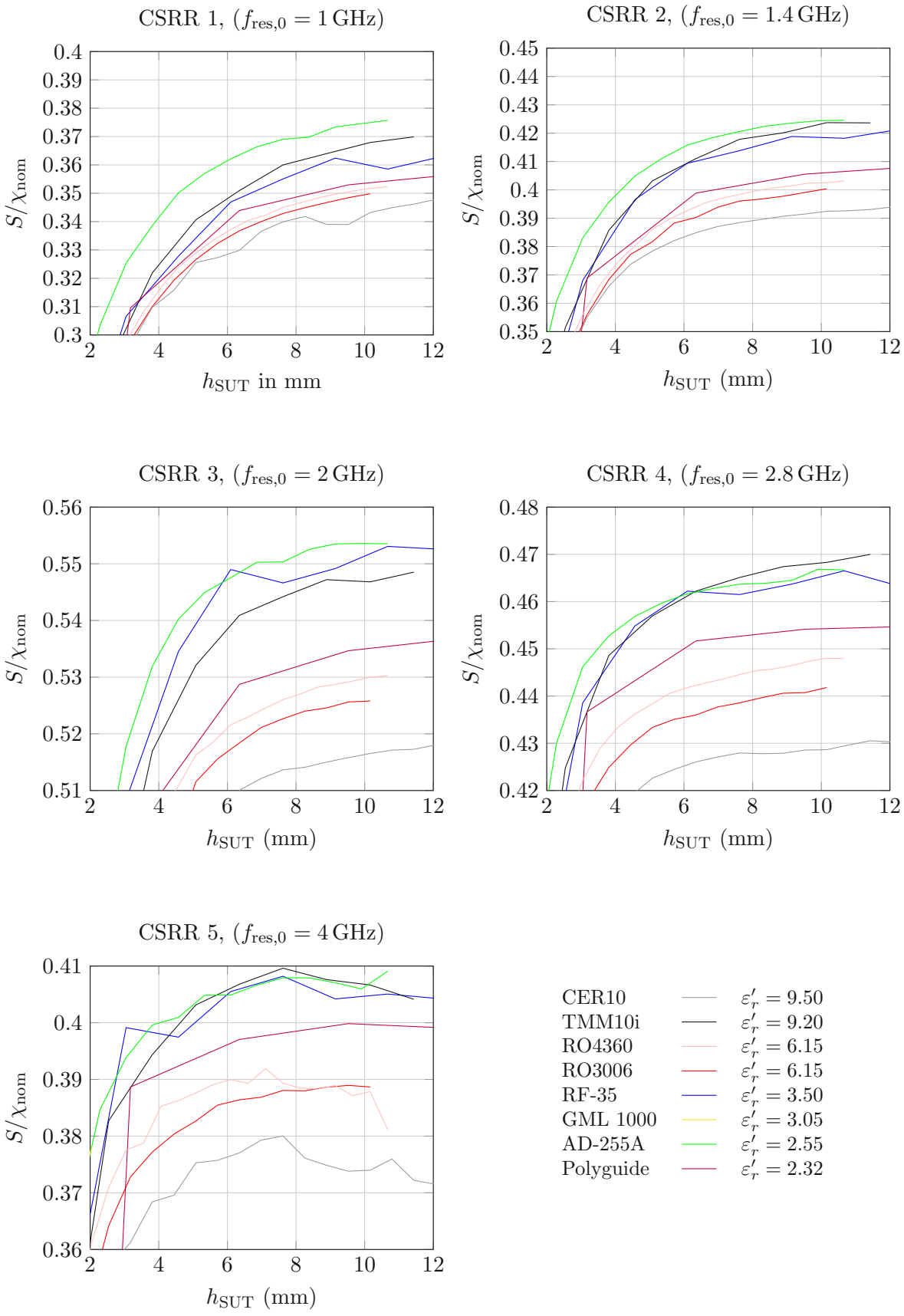

Figure 5.7: Values for S/χ_{nom} after optimization using measurement data.

Table 5.4: Range for S/χ_{nom} for each of the five CSRRs.

$f_{\text{res},0}$	1 GHz	1.4 GHz	2 GHz	2.8 GHz	4 GHz
min S/χ_{nom}	0.3424	0.3923	0.5164	0.4287	0.3777
max S/χ_{nom}	0.3747	0.4245	0.5536	0.4682	0.4082
min χ_{nom}/S	2.921	2.549	1.936	2.333	2.648
max χ_{nom}/S	2.669	2.356	1.806	2.136	2.450

The values a for e_χ are derived under the assumption that the values for ε'_r in the data sheet are exact for the resonant frequencies for all CSRRs. In order to measure an SUT's permittivity, it is necessary to determine $a\,(h_{\text{SUT}})$ by using a sample whose permittivity is known beforehand. Once $a\,(h_{\text{SUT}})$ has been determined, the permittivity of an SUT with a thickness of h_{SUT} can be determined as

$$\varepsilon'_{r,\text{SUT}} = a\,(h_{\text{SUT}}) \cdot S + 1, \tag{5.4}$$

where $\varepsilon'_{r,\text{SUT}}$ is the real part of the SUT's relative complex permittivity. Using one of the materials from Tab. 5.1 as a reference material to determine $a\,(h_{\text{SUT}})$ would yield an error of up to $2 \cdot e_\chi$, when using the obtained value for $a\,(h_{\text{SUT}})$ in order to measure $\varepsilon'_{r,\text{SUT}}$ of the other materials from Tab. 5.1. A step-by-step guide on how to measure a sample's permittivity using a reference material is provided in Appendix A.

The major limiting factor to measuring a material's permittivity is the lack of a reference measurement at the desired frequencies for one SUT that serves as a reference material. A reference measurement can be carried out using one of the methods discussed in Section 1.1 and yields exact results for the SUT's complex permittivity.

Table 5.5: Values for $a\,(10\,\text{mm})$ and limits for e_χ for each of the five CSRRs.

$f_{\text{res},0}$	1 GHz	1.4 GHz	2 GHz	2.8 GHz	4 GHz
$a\,(10\,\text{mm})$	2.795	2.452	1.871	2.234	2.549
e_χ	$\leq 4.5\%$	$\leq 3.9\%$	$\leq 3.5\%$	$\leq 4.4\%$	$\leq 3.9\%$

5.5.2 Loss Tangent

Fig. 5.8 shows the results for $\tilde{Q}^{-1}$, defined as

$$\tilde{Q}^{-1} = \sqrt{\frac{L_{\text{Res}}}{C_{\text{Res,SUT}} - C_{\text{Res},0}}} \cdot (G_{\text{Res,SUT}} - G_{\text{Res},0}) \tag{5.5}$$

over h_{SUT}. The sample materials' loss tangents range from $0.5 \cdot 10^{-3}$ to $5.0 \cdot 10^{-3}$, values comparable to the absolute measurement uncertainty for a CSRR with an FR-4 substrate in Chapter 3. The exact values for the MUT's loss tangents can therefore not be devised. Nevertheless, the measurement results for $\tilde{Q}^{-1}$ and the data sheet results for $\tan\delta$ are still compared, in order to find consistencies and inconsistencies, given that $\tilde{Q}^{-1}$ and $\tan\delta$ follow an almost linear relation. To allow for a fair comparison between the losses in GML 1000 and other substrates, I consider GML 1000's specified loss tangent only at 10 GHz. GML 1000's loss tangent is specified for both 10 GHz and 2.5 GHz, while the

loss tangents of all other substrates apart from RF-35 are specified for 10 GHz only. The following consistencies between measured values of $\tilde{Q}^{-1}$ and data sheet values of $\tan\delta$ can be observed:

- RO3006 and RO3460 have the same permittivity. RO3460 has a greater loss tangent than RO3006. It is therefore expected that $\tilde{Q}^{-1}$ for RO3460 is always greater than for RO3006. This is indeed the case for all five CSRRs.
- The same is the case for CER-10 and TMM 10i. While their real permittivities are similar (9.5 and 9.2, respectively), CER-10 has a higher loss tangent and therefore yields greater values of $\tilde{Q}^{-1}$ in all five CSRRs.
- Polyguide and AD255A have similar permittivities (2.32 and 2.55, respectively), but Polyguide's loss tangent is one third of that of AD255A, the lowest of all materials. As expected, Polyguide has the lowest $\tilde{Q}^{-1}$ of all materials, even reaching negative values, with AD255A obtaining the second-lowest in all five CSRRs.

There are, however, also inconsistencies between the measurement results for $\tilde{Q}^{-1}$ and the data sheet results for $\tan\delta$:

- The $\tilde{Q}^{-1}$-curves for RF-35 lie between those of AD-255A and RO3006 for CSRRs 1 and 2, but rise to the levels of those of CER 10 and RO4360 — whose loss tangents are twice that of RF-35 — for CSRRs 3,4, and 5. However, RF-35's data sheet specifies $\tan\delta$ for 1.9 GHz, while the other materials (with the exception of GML 1000) specify $\tan\delta$ only for 10 GHz.
- GML 1000 yields greater values for $\tilde{Q}^{-1}$ than any other substrate in CSRRs 1, 3, 4, and 5 (as expected), but not in CSRR 2, where they are second to only those of CER-10, whose ε'_r is 3 times that of GML 1000. At 10 GHz, GML 1000 has the greatest loss tangent from all the materials in Tab. 5.1. Hence, the fact that curves of $\tilde{Q}^{-1}$ are below those of CER-10 in CSRR 2 defies the expected result.

A direct comparison between the simulation and measurement results is not possible for the following reasons:

- The exact values for $\tan\delta$ of the substrates at the resonant frequencies of the five CSRRs on the test fixture are not contained in the data sheets. In fact, the data sheet for RF-35 only contains $\tan\delta$ for 1.9 GHz, while the data sheets for all other materials except GML 1000 only contain $\tan\delta$ for 10 GHz, making a direct comparison impossible.
- A reference measurement system to measure $\tan\delta$ of the samples at the resonant frequencies of the five CSRRs was not available.
- The simulations of loaded CSRRs were not carried out with the geometries of the five CSRRs on the test fixture, but with a resonant frequency of 2.3 GHz, due to time constraints.

Increasing h_{SUT} past a certain thickness on CSRR 4 and CSRR 5 drastically raises $\tilde{Q}^{-1}$. For CSRR 5, that threshold lies at around 4 mm, which is substantially higher than a typical sample thickness, and S almost converges. The rise in $\tilde{Q}^{-1}$ coincides with a drop in the resonator's Q-factor Q_{Res}, defined as

$$Q_{\mathrm{Res}} = \sqrt{\frac{C_{\mathrm{Res,SUT}}}{L_{\mathrm{Res}}}} \cdot \frac{1}{G_{\mathrm{Res,SUT}}} \tag{5.6}$$

and shown in Fig. 5.9.

There are two factors that limit the ability to measure the loss tangent of the low loss materials from Tab. 5.1 in this thesis. One is the loss tangent of the test fixture's FR-4 substrate, which is greater than that of the SUTs. Another issue is that the measurement results obtained from the CSRRs cannot be verified. This is due to the lack of reference measurements for the SUTs's loss tangent at the desired frequencies.

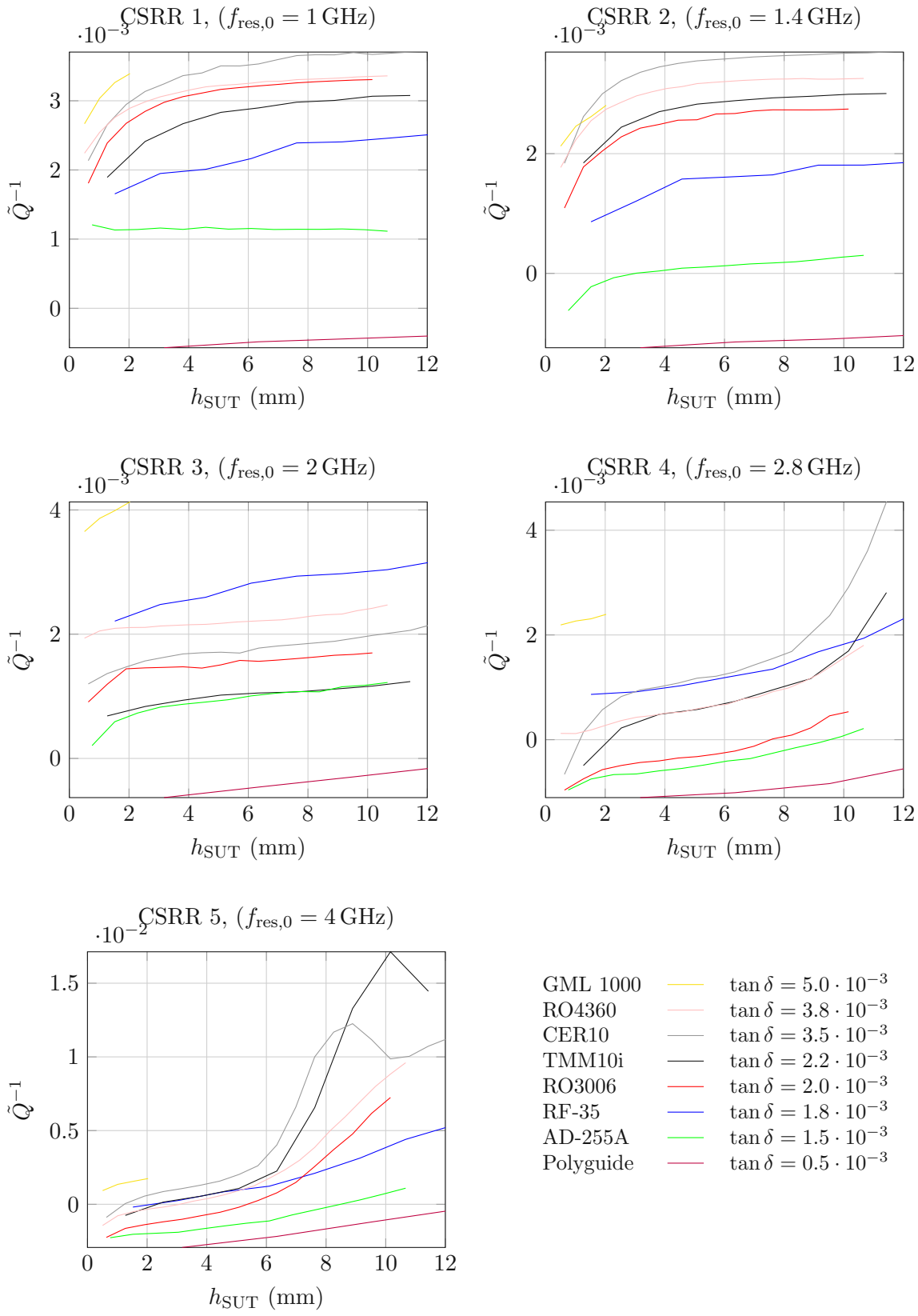

Figure 5.8: Values for $\tilde{Q}^{-1}$ after optimization using measurement data.

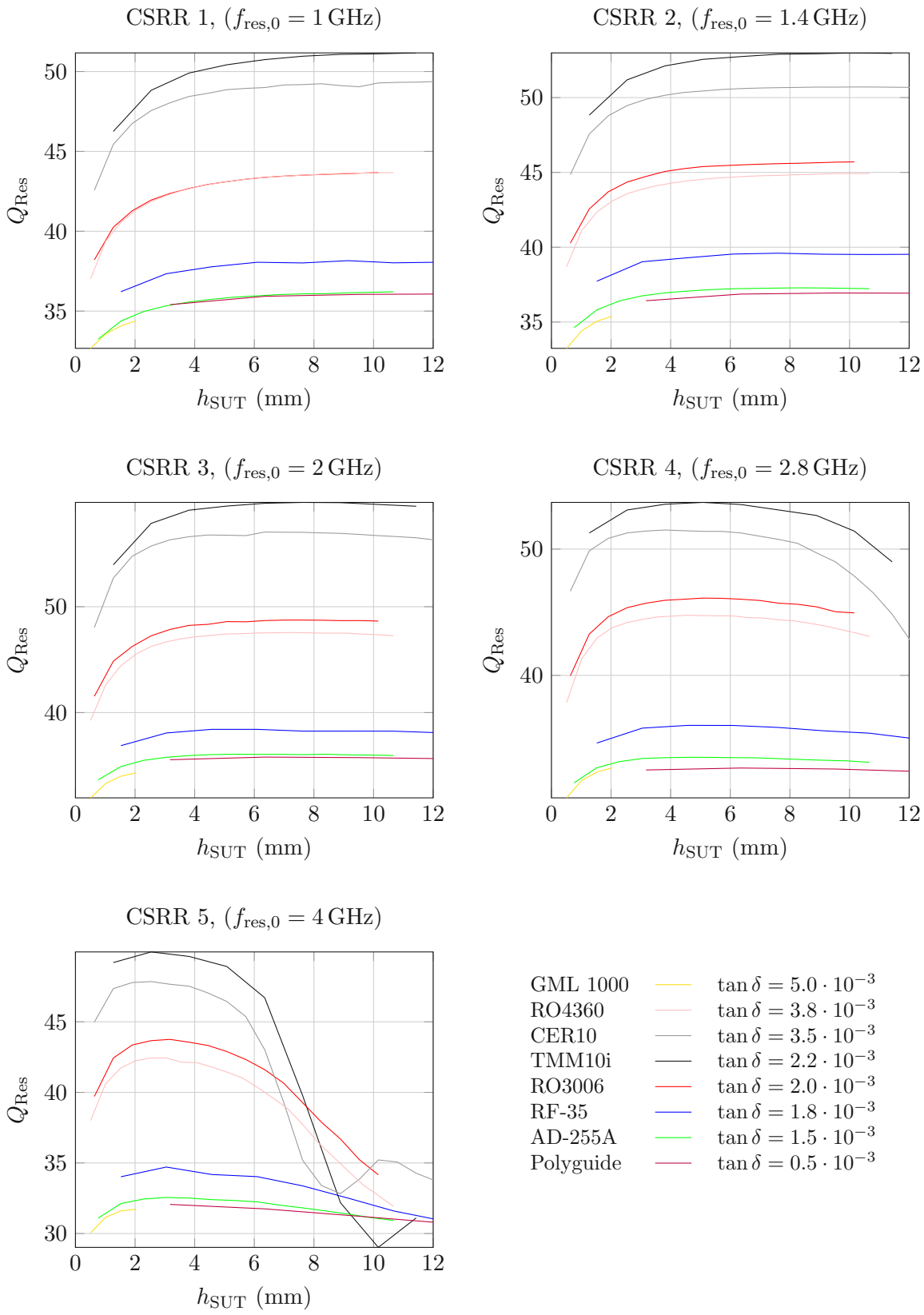

Figure 5.9: Values for Q_{Res} after optimization using measurement data.

5.6 Conclusion

The linear relation

$$\varepsilon_r' = a\,(h_{\mathrm{SUT}}) \cdot S + 1 \tag{5.7}$$

was experimentally verified. The parameter $a\,(h_{\mathrm{SUT}})$ does not significantly increase above a certain threshold sample thickness h_{SUT}. A higher resonant frequency of the CSRR corresponds to a lower threshold for h_{SUT}. As a result, the exact value of h_{SUT} does not need to be known in order to measure an SUT's permittivity, as long as it is above a certain threshold. The parameter $a\,(h_{\mathrm{SUT}})$ is also a function of the CSRR's resonant frequency, which is in turn a function of its side length d according to (4.2). The value for $a\,(h_{\mathrm{SUT}})$ must be obtained by loading the CSRR with a sample whose permittivity is known at the loaded CSRR's resonant frequency. The ratio S/χ_{nom} deviates by up to $\pm 4.5\,\%$ for all five CSRRs.

The linear relation

$$\tan\delta = b\,(h_{\mathrm{SUT}}) \cdot \tilde{Q}^{-1} \tag{5.8}$$

was established based on simulations in Chapter 3. Experimentally verifying (5.8) faced two major challenges. For one, the samples used during the measurements have a significantly lower loss tangent than the FR-4 substrate of the CSRR test fixture. In fact, the samples' loss tangents are on the order of the measurement uncertainty derived in Chapter 3. Additionally, the exact values for the samples' loss tangents are not known at the CSRRs resonant frequencies. In fact, the information about the loss tangents in the data sheets is not provided for the same frequencies. Nevertheless, the measurement results show some consistency with expectations. When comparing materials with a similar ε_r', higher measured values of $\tilde{Q}^{-1}$ correspond to higher values of $\tan\delta$ in the data sheets, with the exception of RF-35, whose loss tangent is provided at a different frequency than for the other materials. Furthermore, the measured values of $\tilde{Q}^{-1}$ are on the same order as the simulated values for SUTs with similar complex permittivities. In order to accurately measure the materials' loss tangents, two aspects are required:

1. The PCB substrate's loss tangent must not be greater than the loss tangent of the SUTs.

2. The parameter $b\,(h_{\mathrm{SUT}})$ must be obtained with a material whose loss tangent is known at the loaded CSRR's resonant frequency, similar to measuring the permittivity.

6 Summary and Outlook

This thesis presents a novel method of characterizing dielectrics using CSRRs. A sample under test's (SUT's) complex permittivity can be measured by pressing it against a CSRR, thereby loading the CSRR. Loading the CSRR with an SUT shifts its resonant frequency and Q-factor. Current methods in the literature relate these changes to the SUT's permittivity and loss tangent. The method presented in this thesis provides more insight into loading CSRRs by studying the CSRR's equivalent circuit and the SUT's effect on the CSRR's equivalent circuit elements. In particular, I identified quantities related to a CSRR's equivalent circuit that follow a linear relation with an SUT's susceptibility and loss tangent.

In Chapter 2, an improved equivalent circuit model for unloaded CSRRs was devised based on simulations in HFSS. In Chapter 3, I study the changes in the equivalent circuit elements when the CSRR is loaded with an SUT. Two linear relations suitable for characterizing dielectrics are formulated. They link values for some of the equivalent circuit elements to the SUT's susceptibility and loss tangent. In order to verify the formulated relations, a test fixture containing multiple CSRRs with different resonant frequencies is designed in Chapter 4. The test fixture was used to demonstrate a new material characterization method in Chapter 5. The CSRRs on the test fixture were loaded with materials with known complex permittivities.

The measurement results demonstrated that a material's permittivity can be obtained from the increase in one capacitance in the equivalent circuit. Furthermore, it was experimentally shown that: (i) The air gap between a CSRR and a sample can be closed by pressing the sample against the CSRR. (ii) The capacitance converges with increasing thickness of the sample loading the CSRR. Thus, it is possible to measure a material's ε_r' without having to know the sample's thickness, as long as it is larger than a certain threshold. (iii) Stacking multiple samples of the same material on top of each other does not limit the ability to measure its permittivity. This is convenient when only thin material samples are available.

The test fixture's FR-4 substrate has a loss tangent that is 4 to 40 times greater than that of the SUTs whose permittivities were measured. The fact that the SUTs' loss tangents are significantly lower than that of the FR-4 substrate could be shown, but their exact values could not be determined. The SUTs' loss tangents are listed in data sheets, but not for the resonant frequencies of the loaded CSRRs. Without knowing the loss tangents beforehand, the proposed method to measure a material's loss tangent cannot be verified.

Exact values for the loss tangents can be provided by a proven test method, like the ones discussed in Section 1.1.

Determining $\tilde{Q}^{-1}$, which is linked to an SUT's loss tangent, revealed an unexpected effect. The CSRR's Q-factor experiences a sudden drop when the height of the stacked samples exceeds a certain threshold. For CSRR 5, that threshold lies at around 4 mm, which is substantially higher than a typical sample thickness, and S almost converges. Hence, the ability to measure a sample's loss tangent is not negated.

The results in this thesis give an outlook to further steps in future work. The material characterization method in this thesis requires one sample whose complex permittivity is known. I suggest taking a sample and measuring its permittivity and loss tangent with a method discussed in Section 1.1. Once its complex permittivity is known, the sample can be carved into smaller samples that are used to determine the parameters a and b.

Another result shows that the test fixture's ability to measure a sample's loss tangent is limited by the loss tangent of the test fixture's substrate. The loss tangent of the test fixture's substrate is proportional to the uncertainty to which a sample's loss tangent can be measured. I suggest using a low-loss RF substrate instead of FR-4 for a test fixture in future experiments.

Another potential improvement lies in the calibration method during measurements. The TRL calibration suffers from the fact that variations in the connectors' S-parameters cannot be differentiated from the S-parameters of the CSRR. I suggest using an auto fixture removal (AFR) calibration instead. The distances between each connector and the CSRRs are long enough to separate connectors from CSRRs in the time domain. Thus, an AFR calibration can remove the connectors' effects on the measured S-parameters, even if they all exhibit vastly different S-parameters.

A Complex Permittivity Measurement Example

The workflow in order to measure a material's complex relative permittivity is given in this chapter. The required components are listed in Section A.1. The instructions to perform a TRL calibration are given in Section A.2. Determining the equivalent circuit parameters of an unloaded CSRR follows the instructions in Section A.3. Section A.4 describes how to obtain the parameters a and b that are required in order to measure a material's permittivity. Section A.5 describes how to determine a material's complex relative permittivity from the measurement results and the parameters a and b.

A.1 Required Components

The required components are:

1. A vector network analyzer.
2. A test fixture that contains CSRRs and the elements for a TRL calibration. An example is given in Chapter 4.
3. Blocks of Rohacell. One piece of Rohacell is required to press the samples against the test fixture during measurement. The test fixture rests on the other block of Rohacell, as the example in Fig. 5.2 shows.
4. *MultilineTRL*, which is available in [49]. Using *MultilineTRL* can be omitted, if the VNA is capable of performing a TRL calibration. The TRL calibration must be performed in the frequency range between f_{min} and f_{max} in steps of f_{step}. The frequency f_{max} must be at least twice the resonant frequency of the CSRR with the greatest resonant frequency on the test fixture. The frequency f_{min} must be no more than 30% of the resonant frequency of the CSRR with the smallest resonant frequency on the test fixture in order to measure sample permittivities up to 10. I recommend a step size f_{step} of 1 MHz.
5. An estimate for the propagation constant γ on the microstrip line. This can be obtained by FWSs in HFSS or using closed-form expressions as in [36].

6. Samples of a material whose relative complex permittivity is known. This material is called the reference material. The thickness of a stack of available samples should be at least the same as the thickness of the material whose permittivity shall be measured. This is the test material.

A.2 TRL Calibration

If the VNA is capable of performing the TRL calibration, proceed as follows:

1. Perform an SOLT calibration in the frequency range between f_{min} and f_{max} in steps of f_{step}.
2. Perform the TRL calibration with the TRL calibration elements on the test fixture.

When using *MultilineTRL*, proceed as follows:

1. Perform an SOLT calibration in the frequency range between f_{min} and f_{max} in steps of f_{step}.
2. Measure the S-parameters of the TRL calibration elements on the test fixture and store the results of the line and thru elements in Touchstone s2p files. Store the measurement results of the open standards in Touchstone s1p files.
3. Create a file called `CalKitConf.txt`. Fig. A.1 contains an example of the contents to write into the file. The first column indicates the calibration standard. Valid entries are either `THRU`, `LINE`, or `REFLECT`. The second column contains the name of the respective Touchstone s2p or s1p file. They must be in the same directory as `CalKitConf.txt`. In the third column, write the port number of the VNA in case of a `REFLECT`, 0 in case of a `THRU`, and the additional line length if the line standard in mm in case of a `LINE` standard.

```
THRU      T.s2p    0
LINE      L1.s2p   9.135
LINE      L2.s2p   30.4
LINE      L3.s2p   36.5014
REFLECT   O1.s1p   1
REFLECT   O2.s1p   2
```

Figure A.1: Example of `CalKitConf.txt`.

4. Create a file called `gammaEstimate.txt`. The file `gammaEstimate.txt` contains the estimated propagation constant γ for each frequency point in the calibration, where

$$\gamma = \alpha + j\beta, \tag{A.1}$$

where α is the attenuation constant and β is the phase constant. An example is shown in Fig. A.2. The first column contains the frequency in Hz. The second

10000000	0.38980253	88.44913683
11000000	0.428467365	88.53343161
12000000	0.467113717	88.60444313
13000000	0.505744375	88.66494434
14000000	0.544361069	88.71695677
15000000	0.582964823	88.76200594
16000000	0.621556206	88.80127435
17000000	0.660135512	88.83569779
18000000	0.698702873	88.86602881
19000000	0.737258338	88.8928803

Figure A.2: Example of the first lines of `gammaEstimate.txt`.

column contains the magnitude of the propagation constant in m^{-1}. The third column contains the phase propagation constant in degrees. An estimate for γ can be obtained by

- Using FWSs, such as in HFSS.
- Using TxLine by Cadence [50]. TxLine allows to calculate α and β. The screenshot in Fig. A.3 shows an example. The phase constant $\beta_{\mathrm{deg/m}}$ is given in degrees per meter. The attenuation constant $\alpha_{\mathrm{dB/m}}$ is given under the name "Loss". The second and third columns in `gammaEstimate.txt` require the

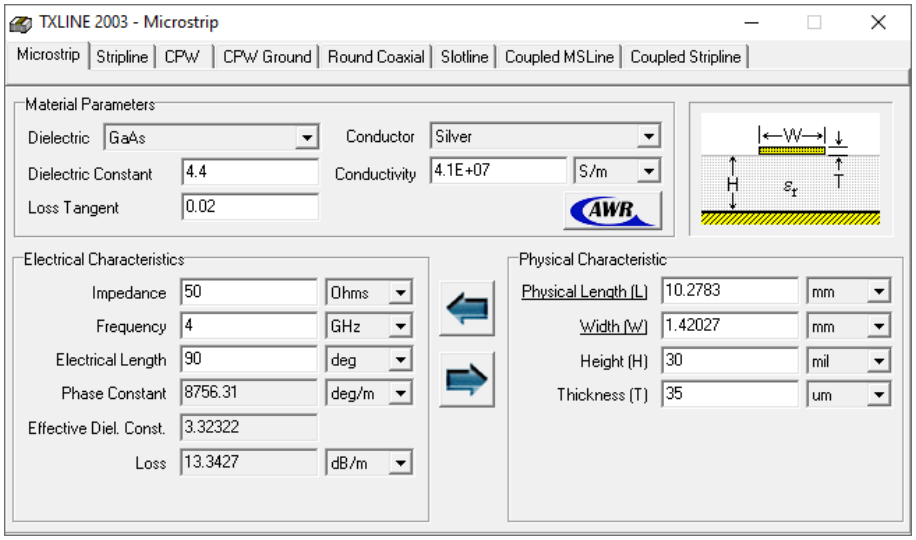

Figure A.3: Screenshot of TxLine [50].

magnitude $|\gamma|$ and phase $\arg\gamma$ of γ. The following equations must be applied

to obtain $|\gamma|$ and $\arg\gamma$ from $\alpha_{\mathrm{dB/m}}$ and $\beta_{\mathrm{deg/m}}$:

$$\alpha_{\mathrm{Np/m}} = \frac{\ln 10}{20} \cdot \alpha_{\mathrm{dB/m}} \approx 0.11512955 \cdot \alpha_{\mathrm{dB/m}}, \tag{A.2}$$

$$\beta_{\mathrm{rad/m}} = \frac{\pi}{180} \cdot \beta_{\mathrm{deg/m}} \approx 0.01745 \cdot \beta_{\mathrm{deg/m}}, \tag{A.3}$$

$$|\gamma| = \sqrt{\alpha_{\mathrm{Np/m}}^2 + \beta_{\mathrm{rad/m}}^2}, \tag{A.4}$$

$$\arg\gamma = \frac{180}{\pi} \cdot \arctan\frac{\beta_{\mathrm{rad/m}}}{\alpha_{\mathrm{Np/m}}}. \tag{A.5}$$

The steps to calibrate individual measurement results are given in Subsection A.2.1.

A.2.1 Calibration Measurements with MultilineTRL

In order to perform a TRL calibration with `MultilineTRL`, proceed as follows:

1. Store the measurement results in a Touchstone s2p file.
2. Call the file `main.m` in MATLAB.
3. Press `Read CalKit` in the GUI. A pop-up window opens. Select the file `CalKitConf.txt` and press `Open`. Another pop-up window opens. Select the file `gammaEstimate.txt` and press `Open`.
4. Use the radio buttons below `REFLECT Type` in the GUI to specify if the reflect standards are of type open or short.
5. Press `Start Cal.`
6. Press `Ref. Plane Shift`. A pop-up window opens. Select the s2p files of the measurements you want to calibrate. You can select multiple files. Press `Open`. `MultilineTRL` creates a new directory that contains the calibrated measurement results.

A.3 Unloaded Resonator Equivalent Circuit

1. Measure the S-parameters of the CSRRs when they are unloaded, as shown in Fig. 5.2.
2. Store the measured S-parameters in Touchstone s2p files.
3. Use the results in the s2p file in order to proceed with the optimization in case the TRL calibration was performed by the VNA. When using *MultilineTRL*, perform the calibration according to Subecction A.2.1.
4. Apply the optimization procedure in Chapter 2 using the circuit in Fig. 2.6. The solutions in Figs. 2.8 and 2.9 provide good starting values.
5. Store the values for the equivalent circuit parameters in a file.

A.4 Determining the CSRR's Parameters A and B

Measuring the complex permittivity of the sample material requires a calibration with a sample of the reference material. Suitable reference material for measuring the real permittivity is Polyguide, whose real permittivity changes slowly over frequency due to its low loss tangent.

There are two possible approaches with regard to the thickness of the material samples when they load the CSRRs.

1. The thicknesses of both material samples h_{sample} are equal. Generally h_{sample} does not have to be the thickness of one sample. Instead, multiple samples may be stacked on top of each other such that the stack reaches a thickness of h_{sample}.
2. The thickness of both material samples (or stacks of samples) h_{sample} is above a certain threshold, such that a further increase in h_{sample} does not change the measurement results. Fig. 5.6 shows how the curves containing the measured values for S flatten. The flattening indicates threshold values for h_{sample}, above which S does not increase.

In order to measure the real permittivity and loss tangent of a sample of the test material whose thickness is h_{sample}, two parameters a (sample) and b (sample) must be determined for h_{sample}. In general, h_{sample} does not have to be the thickness of one sample, it can also be the thickness of a stack of multiple samples of the MUT.

1. Stack enough samples of the reference material on top of each other so that its height is h_{sample}.
2. Place the stack on a CSRR, like in Fig. 5.4.
3. Measure the S-parameters of the CSRR. Press the stack against the test fixture as in Fig. 5.5.
4. When using `MultilineTRL`, calibrate the results according to the procedure in Subsection A.2.1.
5. Apply the optimization procedure in Chapter 3 when using Variation 4 from Tab. 3.5.
6. Store the results for C_{Res} and G_{Res} in a file.
7. Calculate the values S_{RM} and $\tilde{Q}_{\text{RM}}^{-1}$ as

$$S_{\text{RM}} = \frac{C_{\text{Res,RM}} - C_{\text{Res,0}}}{C_{\text{Res,RM}}}, \tag{A.6}$$

$$\tilde{Q}_{\text{RM}}^{-1} = \sqrt{\frac{L_{\text{res}}}{C_{\text{res,RM}} - C_{\text{res,0}}}} \cdot (G_{\text{res,RM}} - G_{\text{res,0}}), \tag{A.7}$$

where $C_{\text{Res,RM}}$ and $G_{\text{Res,RM}}$ are C_{Res} and G_{Res} for the CSRR loaded with the reference material. The parameters $C_{\text{Res,0}}$ and $G_{\text{Res,0}}$ are C_{Res} and G_{Res} for the unloaded CSRR.

8. Knowing the reference materials permittivity and loss tangent, calculate the parameters $a\left(h_{\text{sample}}\right)$ and $b\left(h_{\text{sample}}\right)$, proceed as follows:

$$a\left(h_{\text{sample}}\right) = \left(\varepsilon'_{r,\text{RM}} - 1\right) / S_{\text{RM}}, \tag{A.8}$$

$$b\left(h_{\text{sample}}\right) = \tan\delta_{\text{RM}} / \tilde{Q}^{-1}_{\text{RM}}, \tag{A.9}$$

where $\varepsilon'_{r,\text{RM}}$ and $\tan\delta_{\text{RM}}$ are the permittivity and loss tangent of the reference material, respectively.

A.5 Measuring a Samples Permittivity

1. Repeat steps 1–6 from Section A.4 but with the test material instead of the reference material.

2. Calculate the values S_{TM} and $\tilde{Q}^{-1}_{\text{TM}}$ as

$$S_{\text{TM}} = \frac{C_{\text{Res,TM}} - C_{\text{Res},0}}{C_{\text{Res,TM}}}, \tag{A.10}$$

$$\tilde{Q}^{-1}_{\text{TM}} = \sqrt{\frac{L_{\text{res}}}{C_{\text{res,TM}} - C_{\text{res},0}}} \cdot \left(G_{\text{res,TM}} - G_{\text{res},0}\right), \tag{A.11}$$

where $C_{\text{Res,TM}}$ and $G_{\text{Res,TM}}$ are C_{Res} and G_{Res} for the CSRR loaded with the test material. The parameters $C_{\text{Res},0}$ and $G_{\text{Res},0}$ are C_{Res} and G_{Res} for the unloaded CSRR. Calculate the test material's permittivity $\varepsilon'_{r,\text{TM}}$ and loss tangent $\tan\delta_{\text{TM}}$ as

$$\varepsilon'_{r,\text{TM}} = a\left(h_{\text{sample}}\right) \cdot S_{\text{TM}} + 1, \tag{A.12}$$

$$\tan\delta_{\text{TM}} = b\left(h_{\text{sample}}\right) \cdot \tilde{Q}^{-1}_{\text{TM}}. \tag{A.13}$$

References

[1] Lin-Feng Chen, Chong Kim Ong, C.P. Neo, Vasundara V. Varadan, and Vijay K. Varadan. *Microwave Electronics: Measurement and Materials Characterization*. John Wiley & Sons, 2004. 1, 2, 6, 7, 8

[2] Keysight Technologies. Basics of Measuring the Dielectric Properties of Materials. `http://www.keysight.com/us/en/assets/7018-01284/application-notes/5989-2589.pdf`, last accessed: 25th of May, 2022. 1, 7

[3] QWED Company. Test Fixtures and Setups. `http://www.qwed.eu/test_fixtures_brochure.pdf`, last accessed: 5th of July, 2022. 1, 5

[4] IPC. IPC-TM-650 Relative Permittivity and Loss Tangent Using a Split-Cylinder Resonator. `www.ipc.org/sites/default/files/test_methods_docs/2-5-5-13.pdf`, last accessed: 8th of June, 2022. 1, 4, 5

[5] IPC. Stripline Test for Permittivity and Loss Tangent (Dielectric Constant and Dissipation Factor) at X-Band. `https://www.ipc.org/sites/default/files/test_methods_docs/2-5_2-5-5-5.pdf`, last accessed: 5th of July, 2022. 1

[6] IEC. IEC 61189-2-721:2015. `https://webstore.iec.ch/publication/22343`, last accessed: 5th of July, 2022. 1

[7] Kenny Liao and Keysight Technologies. mmWave Material Measurements for 5G and Radar. `https://www.keysightevent.com/kw2020/handout/d3`, last accessed: 15th of July, 2022. 3

[8] Keysight Technologies. 85072A 10-GHz Split Cylinder Resonator. `https://www.keysight.com.cn/cn/zh/assets/7018-01496/technical-overviews/5989-6182.pdf`, last accessed: 8th of June, 2022. 3, 5

[9] Keysight Technologies. Split Post Dielectric Resonators for Dielectric Measurements of Substrates. `https://www.keysight.com/at/de/assets/7018-01416/application-notes/5989-5384.pdf`, last accessed: 9th of June, 2022. 3, 5, 6

[10] Keysight Technologies. Solutions for Measuring Permittivity and Permeability with LCR Meters and Impedance Analyzers. `https://www.keysight.com/at/de/assets/7018-06683/application-notes/5980-2862.pdf`, last accessed: 5th of July, 2022. 3, 7

[11] James Baker-Jarvis, Michael D. Janezic, P.D. Domich, and Richard G. Geyer. Analysis of an open-ended coaxial probe with lift-off for nondestructive testing. *IEEE Transactions on Instrumentation and Measurement*, 43(5):711–718, 1994. 3, 7

[12] James Baker-Jarvis, E. J. Vanzura, and W. A. Kissick. Improved technique for determining complex permittivity with the transmission/reflection method. *IEEE Transactions on Microwave Theory and Techniques*, 38(8):1096–1103, 1990. 3, 8

[13] Keysight Technologies. Long-awaited mmWave Low-loss Dielectric Material Test Solution. `https://www.keysight.com/at/de/assets/7018-06384/brochures/5992-3438.pdf`, last accessed: 5th of July, 2022. 4

[14] Max Gattringer. An Improved Model for Complex Permittivity Measurements with a Split-Cylinder Resonator. Master's thesis, TU Wien, Gusshausstrasse 25, 1040 Vienna, Austria, april 2017. 4

[15] QWED Company. Split Post Dielectric Resonators (SPDR). `https://www.qwed.eu/resonators_spdr.html`, last accessed: 5th of July, 2022. 5

[16] Asja Veber, Špela Kunej, and Danilo Suvorov. Dielectric Properties of Sol–Gel-Derived Bi12SiO20 Thin Films. *Journal of the American Ceramic Society*, 96(1):157–160, 2013. 6

[17] Keysight Technologies. Materials Measurement: Dielectric Materials Application Brief. `https://www.keysight.com/at/de/assets/7018-08589/brochures/5989-4713.pdf`, last accessed: 6th of June, 2022. 6, 7

[18] Michael C. Hegg and Alexander V. Mamishev. Influence of Variable Plate Separation on Fringing Electric Fields in Parallel-Plate capacitors. In *Conference Record of the 2004 IEEE International Symposium on Electrical Insulation*, pages 384–387, 2004. 7

[19] Richard Wilson and Giovanni D'Amore. Measuring Critical Material Properties of Capacitors and Inductors. `https://www.electronicsweekly.com/news/measuring-critical-material-properties-capacitors-inductors-2017-03/`, last accessed: 5th of July, 2022. 7

[20] Physics Curriculum & Instruction. Electrostatics 3D Electric Field & Potential Simulator. `https://www.physicscurriculum.com/electrostatics3d`, last accessed: 18th of August, 2022. 7

[21] Schmid & Partner Engineering AG. DAK. `https://speag.swiss/products/dak/dak-probes/`, last accessed: 18th of July, 2022. 7

[22] A. M. Nicolson and Gerald F. Ross. Measurement of the Intrinsic Properties of Materials by Time-Domain Techniques. *IEEE Transactions on Instrumentation and Measurement*, 19(4):377–382, 1970. 8

[23] William B. Weir. Automatic measurement of complex dielectric constant and permeability at microwave frequencies. *Proceedings of the IEEE*, 62(1):33–36, 1974. 8

[24] James Baker-Jarvis, Richard G. Geyer, and P. D. Domich. A nonlinear least-squares solution with causality constraints applied to transmission line permittivity and permeability determination. *IEEE Transactions on Instrumentation and Measurement*, 41(5):646–652, 1992. 8

[25] Filippo Costa, Michele Borgese, Marco Degiorgi, and Agostino Monorchio. Electromagnetic Characterisation of Materials by Using Transmission/Reflection (T/R) Devices. *Electronics*, 6(4), 2017. 9

[26] Ala Eldin Omer, George Shaker, Safieddin Safavi-Naeini, Hamid Kokabi, Georges Alquié, Frédérique Deshours, and Raed M. Shubair. Low-Cost Portable Microwave Sensor for Non-Invasive Monitoring of Blood Glucose Level: Novel Design Utilizing a Four-Cell CSRR Hexagonal Configuration. *Nature Scientific Reports*, 10(15200), 2020. 9, 11, 13, 34

[27] Francisco Falcone, Txema Lopetegi, Juan Domingo Baena, Ricardo Marqués, Ferran Martín, and Mario Sorolla. Effective Negative-/spl epsiv/ Stopband Microstrip Lines based on Complementary Split Ring Resonators. *IEEE Microwave and Wireless Components Letters*, 14(6):280–282, 2004. 11

[28] Muhammed Said Boybay and Omar M. Ramahi. Material Characterization Using Complementary Split-Ring Resonators. *IEEE Transactions on Instrumentation and Measurement*, 61(11):3039–3046, 2012. 11, 24

[29] Chieh-Sen Lee and Chin-Lung Yang. Thickness and Permittivity Measurement in Multi-Layered Dielectric Structures Using Complementary Split-Ring Resonators. *IEEE Sensors Journal*, 14(3):695–700, 2014. 11

[30] Nilesh Kumar Tiwari, Prashant Kumar Varshney, Surya Prakash Singh, and M. Jaleel Akhtar. Shape Perturbed Tunable Planar RF Resonator for the Dielectric Measurement in wide frequency range. In *2019 8th Asia-Pacific Conference on Antennas and Propagation (APCAP)*, pages 666–667, 2019. 11

[31] Mohammad Arif Hussain Ansari, Abhishek Kumar Jha, Zubair Akhter, and Mohammad Jaleel Akhtar. Multi-Band RF Planar Sensor Using Complementary Split Ring Resonator for Testing of Dielectric Materials. *IEEE Sensors Journal*, 18(16):6596–6606, 2018. 11

[32] Roghieh Karimzadeh Baee, Gholamreza Dadashzadeh, and F. Geran Kharakhili. Using of CSRR and its Equivalent Circuit Model in Size Reduction of Microstrip Antenna. In *2007 Asia-Pacific Microwave Conference*, pages 1–4, 2007. 11

[33] Juan Domingo Baena, Jordi Bonache, Ferran Martín, Ricardo Marqués Sillero, Francisco Falcone, Txema Lopetegi, Miguel A. G. Laso, Joan García–García, Ignacio Gil, Maria Flores Portillo, and Mario Sorolla. Equivalent-Circuit Models for Split-Ring Resonators and Complementary Split-ring Resonators Coupled to Planar Transmission Lines. *IEEE Transactions on Microwave Theory and Techniques*, 53(4):1451–1461, 2005. 11, 13, 36

[34] Jordi Bonache, Marta Gil, Ignacio Gil, Joan Garcia-Garcia, and Ferran Martín. On the Electrical Characteristics of Complementary Metamaterial Resonators. *IEEE Microwave and Wireless Components Letters*, 16(10):543–545, 2006. 11

[35] Chao Li, Kaiyu Liu, and Fang Li. An Equivalent Circuit for the Complementary Split Ring Resonators (CSRRs) With Application to Highpass Filters. In *2006 International Symposium on Biophotonics, Nanophotonics and Metamaterials*, pages 478–479, 2006. 11, 13

[36] Erik O. Hammerstad and Ø. Jensen. Accurate Models for Microstrip Computer-Aided Design. In *1980 IEEE MTT-S International Microwave symposium Digest*, pages 407–409, 1980. 13, 63

[37] Mohammad Arif Hussain Ansari, Abhishek Kumar Jha, and Mohammad Jaleel Akhtar. Design and Application of the CSRR-Based Planar Sensor for Noninvasive Measurement of Complex Permittivity. *IEEE Sensors Journal*, 15(12):7181–7189, 2015. 34

[38] Pasternack Enterprises, Inc. SMA Female Connector Solder Attachment .031 inch End Launch PCB. `https://www.pasternack.com/images/ProductPDF/PE44206.pdf`, last accessed: 8th of July, 2022. 37

[39] Roger B. Marks. A multiline method of network analyzer calibration. *IEEE Transactions on Microwave Theory and Techniques*, 39(7):1205–1215, 1991. 41, 49

[40] Crane Company. Polyguide™ Microwave Laminates Data Sheet. `https://www.craneae.com/sites/default/files/documents/Polyguide-Data-Sheet-Rev-Feb-2016_0.pdf`, last accessed: 20th of May, 2022. 47

[41] GIL. GML 1000 High Frequency Laminate Data Sheet. `http://www.shfmicro.com/gil20.pdf`, last accessed: 20th of May, 2022. 47

[42] Arlon. AD255A Laminate Data Sheet. `http://www.agssales.com/ad255a.pdf`, last accessed: 20th of May, 2022. 47

[43] Taconic. RF-35 Data Sheet. `http://www.taconic.co.kr/download/RF-35.pdf`, last accessed: 20th of May, 2022. 47

[44] Taconic. CER-10 Data Sheet. `https://www.elcopcb.com/material-docs/taconic/CER-10.pdf`, last accessed: 20th of May, 2022. 47

[45] Rogers Corporation. TMM Data Sheet. `https://rogerscorp.com/-/media/project/rogerscorp/documents/advanced%2Delectronics%2Dsolutions/english/data%2Dsheets/tmm%2Dthermoset%2Dlaminate%2Ddata%2Dsheet%2Dtmm3%2D%2D%2D%2Dtmm4%2D%2D%2D%2Dtmm6%2D%2D%2D%2Dtmm10%2D%2D%2D%2Dtmm10i%2D%2D%2D%2Dtmm13i.pdf`, last accessed: 20th of May, 2022. 47

[46] Rogers Corporation. RO3000 Series Circuit Materials Data Sheet. `https://rogerscorp.com/-/media/project/rogerscorp/documents/advanced-electronics-solutions/english/data-sheets/ro3000-laminate-data-sheet-ro3003----ro3006----ro3010----ro3035.pdf`, last accessed: 20th of May, 2022. 47

[47] Rogers Corporation. RO4360G2 Data Sheet. `https://rogerscorp.com/-/media/project/rogerscorp/documents/advanced-electronics-solutions/`

english/data-sheets/ro4360g2-high-frequency-laminates-data-sheet.pdf, last accessed: 20th of May, 2022. 47

[48] Evonik Industries AG. Choose the ROHACELL® PMI foam for your application and process - Evonik Industries. https://performance-foams.evonik.com/en/products-and-solutions/rohacell, last accessed: 26th of July, 2022. 48

[49] Wenzhi Wang (simonary) and npanti. MultilineTRL. https://github.com/simonary/MultilineTRL, last accessed: 22nd of July, 2022. 49, 63

[50] Cadence Design Systems, Inc. AWR TX-LINE. https://www.cadence.com/ko_KR/home/tools/system-analysis/rf-microwave-design/awr-tx-line.html, last accessed: 19th of August, 2022. 65

Hiermit erkläre ich, dass ich die vorliegende Arbeit gemäß dem Code of Conduct – Regeln zur Sicherung guter wissenschaftlicher Praxis, insbesondere ohne unzulässige Hilfe Dritter und ohne Benutzung anderer als der angegebenen Hilfsmittel, angefertigt wurde. Die aus anderen Quellen direkt oder indirekt übernommenen Daten und Konzepte sind unter Angabe der Quelle gekennzeichnet. Die Arbeit wurde bisher weder im In- noch im Ausland in gleicher oder in ähnlicher Form in anderen Prüfungsverfahren vorgelegt.

Wien, 24. August 2022 *Edgar Philip Jirousek*